Richard Berger, BSc

Nano-Porous Zinc Oxide
via
Molecular Layer Deposition

Master's Thesis

to achieve the university degree of

Diplom-Ingenieur

Master's degree programme: Technical Physics

submitted to

Graz University of Technology

Supervisor

Assoc. Prof. Dr. Anna Maria Coclite

Co-Supervisor

Dott. Mag. Dr Alberto Perrotta

Institute for Solid State Physics

Graz, March 2019

AFFIDAVIT

I declare that I have authored this thesis independently, that I have not used other than the declared sources/resources, and that I have explicitly indicated all material which has been quoted either literally or by content from the sources used. The text document uploaded to TUGRAZonline is identical to the present master's thesis.

_____
Date

_____
Signature

Acknowledgments

First of all, I want to thank my co-supervisor Alberto Perrotta for supporting, teaching and motivating me throughout this whole thesis. He gave me any possible freedom within this work and was always there when I needed his advice.

Second, I am thankful for all the friends I found amongst the research group of my supervisor Anna Coclite. Sharing the office with Fabian Muralter, Marianne Kräuter, Julian Pilz, and Taher Abu Ali made every single working day joyful. It is thanks to the leadership style of Anna Coclite that there is a very friendly and familiar atmosphere in this whole group.

Furthermore, I would also like to thank Harald Kerschbaumer for all the technical support during the construction of the experimental setup.

Most of all I want to thank my family, especially my mother Marion Berger, for the love and encouragement they gave me throughout my whole life.

1   INTRODUCTION

Densely packed zinc oxide (ZnO) in thin film form is used in a widespread field of applications due to its multifunctional physical and chemical properties. Especially in case of bio- and UV-sensors, photoanodes for dye-sensitized solar cells and photocatalytic applications, ZnO thin films are often employed as a sensing material or as a catalyst. However, the performance of these thin films is mainly limited by a lack of surface area and cavernous structure. Especially for the above-mentioned applications, recent studies show that a porous framework within the ZnO thin films drastically increases the performance [1]. To be precise, one has to differentiate between micro-, meso- and macroporosity. Depending on the application, the dimension of the pores is crucial for the effectiveness of the employed ZnO film. For instance, cholesterol detection threw ZnO thin films is made possible by nanopores [2]. The photoresponse on ZnO based UV-photodetectors is enabled by oxygen trapped inside micropores [3]. And dye-sensitized solar cell anodes exploit porous ZnO films with pores around 50 nm in diameter [4]. Furthermore, it is reported that nano-branched structures, including coral shaped polycrystalline ZnO frameworks in the lower macroporous regime, provide a great piezoelectric response [5], [6].

However, what most synthesizing methods for porous ZnO have in common is a lack of film conformity on textured substrates, which limits its use to planar structure. Furthermore, many of them show deficiencies in cost efficiency, large scale processability, and tunable porosity.

Therefore, it is evident to search for new synthesis methods in order to conformally deposit porous ZnO thin films on textured substrates while simultaneously enabling the tunability of characteristic film properties such as pore size and crystallinity.

A completely new and promising approach to produce conformal porous crystalline zinc oxide films, avoiding the above-mentioned problems, lies in molecular layer deposition (MLD).

The biggest effort of this technique is its capability to create conformal films on uneven surfaces. This, amongst others, allows a radical improvement in the response of biosensors. Via MLD countless biosensors exploiting densely packed zinc oxide micro- / nano-structures could be coated with thin films of micro-/mesoporous ZnO, thus multiplying the gas sensitive surface and leading to a responsivity of these sensors, never seen before. MLD as the film forming technique also offers the possibility to precisely vary the film thickness from a few to hundreds of nanometers. This makes

it possible to tailor the ZnO layers specifically to the needs of each sensor, resulting in a vastly enhanced performance.

Put simply, the concept of creating micro-/mesoporous zinc oxide films via MLD is to produce alternating layers of both zinc-oxygen compounds and organic structures, a so-called metal-organic hybrid film. After growing the film, the organic content is removed by oxidation triggered by heating, leaving behind vacancies within the zinc-oxygen compound that will then crystallize to a porous structure.

With the choice of the heating parameters alone, the properties of the film can be influenced.

By varying the maximum heating temperature, for instance, the crystallite grain size and porosity can be influenced allowing to tune the sensing properties of the film.

Within this master thesis, the first MLD system at the TU Graz was established and an optimized deposition recipe for this setup was found in order to create the desired metal-organic hybrid films, using diethylzinc (DEZ) and ethylene glycol (EG) as the deposition precursors.

The substrate is alternatingly exposed to each of the precursor providing the desired layer-by-layer growth of the film that ensures precise control of the film thickness.

Since this is a completely new approach to synthesize nanoporous ZnO, the potential limits of this method are not determined yet. It is likely that the nanoporous structure decreases the film conductivity compared to densely structured zinc oxide. If this was the case one could obtain a piezoelectric response in incredible thin films opening a whole new field of sensing techniques, foremost for pressure and humidity sensing applications used in recently arising artificial skin concepts.

Motivation
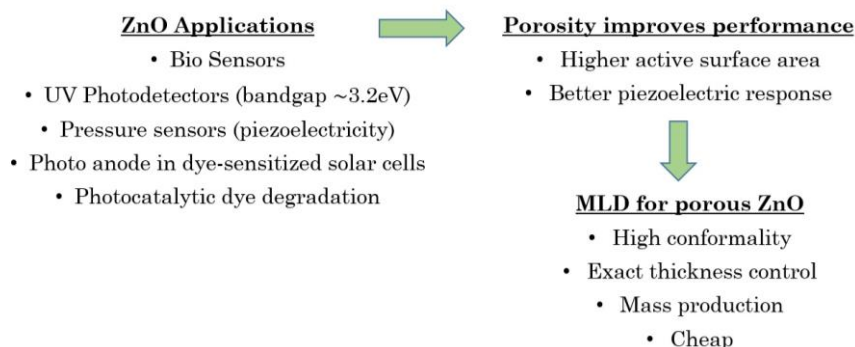
Figure 1: Motivation for porous ZnO via MLD

2 FUNDAMENTALS

2.1 POROUS ZINC OXIDE VIA MOLECULAR LAYER DEPOSITION

2.1.1 MLD for Metal-Organic Hybrid Thin Films

The general idea of MLD is to place a substrate into a vacuum chamber and alternatingly expose it to different reactive gases (precursor gases). Reactions between the precursors take place at the sample surface building up layers of the precursor molecules on top of the substrate. With this, it is possible to create films of alternating metallic and organic monolayers. As a self-limiting process, MLD provides the possibility to precisely vary the film thickness by controlling the number of monolayers that are deposited onto the substrate. Furthermore, one of the strongest feature of MLD is the possibility to conformally coat textured surfaces (this, for example, allows the coverage of nanostructured zinc oxide bio-sensors with a thin layer of nanoporous ZnO in order to increase their performance).

The film growth is based on multiple step reactions in which the different precursor molecules react with each other via their functional groups at the substrate surface. The self-limiting character of this method results from the fact that the precursor molecules are equipped with reactive functional groups which are chosen in a way that reactions can only take place between molecules from different precursor species. Therefore, a reaction between molecules from the same precursor species is not possible, or at least much less likely than a reaction between molecules of a different type. Under proper deposition conditions, this allows the formation of alternating single layers of the according precursor molecules. Choosing one precursor with a metallic content and one with an organic composition, a hybrid film of alternating organic and metallic single layers can be formed. Further details on the fabrication of generic hybrid organic-inorganic films by MLD can be found in [7].

Parent substance for the porous ZnO is a hybrid film of zinc oxide-organic polymers, a so-called Zincone film. In principle Zincone can be formed with a big variety of organic precursors, allowing the modification of the organic part inside the film. Within this thesis ethylene glycol (EG) was used as the organic precursor and diethyl zinc (DEZ) as the precursor providing the desired zinc content. Zincone formation using these precursors is well known and has been studied by many groups such as [8], [9], [10]. Both precursors are equipped with homo-bifunctional groups namely two ethyl groups in case of DEZ and two hydroxyl groups in case of EG. The reactions between the two precursors and the sample surface follow:

DEZ-surface reaction

$$R - OH + (C_2H_5)Zn(C_2H_5) \rightarrow R - OZn(C_2H_5) + C_2H_6 \qquad Rct\ 1$$

EG-surface reaction

$$R - OZn(C_2H_5) + HO(CH_2)_2OH \rightarrow R - OZnO(CH_2)_2OH + C_2H_6 \qquad Rct\ 2$$
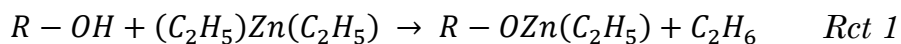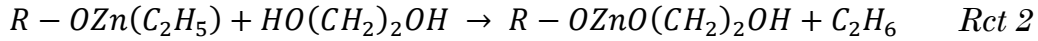
The two reaction schemes are illustrated below:
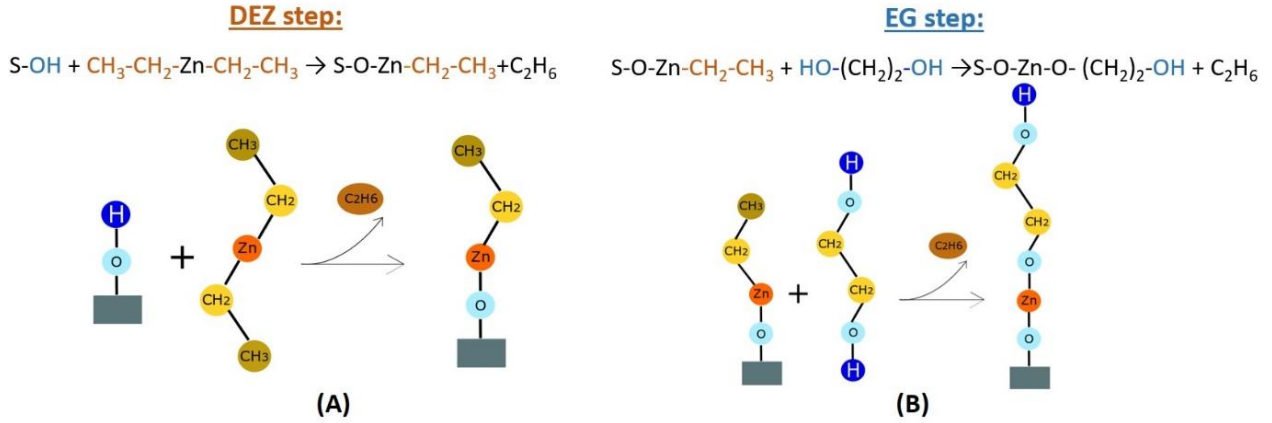
Figure 2: (A) DEZ molecule reacting with a hydroxyl surface functional group (B) EG molecule reacting with an ethyl surface functional group; S denotes the substrate

Figure 2 (A) shows the reaction between a DEZ molecule in the gas phase and a hydroxyl group standing out on top of the sample surface. One of the two ethyl groups of DEZ reacts with a surface hydroxyl group binding the DEZ molecule to the surface and emitting ethane as a by-product. In order to ensure a pristine DEZ atmosphere, the sample inside the vacuum chamber is exposed to short pulses of DEZ gas shot into the chamber. The DEZ molecules can bind to the sample as long as there are hydroxyl functional groups standing out on top of the sample surface.

When all the surface hydroxyl groups have reacted with DEZ the surface is covered with the second ethyl group of DEZ (the one that has not reacted with a surface functional hydroxyl group from the previous step). This, in turn, terminates the reaction between further DEZ molecules in the gas phase and the sample surface since the remaining DEZ molecules from the gas phase cannot react with their own functional groups on top of the surface. This defines the self-limiting character of MLD that ensures the formation of exactly one monolayer of the according precursor molecule at the time.

In the second precursor exposure step, shown in Figure 2 (B), the sample is exposed to vapors of EG molecules. The EG molecules from the gas phase react with the surface ethyl groups provided by the last DEZ step. Again, ethane is a by-product of this reaction. Analog to the DEZ exposure step, the EG can only bind to the surface as long as there are ethyl groups left standing out on top of the surface. After all the ethyl surface groups have reacted to EG the surface is covered with a monolayer of EG with the according hydroxyl groups standing out on top of the surface. Therefore, one finds

the initial condition of the DEZ exposure step (A) and a film of alternating monolayers can be grown by repeating the two exposure steps.

Between precursor exposure steps the atmosphere around the sample has to be evacuated completely from the precursor gas inside the vacuum chamber. The reason for this is to prevent reactions between different precursor species in the gas phase. Such reactions in the gas phase would cause CVD like film growth since one could not control the number of precursor molecules that would react in the gas phase and then deposit on the sample surface. A self-limiting growth can therefore only be ensured in case that reactions between the precursors exclusively take place at the sample surface because there the number of reactive functional groups is limited. Typically, during a purging step, an inert gas is used to carry remaining precursor molecules out of the chamber. For this purpose, the vacuum chamber is evacuated while simultaneously flowing the inert gas inside the chamber. This allows the removal of precursor molecules from the chamber within much shorter purging steps than without the use of a purging gas. A typical purging gas is argon (Ar), which as an inert gas does not cause any reactions inside the chamber but simply transfers momentum to the precursor gas, aiding the removal of the precursor.

A complete MLD cycle (Figure 3) therefore consists of 4 steps: 2 exposure steps in which the particular precursor molecules react and form a monolayer on top of the sample surface and 2 purging steps in which the unreacted precursors and by-products are removed from the vacuum chamber.
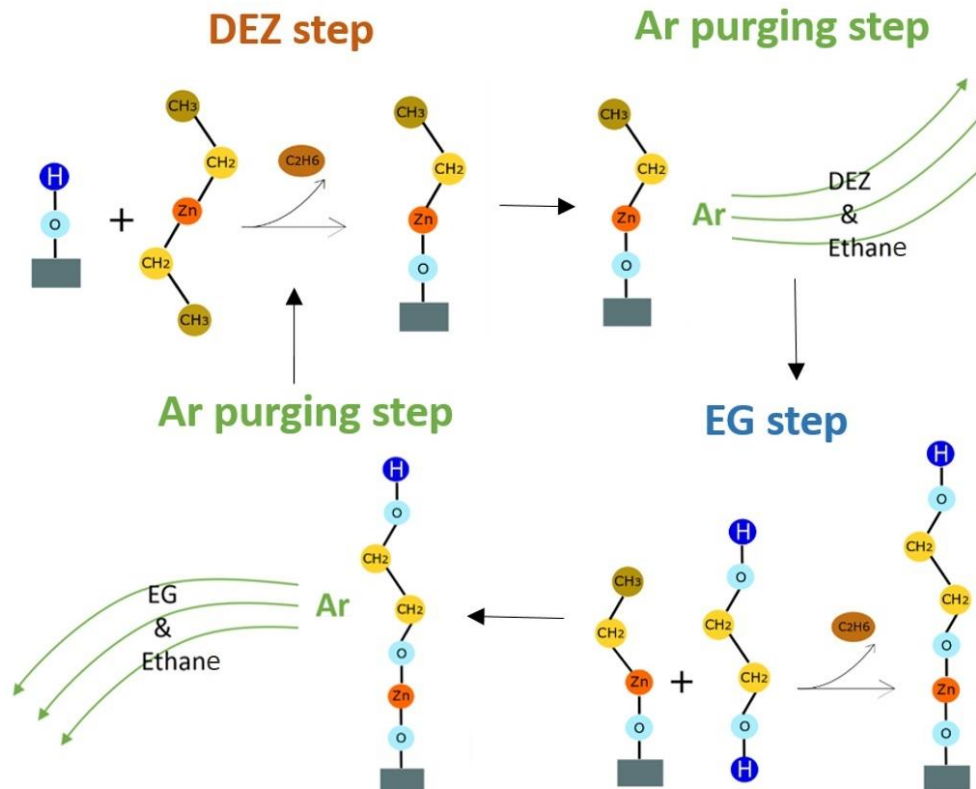
Figure 3: Complete MLD cycle consisting of 2 precursor exposure and 2 purging step

Each step of the complete MLD cycle can be characterised by a so-called saturation curve (Figure 4) in which the film growth per MLD cycle (growth per cycle, GPC) is illustrated as a function of either the purging time in case of a purging step or as a function of the pulsing time in case of an exposure step.
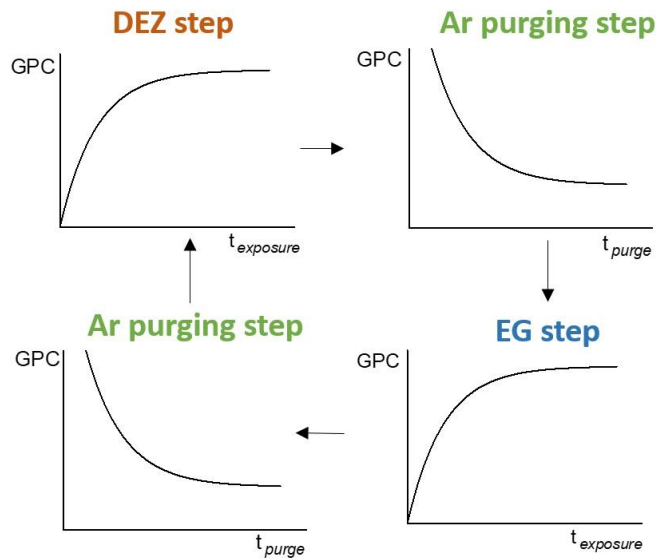
Figure 4: Saturation curves

With the help of the saturation curves (Figure 4), one can find proper purging and precursor exposure times in order to ensure a self-limiting MLD-like growth with a maximum thickness increase per cycle.

The saturation curves owe their name to the fact that for long purging and exposure times the GPC converges to a constant value. One can, therefore, define a saturation regime for each curve in which the GPC barely changes with further increasing exposure/purging times.

According to whether the GPC is measured as a function of the exposure or the purging time different mechanism are responsible for the saturation curve's shape. In any case, a simple model can be applied to obtain physically reasonable fitting functions:

In case the GPC is measured as a function of the precursor exposure time one can explain the saturation curve as follows.

During the exposure step, a connection between the vacuum chamber and the precursor gas vessel is opened and the precursor gas surrounds the sample for the exposure time $t_{exposure}$. During the exposure time, the precursor molecules can react with the surface functional groups and attach to the sample surface.

To form a complete monolayer of the according precursor, every free surface functional group must react with a precursor molecule from the gas phase. However, for shorter exposure times less surface functional groups can react with the precursor molecules. In this case, it takes more than one single deposition step to form a complete monolayer and the film growth per MLD cycle (GPC) decreases.

Therefore, the longer the precursor exposure time, the more surface functional groups get occupied by precursor molecules from the gas phase, increasing the GPC as a function of the exposure time. For exposure times that are long enough almost every available surface functional group reacts with a precursor molecule and a complete monolayer can be formed. Even longer exposure times cause no more precursor deposition since there are no more functional groups left at the surface and one has reached the saturation regime.

Under the following assumptions one can derive a proper fitting function for the exposure saturation curves:

1. The rate at which free surface functional groups get occupied is constant:

$$\frac{dn}{dt} = p_0 \qquad Eq\ 1$$

$dn \dots number\ of\ reactions\ with\ one\ free\ surface\ functional\ group\ in\ dt$

$p_0 \dots occupation\ rate$

$t \dots precursor\ exposure\ time$

In Eq 1 the surface functional group is considered to always be unoccupied, even after a reaction with a precursor molecule. Therefore n can become bigger than 1.

2. The number of free surface functional groups being occupied in a time increment is proportional to the number of free sites at that time and the occupation rate:

$$dN_{ocp(t)} = N_{f(t)} * dn = N_{f(t)} * p_0 * dt \qquad Eq\ 2$$

3. According to the model explained above the boundary conditions are:

$$N_{ocp(t)} = N_{tot} - N_{f(t)} \quad Eq\ 3$$

$$N_{ocp(t=0)} = 0;\ N_{ocp(t\to\infty)} \to N_{tot} \quad Eq\ 4$$

$N_{ocp(t)} \dots number\ of\ surface\ functional\ groups\ that\ reacted\ with\ a\ precursor$

$N_{f(t)} \dots number\ of\ surface\ functional\ groups\ that\ are\ still\ unoccupied$

$N_{tot} \dots total\ number\ of\ surface\ functional\ groups$

4. The GPC shall be related to the number of surface functional groups that have reacted with a precursor according to:

$$GPC_{(t)} = G * N_{ocp(t)}/N_{tot} \quad Eq\ 5$$

$G \dots GPC\ in\ the\ saturation\ regime$

Combining Eq 2 and Eq 3 one obtains the following differential equation:

$$\frac{dN_{ocp(t)}}{(N_{tot} - N_{ocp(t)})} = p_0 * dt \quad Eq\ 6$$

Solving Eq 6 according to the boundary conditions in Eq 4 one obtains:

$$N_{ocp(t)} = N_{tot} * (1 - exp(-p_0 * t)) \quad Eq\ 7$$

Finally, exploiting Eq 5 one obtains the equation for the GPC as a function of the precursor exposure time:

$$GPC_{(t)} = G * \frac{N_{ocp(t)}}{N_{tot}} = G * (1 - exp(-p_0 * t)) \quad Eq\ 8$$

G and p_0 can be used as fitting parameters in order to represent the saturation curve by Eq 8. G can then be used to extrapolate the GPC when every surface functional group has been occupied giving an estimation for the GPC in complete saturation.

For the GPC as a function of the purging time the saturation curve can be explained in the following way.

During the purging step, the connections between the vessels containing the precursor gases and the vacuum chamber are closed. The precursor molecules from the last exposure step which are still inside the reactor are carried out of the reactor towards the vacuum pump with the help of the purging gas.

For short purging times, not all of the precursor molecules from the last step can be carried out of the reactor. Therefore, in the next deposition step, there are two different precursor species inside the reactor at the same time. This causes reactions in the gas phase between the different precursor species which leads to a CVD like growth where more than a single monolayer is deposited during a single deposition step leading to an increased GPC.

For longer purging times more and more precursor molecules can be removed out of the reactor during a single purging step. Therefore, fewer reactions take place in the gas phase in the next deposition step and the GPC decreases.

When the purging time is long enough almost all the precursor molecules can be removed out of the reactor during the purging step and further reactions can only take place at the sample surface during the next exposure step. One is then talking of the saturation regime of the purging step.

Similar to the precursor exposure step one can describe the situation via a mathematical model which requires the following assumptions:

1. The rate at which one precursor molecule leaves the reactor during a purging time increment is constant:

$$\frac{dN}{dt} = C \quad Eq\ 9$$

$N \ldots number\ of\ particles\ leaving\ the\ reactor\ in\ dt$

$C \ldots rate\ at\ which\ particles\ leave\ the\ reactor$

$t \ldots purging\ time$

Eq 9 holds in case of a reactor that contains exactly 1 particle at all times.

2. The number of precursor molecules leaving the reactor in a time increment is proportional to the current number of molecules inside the reactor and the rate at which one particle leaves the reactor.

$$dN_{purg(t)} = N_{gas(t)} * dN = N_{gas(t)} * C * dt \quad Eq\ 10$$

$N_{purg(t)} \dots number\ of\ molecules\ being\ purged\ out\ of\ the\ reactor$

$N_{gas(t)} \dots number\ of\ molecules\ inside\ the\ reactor$

3. The boundary conditions are:

$$N_{gas(t)} = N_{tot} - N_{purg(t)} \quad Eq\ 11$$

$$N_{purg(t=0)} = 0;\ N_{purg(t \to \infty)} \to \infty \quad Eq\ 12$$

$N_{tot} \dots total\ number\ of\ precursor\ particles\ in\ the\ system\ at\ t = 0$

4. The GPC can be split up in one part coming from reactions in the gas phase and subsequent deposition to the sample surface (CVD) and one part coming from reactions at the sample surface (MLD). For the reactions at the sample surface, a full monolayer coverage is assumed.

$$GPC_{(t)} = G + GPC_{(t)}^{CVD} \quad Eq\ 13$$

$GPC_{(t)}^{CVD} \dots film\ growth\ due\ to\ reactions\ in\ the\ gas\ phase$

$G \dots film\ growth\ due\ to\ reactions\ with\ the\ surface\ functional\ groups$

5. $GPC_{(t)}^{CVD}$ is related to the number of precursor molecules that remain in the reactor after the purging step:

$$GPC_{(t)}^{CVD} = N_{gas(t)} * f \quad Eq\ 14$$

$f \dots factor\ of\ proportionality$

Combining Eq 10 & Eq 11 one obtains the following differential equation:

$$\frac{dN_{purg(t)}}{dt} = C * (N_{tot} - N_{purg(t)}) \quad Eq\ 15$$

Solving Eq 15 for the boundary conditions given by Eq 12 one obtains:

$$N_{purg(t)} = N_{tot} * (1 - exp(-C * t)) \quad Eq\ 16$$

Combining Eq 11 & Eq 13 finally gives the fitting function for the purging saturation curve:

$$GPC_{(t)} = G + GPC_{max}^{CVD} * exp(-C * t) \quad Eq\ 17$$

With the following substitution:

$$GPC_{max}^{CVD} \equiv f * N_{tot} \quad Eq\ 18$$

Analog to the precursor exposure step G; GPC_{max}^{CVD} and C can be used as fitting parameters and with the help of G the GPC in saturation can be extrapolated.

It is important to notice that in case of a proper operating MLD process the fitting parameter G is the same for each of the four saturation curve. This gives a strong criterion for a self-limiting deposition process.

Furthermore, one must notice that also for long purging times there remains a little fraction of CVD-like growth. This follows from the fact that one can never remove all of the precursor molecules out of the system during a purging step, hence there will always be reactions in the gas phase. The structure of Eq 17 mirrors this fact. Analogue, also for long precursor exposure times it is unlikely to occupy every single surface functional group, leading to a converging but ever growing GPC as a function of the precursor exposure time in Eq 8. Therefore, there is no exact finite value for the minimum exposure & purging times that define the saturation regime. Rather the minimum values for the exposure & purging times in saturation are estimated in the region where the GPC changes only within its measuring error.

Generally, there is no restriction on the order in which the four saturation curves are measured. However, one can save a lot of time by measuring the saturation curves for the purging times before the saturation curves for the precursor exposure times. The reason for this is that the purging times for saturation tend to be orders of magnitude longer than the precursor exposure times.

From the purging saturation curves, one can read out the minimum purging times that are considered to be in the saturation regime. These minimum purging times can then be used to measure the saturation curves for the precursor exposure times.

The saturation curves can be measured in the following way:

EG purging saturation curve

The precursor exposure times and the DEZ purging time are set to very high values so they can be assumed to be in the saturation regime. The GPC is then measured as a function of different EG purging times. The EG purging time is increased until the GPC saturates. From this saturation curve, the minimum EG purging time for CVD free growth can be estimated.

DEZ purging saturation curve

The precursor exposure times are set to very high values and can be assumed to be in the saturation regime. The EG purging time is set to its minimum value for saturation, according to the EG purging saturation curve. The GPC is measured as a function of different DEZ purging times. The DEZ purging time is increased until the GPC goes in saturation. From this saturation curve, the minimum DEZ purging time for CVD free growth can be estimated.

EG exposure saturation curve

The purging times are set to their minimum values for saturation. The DEZ exposure time is set to a very high value and can be assumed to be in saturation. The GPC is measured as a function of different EG exposure times. The EG exposure time is increased until the GPC saturates. From this saturation curve, one can estimate the minimum EG exposure time that provides a complete monolayer coverage of EG during the exposure step.

DEZ exposure saturation curve

The purging times and the EG exposure time are set to its minimum values for saturation. The GPC is measured as a function of different DEZ exposure times. The DEZ exposure time is increased until the GPC saturates. From this saturation curve, one can estimate the minimum DEZ exposure time that provides a complete monolayer coverage of DEZ during the exposure step.

2.1.2 Zincone Films

Zincone films produced with DEZ and EG, are promising candidates in order to create conformal thin films of porous ZnO. Although the formation of porous ZnO with this technique has already been observed [11] there has been little research in this field. Especially structural changes, such as crystallization, during the heating of these films are barely investigated.

The schematic structure of a Zincone film deposited via MLD is shown below:
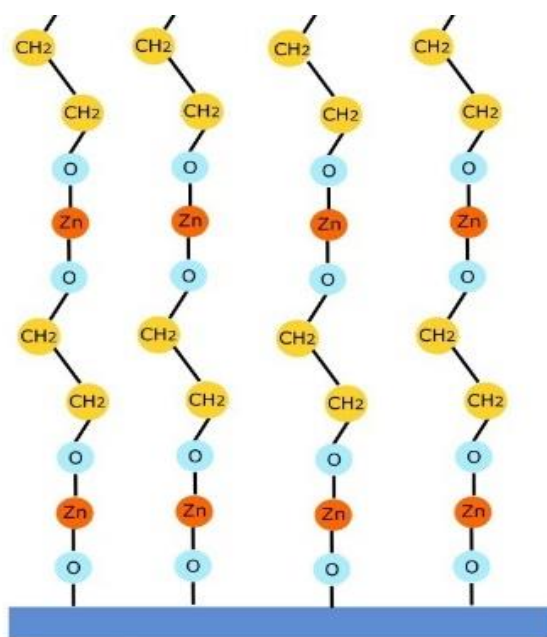
Figure 5: Zincone film formed with DEZ and EG

According to Figure 5, the GPC should be on the order of the length of both precursor molecules. Yet, experiments measuring the GPC show that the GPC is usually smaller than the length of the precursor molecules without their functional groups. This is due to the fact that the molecules that form the alternating monolayers tilt with respect to the surface normal. Longer organic precursor molecules are especially likely to tilt, causing a growth that is not perpendicular to the surface [7], [12]. On the other hand, in a self-limiting MLD process that avoids CVD growth, the GPC can never be bigger than the length of the two precursor molecules without their functional groups.

Due to the bending of the organic precursors, both functional groups of the organic precursor can react with the surface (Figure 6), reducing the number of available surface functional groups in the next deposition step [7], [8], [12]. This further reduces the GPC compared to an ideal model where every precursor molecule reacts only with one of its functional groups.
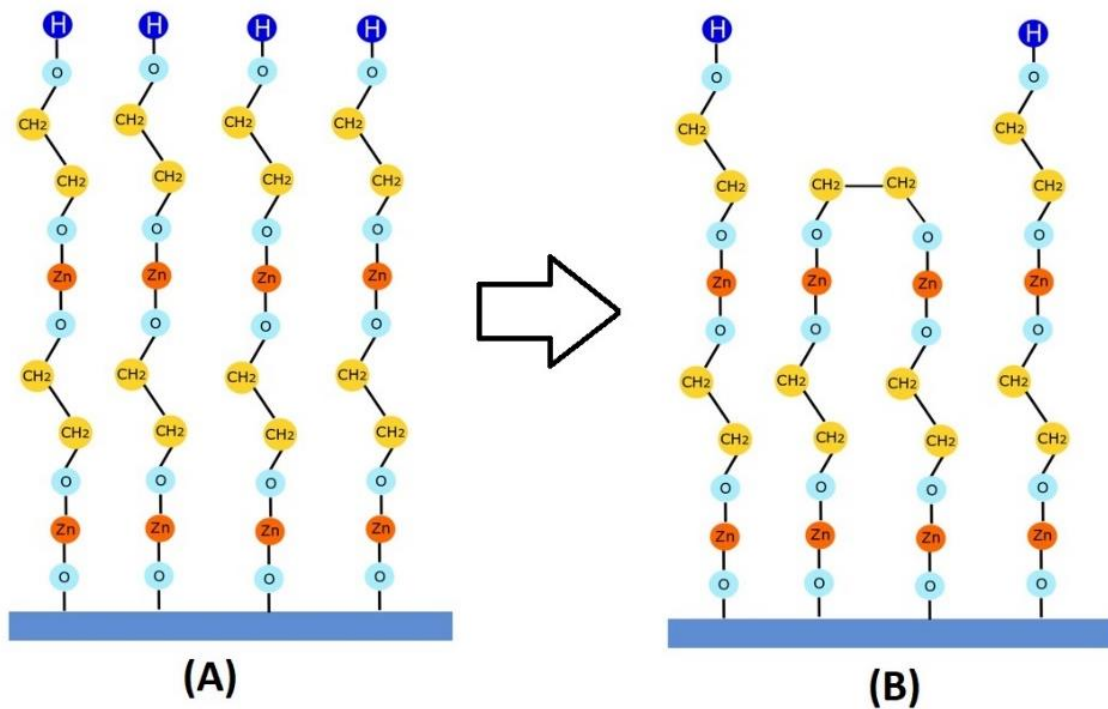
Figure 6: (A) Single bonds between the surface and EG molecules; (B) Double bonds between EG molecules and the surface limiting the number of surface functional groups
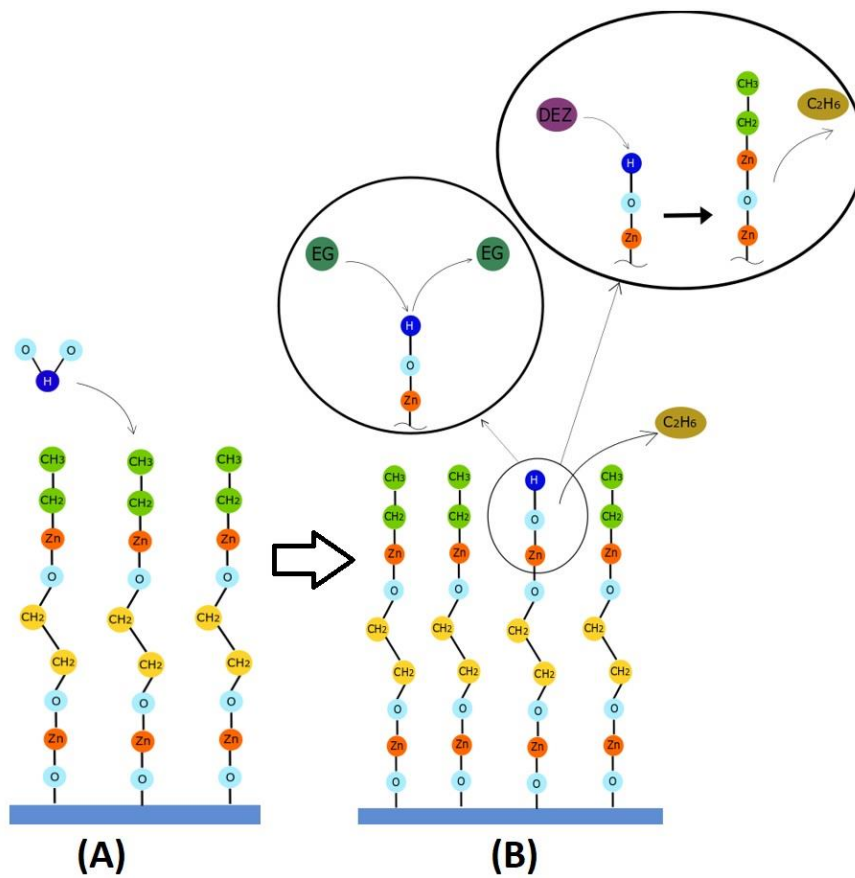
Figure 7: (A) Water reacting with DEZ surface functional groups forming OH surface groups (B) OH surface groups hinder EG surface reactions and causes ZnO formation

Also, reactions with water decrease the GPC and disrupt a proper growth of the alternating metal organic film structure [8], [13]. As shown in Figure 7 water can react with an ethyl surface group after the DEZ exposure step according to Rct 3:

$$R - OZn(C_2H_5) + H_2O \ \rightarrow \ R - OZnOH + C_2H_6 \quad Rct\ 3$$
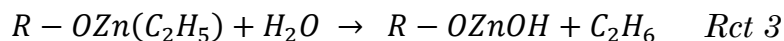
During this reaction the ethyl surface group is replaced by an OH group and ethane is emitted as a by-product. In the next EG exposure step, this surface OH group prevents EG gas molecules from attaching to the surface. In a further DEZ exposure step a DEZ molecule can attach to the OH group forming a classical zinc oxide bond at the surface, hindering the growth of the required organic layer in between zinc layers.

Therefore, in order to create the desired metal-organic hybrid structure of Zincone, water strictly has to be excluded from the reactions at the surface. This requires a proper vacuum system with an appropriately low leak rate.

Not only during the film growth but also in case of an already deposited Zincone film, reactions with water cause a structural change of the film [8], [10], [12], [14]. Such degradation processes are observed when Zincone films are exposed to ambient air: Water from the ambient can infiltrate the films and changes the chemical composition by hydrolyzing the film resulting in zinc oxide, zinc hydroxide and carbon remnants [8]. The hydrolyzing process breaks existing bonds inside the Zincone film and results in the formation of enolate-type vinyl ether species as it is also observed for alucone polymer films deposited with trimethylaluminum and ethylene glycol [14].

2.1.3 Porous Crystalline ZnO from Zincone Films

By heating the Zincone films the weakly bond organic content can be removed (Figure 8). Oxygen being present during the heating process is likely to react with the dimethylene group of the Zincone film according to Rct 4 favoring the removal of the organic part from the film. The removal of the dimethylene bridge results in the formation of vacancies inside the remaining film structure that contains mainly zinc and oxygen.

Methylene oxidation

$$R_1 - (CH_2)_2 - R_2 + 3O_2 \rightarrow R_1 + R_2 + 2CO_2 + 2H_2O \quad Rct\ 4$$
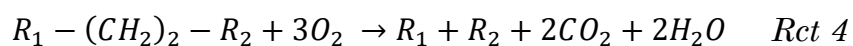
However, this does not yet provide the desired crystalline zinc oxide structure but simply an amorphous structure of zinc and oxygen separated by vacancies.

In order to obtain the desired crystal structure, the material is heated further. With increasing temperature, the zinc and oxygen atoms can rearrange into an ordered crystal structure, retaining some empty space inside the material.
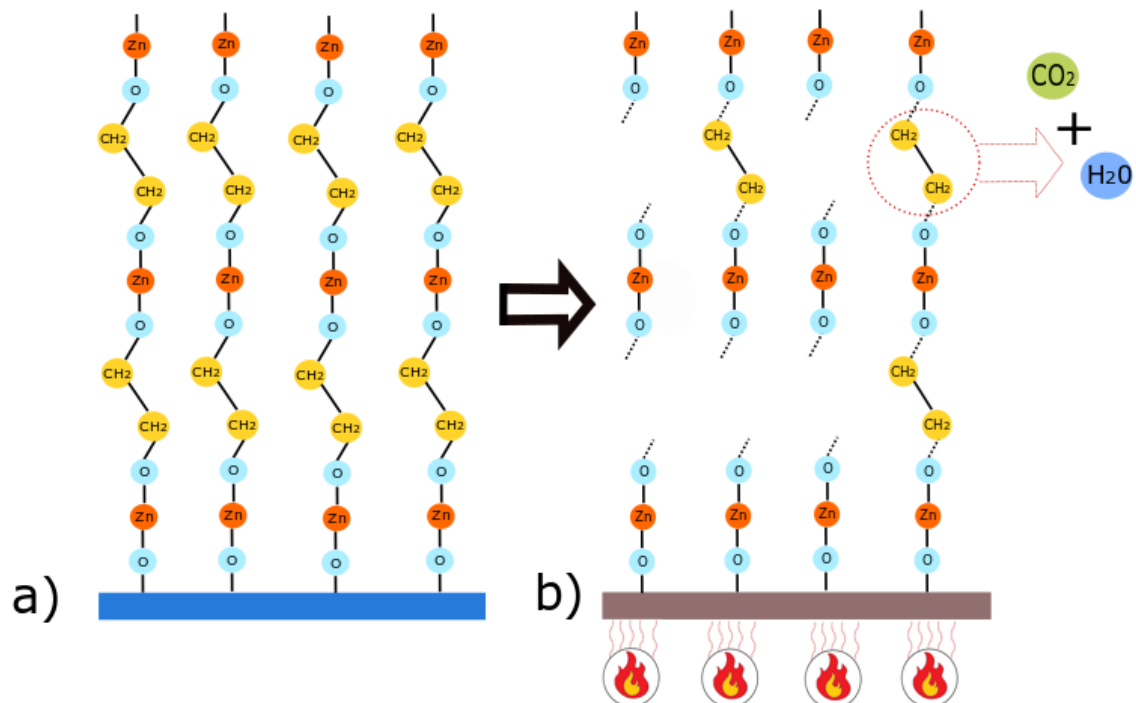
Figure 8: Scheme of the synthesis of porous ZnO

2.2 CHARACTERIZATION METHODS

2.2.1 Fourier Transform Infrared Spectroscopy (FTIR)

FTIR is a powerful technique in order to gain information about the chemical composition of a material, exploiting the quantized nature of intermolecular movement. It allows the measurement of the absorption spectrum of a substance for infrared (IR) light. Absorption in the IR is mostly related to the excitation of stretching and bending modes of covalent bonds which are, thanks to quantum mechanics, discretized. Hence, specific bonds show unique features in the absorption spectrum, in this way allowing one to specify the chemical composition of the absorbing material. However, many features in IR absorption spectra are not clearly assignable and leave open space for multiple interpretations. A detailed insight into the intricacies of FTIR can be found in [15].

Using a Michelson interferometer offers the great advantage to acquire a whole IR absorption spectrum using an IR light source that emits a broadband spectrum rather than monochromatic electromagnetic waves, enabling a rapid data acquisition. A schematic sketch of the Michelson interferometer is depicted in Figure 9.
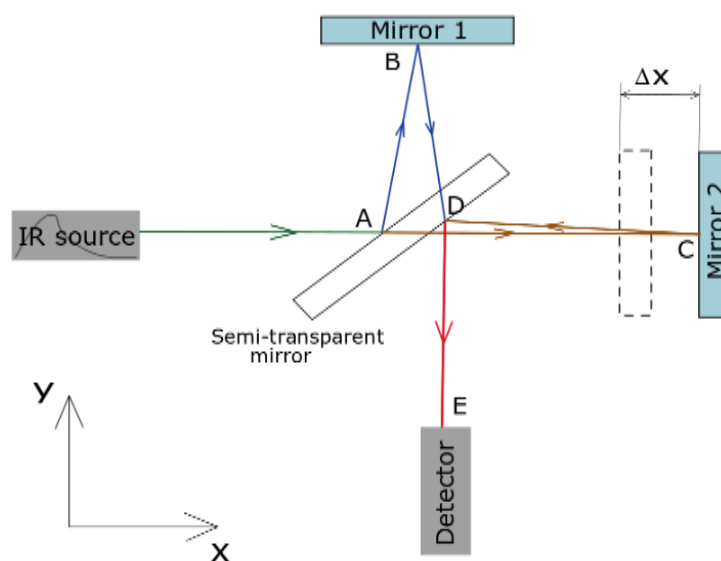
Figure 9: Michelson interferometer

The IR source emits broadband infrared radiation towards a semi-transparent mirror (A). At the semi-transparent mirror, the beam splits apart subsequently traveling toward two different mirrors. At each mirror, the according light beam gets reflected (B & C). After reflection at the two mirrors, the beams recombine at the semi-transparent mirror (D) finally traveling toward a detector (E). The path difference ($2\Delta x$) between the two beams when recombining in D can be adjusted by moving the

second mirror along the x-direction. When the path difference between the two beams is an integer number of the wavelength one can observe constructive interference. Hence, by varying the path difference one can modulate the frequencies within the broadband IR spectrum for which constructive interference takes place. Therefore, the intensity of the whole broadband IR spectrum can be measured with a detector as a function of the displacement of the second mirror (Δx). By Fourier transforming the measured intensity with respect to the displacement one obtains the intensity as a function of frequency. Thus, one can represent the spectral composition of the broadband IR light emmited by the source. If then a sample is brought into the pathway of the recombined beam one can obtain the IR absorbtion spectrum of this sample by simply comparing the spectra measured with and without the light absorbing sample in the pathway of the beam. For a detailed insight into how Fourier transform is applied to the measured data see [15].

2.2.2 X-Ray Diffraction (XRD)

XRD allows for the investigation of the crystalline structure of a thin film, interpreting interference patterns of X-rays diffracted from the crystal. To be exact, XRD measures the reciprocal lattice vectors in the direction of the surface normal of the thin film [16]. For this purpose, the sample is irradiated by a monochromatic X-ray beam at a defined angle θ. The intensity of the diffracted beam is measured at the same angle (specular condition). For elastic scattering, this means that the absolute value of the wave vector does not change due to diffraction and the scattering vector is in the direction of the surface normal (Figure 10, Eq 19). At the Bragg angle θ_B the condition for constructive interference is fulfilled, characterized by a maximum measured for the intensity of the diffracted beam. Consequently, the scattering vector at the Bragg angle is equivalent to a reciprocal lattice vector (Eq 20). Accordingly, one can measure the reciprocal lattice in the direction of the surface normal and therefore reconstruct the distance of net planes parallel to the surface. The values for the interplanar distance can be calculated from the Bragg angles according to Eq 21.
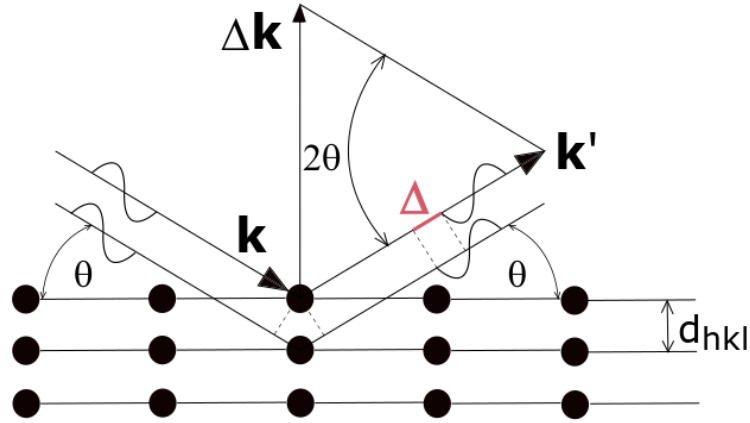
Figure 10: XRD scheme

$$\boldsymbol{k} - \boldsymbol{k'} = \Delta \boldsymbol{k} \qquad Eq\ 19$$

$$\Delta \boldsymbol{k}_{(\theta_B)} = \boldsymbol{G} \qquad Eq\ 20$$

$$n * \lambda = 2 * d_{hkl} * sin(\theta_B) \qquad Eq\ 21$$

$$n \dots integer\ number$$

$$\lambda \dots beam\ wavelength$$

$$d_{hkl} \dots netplane\ distance$$

$$\Theta_B \dots Bragg\ angle$$

$$\Delta \boldsymbol{k} \dots scattering\ vector$$

$$\boldsymbol{G} \dots. reciprocal\ lattice\ vector$$

The interference condition for the diffracted X-ray beam at a certain Bragg angle is theoretically defined for a crystal of infinite size. In this case, the intensity measured as a function of the incident angle would show intensity peaks with the shape of a delta distribution. Obviously, the crystals investigated with XRD are of finite size. This implies Bragg peaks of finite width. With the help of the Scherrer equation (Eq 22) the crystallite grain size can be related to the full width at half maximum of the according Bragg peak:

$$L = K * \frac{\lambda}{\Delta(2\Theta) * cos(\Theta_B)} \quad Eq\ 22$$

$$L \dots crystallite\ size\ perpendicular\ to\ the\ surface$$

$$K \dots form\ factor\ \sim 1$$

$$\lambda \dots beam\ wavelenth$$

$$\Theta_B \dots scattering\ angle\ of\ measured\ diffraction\ peak$$

$$\Delta(2\Theta) \dots full\ with\ at\ half\ maximum\ of\ measured\ diffraction\ peak$$

Further details on XRD can be found in [16], [17], [18].

2.2.3   X-Ray Reflectivity (XRR)

In XRR, thin films are investigated with respect to their thickness, electron density, and roughness. Furthermore, applying a proper model for the chemical composition of the film allows for the calculation of the mass density, based on the measured electron density. The measuring principle of XRR is to irradiate the thin film with a monochromatic X-ray beam at a very low incident angle α and recording the intensity of the reflected beam under specular conditions. Considering the experimental setup, XRR differs from XRD only in terms of the range of the incident angle, which is much smaller in case of XRR. Measuring the intensity of the reflected beam as a function of the incident angle yields the characteristic XRR spectrum of the thin film.

The subsequent introduction in the principles of XRR mainly follows [19], [20], and [21].

XRR spectra show several characteristic features which correlate to the different properties of the thin film. First of all, at the critical angle, below which there is total external reflection of the X-ray beam out of the film, one can observe a rapid drop in the intensity of the reflected beam. Snell's law together with an appropriate model for the complex index of refraction in the X-ray regime enables for calculating the electron density from the critical angle. Since the frequency of X-rays is much higher than the resonance frequency for electronic polarization (see 2.2.4.1), the real part of the refractive index is slightly less than one. Hence, it is reasonable to write for the complex index of refraction as:

$$n = 1 - \delta + i\beta \qquad Eq\ 23$$

$$\delta \ldots dispersion\ term$$

$$\beta \ldots absorption\ term$$

In a simple model, the dispersion term can be approximated by:

$$\delta = \frac{r_e \lambda^2}{2\pi} * \rho_e \qquad Eq\ 24$$

$$r_e \ldots classical\ electron\ radius$$

$$\rho_e \ldots spatial\ electron\ density$$

$$\lambda \ldots X-ray\ beam\ wavelength$$

More sophisticated models introduce atomic form factors for the description of the refractive index, taking into account that electrons in different bond states correspond to different resonance frequencies (see [21]). Such models require knowledge about the chemical composition of the investigated film, nevertheless allowing for the determination of the mass density from the measured electron density.

Snell's law correlates the refractive index to the incident angle and the angle of transmission:
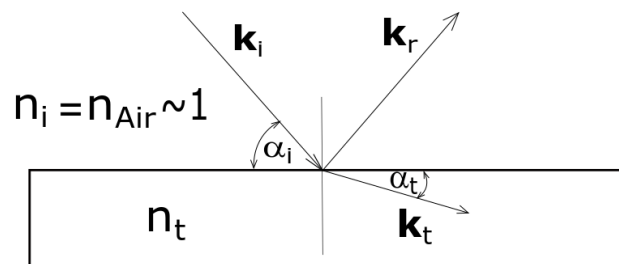
Figure 11: Snell's law

$$n_i * cos(\alpha_i) = n_t * cos(\alpha_t) \quad Eq\ 25$$

For a refractive index of the film n_t that is smaller than one in the X-ray regime, there is total external reflection of the X-ray beam out of the film, in case of an incident angle α_i that is smaller than the critical angle α_{crit}. At the critical angle, the beam starts to penetrate into the film. Hence, at the critical angle, the angle of transmission is zero. Regarding that the absorption term ß is negligibly small compared to the dispersion term δ and that α_{crit} is relatively small, allowing for a Taylor expansion of the cosine terminated after the 2nd order, one can combine Eq 24 and Eq 25 which yields the relationship between the critical angle and the electron density:

$$\rho_{elec} = \left(\frac{\alpha_{crit}}{\lambda}\right)^2 * \frac{\pi}{r_e} \quad Eq\ 26$$

Furthermore, going beyond the critical angle, part of the X-ray beam can penetrate into the thin film. The transmitted beam undergoes multiple reflections within the thin film (Figure 12). Hence, part of the beam can leave the thin film again and interfere with the initial reflected beam. Constructive interference for the total radiation reflected from the sample can be observed when the optical pathway of the beam inside the thin film is equal to an integer number of the wavelength. Hence, in

reflection, intensity maxima, known as Kiessig fringes, appear periodically as a function of the incident angle, allowing for the determination of the layer thickness.

In case of a single layer covering the substrate, the total amplitude reflectivity can be calculated analytically from the Fresnel equations (Eq 27), taking into account the path difference Δ between the multiple reflected single beams (see [19]).
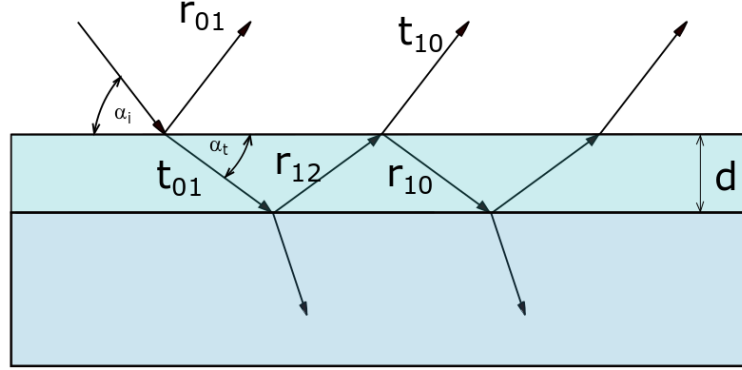
Figure 12: XRR reflection and transmission scheme

$$r = \frac{\alpha_i - \alpha_t}{\alpha_i + \alpha_t}, \quad t = \frac{2\alpha_i}{\alpha_i + \alpha_t} \qquad Eq\ 27$$

$$p^2 = e^{iq\Delta_{(d,\alpha_i)}}, \quad q = \frac{4\pi}{\lambda} * sin(\alpha_i) \qquad Eq\ 28$$

$$r_{Single(\alpha_i,d)} = r_{01} + t_{01}t_{10}r_{12}p^2 + t_{01}t_{10}r_{10}r_{12}^2p^4 + \cdots = \frac{r_{01} + r_{12}p^2}{1 + r_{01}r_{12}p^2} \qquad Eq\ 29$$

$$r, t \ldots reflectivity, transmissivity\ of\ a\ single\ beam$$

$$r_{Single} \ldots total\ amplitude\ reflectivity$$

$$\Delta_{(d,\alpha_i)} \ldots path\ difference\ between\ reflected\ single\ beams$$

$$q \ldots scattering\ vector$$

The reflectivity (Eq 29) relates the periodic intensity of the reflected beam to the film thickness. For multiple layers of different composition on top of the substrate, the calculation for the total amplitude reflectivity must be calculated recursively by the so-called Parratt formalism ([22]).

Also, the surface and interface roughness can be derived from the angular dependence of the reflected beam intensity. Roughness causes off-specular scattering and destructive interference of the reflected and transmitted beam. This leads to a decreased intensity of the reflected X-ray beam([19]). The roughness can be taken into account by approximating the film thickness with the help of a Gaussian-distribution and applying this distribution for fitting a measured XRR spectrum. The differential cross section of the scattering process, describing the interaction between the X-rays and matter, allows for the quantification of the roughness. This differential cross section is proportional to the scattered intensity. Several formalisms exist for describing scattering processes predicting a decrease in intensity of the reflected beam for increasing incident angles α. According to [22] the Fresnel reflectivity is reduced by a factor $e^{-q^2\sigma_r^2}$, where q is the scattering vector (Eq 28) and σ_r^2, as the variance of the thickness, describes the roughness. This dependency on the scattering vector illustrates the exponential decay of the reflected intensity and enables for using the roughness as a fit parameter when fitting the measured XRR spectra. A detailed insight into the Parratt algorithm and possible scattering formalism can be found in [22].

Summarising, three different material properties of the film can be assigned to three different characteristic features in the XRR spectrum. First of all, the electron density corresponds to a rapid drop of the intensity of the reflected beam at the critical angle (in practice, the critical angle is usually measured as the angle where the intensity drops to half its initial value). The periodicity of the repeating peaks, known as Kiessig fringes, give information about the film thickness. Finally, the surface and interface roughness are related to the exponential decrease in the XRR spectrum for increasing incident angles.
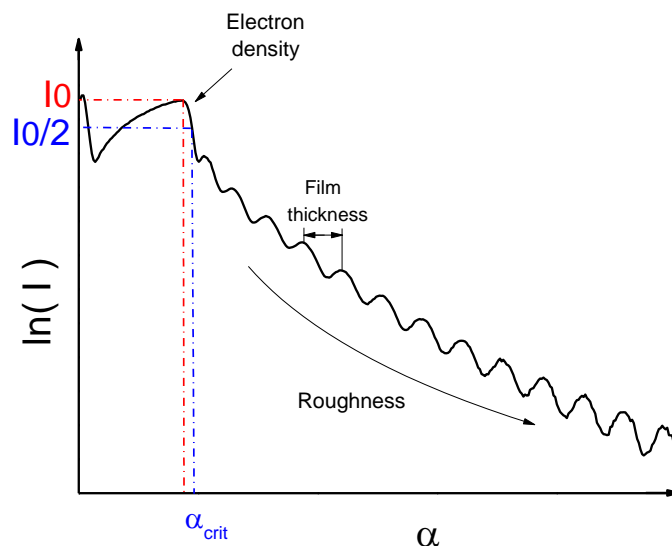
Figure 13: XRR characteristic features

2.2.4 Spectroscopic Ellipsometry (SE)

With the help of SE, one can determine the refractive index and thickness of the thin film. The measuring principle of ellipsometry is to shine linearly polarised light onto a sample and measuring the amplitude ratio Ψ and phase shift Δ between the perpendicular and parallel part of the electric field in reflection with respect to the wavelength of light (Figure 14). In case of a single reflection, the amplitude ratio and phase shift are related to the complex index of refraction by the Fresnel equations. Applying the Fresnel equations to multiple reflections at different layer interfaces allows for the theoretical calculation of the quantities measured with SE, depending on the index of refraction and the thickness of the layers. Hence, using appropriate models for the real and imaginary part of the index of refraction of the layers allows for fitting the refractive index and film thickness to the measured data. A detailed insight into the principles of ellipsometry and the used fitting software can be found in [23] & [24].
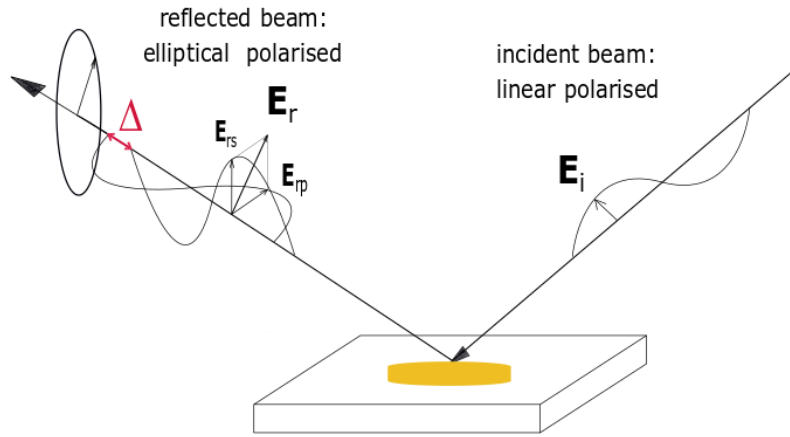
Figure 14: Spectroscopic ellipsometry scheme

$$tan(\Psi)\, e^{i\Delta} = \frac{r_p}{r_s} = \frac{\dfrac{E_{rp}}{E_{ip}}}{\dfrac{E_{rs}}{E_{is}}} \qquad Eq\ 30$$

$$\Psi \dots amplitude\ ratio$$

$$\Delta \dots phase\ shift$$

For a transparent material the Cauchy model is commonly used to describe the wavelength dependency of the (real) refractive index:

$$n_{(\lambda)} = A + \frac{B}{\lambda^2} + \frac{C}{\lambda^4} \quad Eq\ 31$$

Absorption of light within a material can be described by the extinction coefficient which can be simplified for partly transparent materials to:

$$k_{(\lambda)} = k_{amp} * exp(\alpha * (E_{(\lambda)} - E_{edge})) \quad Eq\ 32$$

However, for a perfect transparent film, the extinction coefficient can be set to zero. This is an acceptable approximation for thin films of Zincone and crystalline ZnO in case the maximum energy of the probing light spectrum lies below the bandgap energy of crystalline ZnO. Hence, for the investigation of crystalline ZnO, the minimum wavelength of the probing light was chosen to 450 nm while the band gap of crystalline ZnO lies around 375 nm (see 4.2.1.4).

$$n \ldots refractive\ index$$

$$A, B, C \ldots fitting\ parameters$$

$$k_{(\lambda)} \ldots extinciton\ coefficient$$

$$k_{amp}, \alpha, \ldots fitting\ parameters$$

$$E_{edge} \ldots band\ edge$$

2.2.4.1 Interpretation of the Refractive Index

Spectroscopic ellipsometry enables for measuring the refractive index of a thin film as a varying parameter during an experiment. To make a statement on the structural change of the film during the experiment it is convenient to relate the refractive index to more intuitively accessible quantities. This can be achieved with the help of a classical model for the electric susceptibility of a material, namely the harmonic oscillator model. A detailed insight into this model can be found in [25].

To begin with, for a dielectric medium one can assume a simple spring oscillator model for a single charge which is in a bond state (might be an electron that is bound to an atom or a single ion in an ionic crystal lattice). For the displacement of the charge away from its equilibrium position ($\mathbf{x}$) one can write the equation of motion in the following way:

$$m * \frac{d^2 \mathbf{x}}{dt^2} + \gamma * \frac{d\mathbf{x}}{dt} + K * \mathbf{x} = q * \mathbf{E} \qquad Eq\ 33$$

The field of an electromagnetic wave at the location of the charge has the form:

$$\mathbf{E} = \mathbf{E_0}\, exp(i * \omega * t) \qquad Eq\ 34$$

The dipole moment generated by the charge displacement can be written as:

$$\mathbf{d} = q * \mathbf{x} \qquad Eq\ 35$$

Together with the charge density N, the polarisation density can be written as:

$$\mathbf{P} = N * \mathbf{d} \qquad Eq\ 36$$

Furthermore, the electric susceptibility is defined by:

$$\mathbf{P} = \varepsilon_0\, \chi * \mathbf{E} \qquad Eq\ 37$$

Combining Eq 35, Eq 36 & Eq 37 gives the following ansatz for solving Eq 33:

$$x_{(t)} = \frac{\varepsilon_0 \chi}{Nq} * \mathbf{E_0}\, exp(i * \omega * t) \qquad Eq\ 38$$

Inserting this into the equation of motion gives:

$$\chi = \frac{q^2 N}{\varepsilon_0 m} * \frac{1}{\dfrac{K}{m} - \omega^2 + i\dfrac{\gamma}{m}} \qquad Eq\ 39$$

Using the definitions for the resonance and plasma frequency leads to a very simple form of Eq 39:

$$\omega_0^2 = \frac{K}{m}, \quad \omega_p^2 = \frac{q^2 N}{\varepsilon_0 m} \qquad Eq\ 40$$

$$\chi = \frac{\omega_p^2}{\omega_0^2 - \omega^2 + i\dfrac{\gamma}{m}} \qquad Eq\ 41$$

Generally, there are three different mechanisms (see Figure 15) that can contribute to the susceptibility of a material, namely the electronic, ionic and orientation polarization ([18]).

$$\chi = \chi_e + \chi_{ion} + \chi_{orient} \qquad Eq\ 42$$
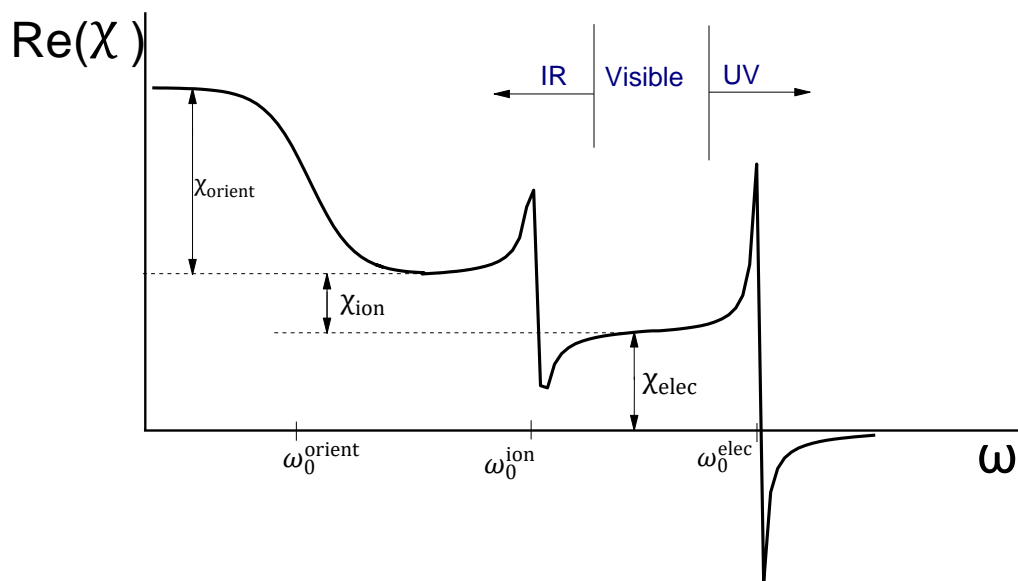
Figure 15: Electric susceptibility as a function of frequency

In the following one is interested in the refractive index measured with ellipsometry, which exploits light in the visible spectrum. This, in turn, means that the wavelengths used within ellipsometry are much higher than the resonance frequencies for ionic or even orientation polarisation. Therefore, the main part of the susceptibility comes from electronic polarisation and one can write:

$$\chi \rightarrow \chi_e \quad \omega_0 \rightarrow \omega_{0,e} \quad \omega_p \rightarrow \omega_{p,e} \qquad Eq\ 43$$

Using the definition of the refractive index and the dielectric constant:

$$n = \sqrt{\varepsilon_r \mu_r} \qquad Eq\ 44$$

$$\varepsilon_r = 1 + \chi_e \qquad Eq\ 45$$

Gives the refractive index of a non-magnetic material ($\mu_r = 1$):

$$n = \sqrt{1 + \frac{\omega_{p,e}^2}{\omega_{0,e}^2 - \omega^2 + i\frac{\gamma}{m_e}}} \qquad Eq\ 46$$

Neglecting the damping term ($\gamma \to 0$) one obtains a completely real refractive index:

$$n \to \sqrt{1 + \frac{\omega_{p,e}^2}{\omega_{0,e}^2 - \omega^2}} \qquad Eq\ 47$$

A fully real refractive index means that the extinction coefficient describing the adsorption properties of the material is zero. Therefore, Eq 47 holds for a transparent material.

Since the resonance frequency for electronic polarisation lies in the UV regime one can use the following approximation:

$$\omega_{0,e}^2 \gg \omega^2: \; n \to \sqrt{1 + \frac{\omega_{p,e}^2}{\omega_{0,e}^2}} \qquad Eq\ 48$$

Resubstituting the plasma and resonance frequencies for electronic polarisation finally leads to:

$$n = \sqrt{1 + \frac{e^2 N_e}{\varepsilon_0 K_e}} \qquad Eq\ 49$$

Eq 49 illustrates that the refractive index of a transparent dielectric in the visible spectrum depends mainly on the electron density N_e and the "spring constant" K_e which describes the mean binding energy of the electrons or more specifically is representative for the electronic polarizability.

However, in the derivation of the electric susceptibility, the contribution of the local polarization to the local electric field had been neglected in order to keep the structure of the derived refractive index fairly simple. This allows for an easy interpretation of the refractive index. To be absolutely precise, for the relationship between microscopic

polarization and macroscopic susceptibility, the Clausius Morsotti equation must be applied (see 2.2.5.1.1, [26]).

$$\boldsymbol{x} \dots charge\ displacement\ from\ equilibrium\ position$$

$$m \dots mass\ of\ a\ single\ charge$$

$$k \dots spring\ constant$$

$$\gamma \dots damping\ constant$$

$$q \dots charge$$

$$\boldsymbol{E} \dots\ electric\ field$$

$$\boldsymbol{d} \dots dipole\ moment$$

$$\boldsymbol{P} \dots polarisation\ density$$

$$\varepsilon_0 \dots vacuum\ permittivity$$

$$\varepsilon_r \dots relative\ permittivity$$

$$\chi \dots susceptibility$$

$$n \dots refractive\ index\ of\ the\ material$$

$$\omega_0 \dots resonance\ frequency$$

$$\omega_p \dots plasma\ frequency$$

$$m_e \dots electron\ mass$$

$$N_e \dots electron\ density$$

$$K_e \dots mean\ spring\ constant\ for\ bond\ electrons$$

2.2.5   Ellipsometric Porosimetry (EP)

Ellipsometric porosimetry (EP) allows measuring the number of vacancies inside the film which are accessible from outside the film (open porosity). The measuring principle of EP is to increase the pressure of a specific probing vapor in the atmosphere surrounding the sample while simultaneously measuring the refractive index of the sample with ellipsometry. With increasing pressure more and more probing vapor molecules adsorb in the pores inside the film. Since typically the refractive index of the probing vapor in a liquid phase is higher than the one of air, the propagating adsorption inside the pores causes an increase of the film's refractive index. One can then apply a so-called effective medium approximation (EMA) in order to calculate back the volume fraction of the condensed liquid inside the film from the measured index of refraction. When the pressure reaches the vapor pressure of the probing vapor, all the open pores of the film are filled with the condensate. In that case, the volume fraction of the liquid inside the film is equal to the fraction of open pores.
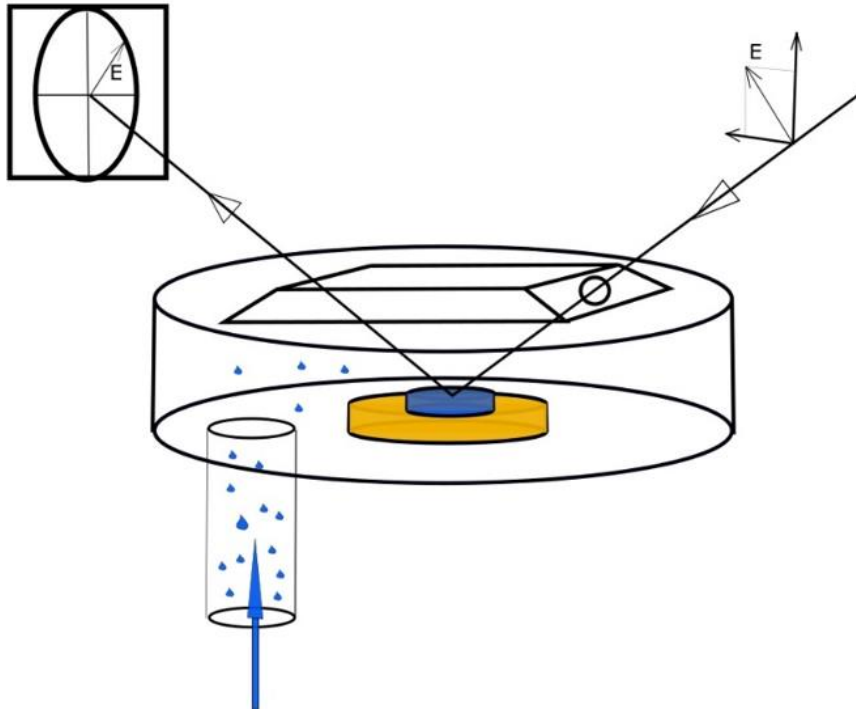
Figure 16: Ellipsometric porosimetry measurement principle

By measuring the refractive index of the film as a function of the probing vapor pressure, a pore size distribution can be obtained with the help of the Kelvin equation which relates the curvature of the surface of a liquid to its vapor pressure. Hence, the radius of the pores in which the probing vapor condenses can be related to the measured gas pressure. This together with a proper model for the shape of the pores allows for the calculation of the pore size distribution inside the film.

A detailed description of EMA, EP, and PSD can be found in [26] [27] [28].

2.2.5.1 Effective Medium Approximation (EMA)

The effective medium approximation allows calculating the volume fraction of a liquid inside vacancies of a porous film from the refractive index of the film. This, in turn, enables for the determination of the film's fraction of open porosity when applied to EP measurements and is the foundation for the calculation of a pore size distribution. In the following, a quick introduction into the EMA and its approach in EP is given. A short derivation of the Lorentz-Lorentz effective-medium formula (Eq 50) is illustrated in the subchapter 2.2.5.1.1.

First of all, the Lorentz-Lorentz effective-medium expression ([26]) for the effective dielectric function of a material that consists of two components, namely material A and material B with dielectric functions ε_a and ε_b respectively, can be written as:

$$\frac{\varepsilon_{eff} - 1}{\varepsilon_{eff} + 2} = \frac{V_a}{V}\frac{\varepsilon_a - 1}{\varepsilon_a + 2} + \frac{V_b}{V}\frac{\varepsilon_b - 1}{\varepsilon_b + 2} \quad Eq\ 50$$
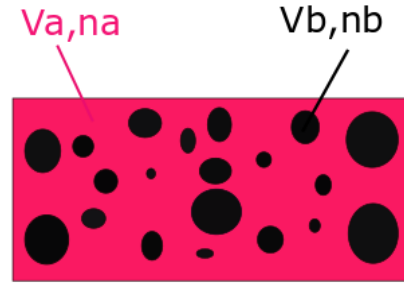
Figure 17: Two component material

For a non-magnetic material ($\mu_r = 1$) one finds:

$$n = \sqrt{\varepsilon_r * \mu_r}\ ;\ \mu_r = 1\ \rightarrow\ n = \sqrt{\varepsilon_r} \quad Eq\ 51$$

This implies that Eq 50 can be re-written for the refractive index as:

$$\frac{n_{eff}^2 - 1}{n_{eff}^2 + 2} = \frac{V_a}{V}\frac{n_a^2 - 1}{n_a^2 + 2} + \frac{V_b}{V}\frac{n_b^2 - 1}{n_b^2 + 2} \quad Eq\ 52$$

$\varepsilon_{a/b/eff} \ldots dielectric\ function\ of$ material a / material b / the mixture

$n_{a/b/eff} \ldots refractive\ index\ of$ material a / material b / the mixture

$V_a\ /\ V_b\ /\ V \ldots volume\ of$ material a / material b / the mixture

Eq 50 and Eq 52 can easily be generalized to systems containing more than two compounds.

In case of a porous film, the materials that compose the film are the pores and the host material which is ZnO, in our case. In general, the refractive index of the host material is often not known and for itself is very hard to measure. The big advantage of ellipsometric porosimetry is that the volume fraction of the pores inside the film can be measured without any knowledge of the host material's refractive index. For this purpose Eq 52 must be evaluated for two different cases:

1. <u>Air atmosphere</u>

In case the atmosphere around the sample does not contain any probing vapor that could adsorb inside the pores, these are filled with air. Therefore, the pore's refractive index can be chosen as $n_{pore} \sim 1$. If this is put into Eq 52 the pore term vanishes and one obtains:

Figure 18: Empty pores

$$\frac{n_0^2 - 1}{n_0^2 + 2} = \frac{V_{host}}{V} \frac{n_{host}^2 - 1}{n_{host}^2 + 2} \quad Eq\ 53$$

$n_0 \dots refractive\ index\ of\ the\ film\ measured\ in\ air\ atmosphere$

$n_{host} \dots refractive\ index\ of\ the\ host\ material$

$V_{host} \dots volume\ of\ the\ host\ material$

$V \dots volume\ of\ the\ total\ film$

2. <u>Probing vapor atmosphere</u>

In case the sample is exposed to a probing vapor, some pores can be filled with the condensed probing molecules. Obviously, the refractive index of these pores is then the refractive index of the condensed probing vapor, whereas the refractive index of the empty pores is still the one of air. Hence, Eq 52 cannot be simplified as in the case of empty pores and a term coming from the pores that are filled with the condensed probing vapor is present:
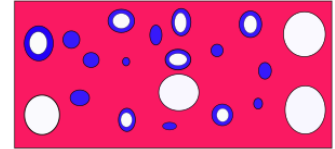
Figure 19: Partly filled pores

$$\frac{n^2 - 1}{n^2 + 2} = \frac{V_{probe}}{V} \frac{n_{probe}^2 - 1}{n_{probe}^2 + 2} + \frac{V_{host}}{V} \frac{n_{host}^2 - 1}{n_{host}^2 + 2} \quad Eq\ 54$$

$n \dots refractive\ index\ of\ the\ film\ measured\ in\ probing\ gas\ atmosphere$

$n_{probe} \dots refractive\ index\ of\ the\ condensed\ probing\ gas$

$V_{probe} \dots volume\ of\ the\ condensed\ probing\ gas\ inside\ pores$

Both Eq 53 and Eq 54 contain the same term describing the host material of the porous film. The two equations can be combined in order to eliminate this term. One then obtains a formula describing the volume fraction of the condensed probing vapor inside the pores.

$$\frac{V_{probe}}{V} = \frac{\dfrac{n^2 - 1}{n^2 + 2} - \dfrac{n_0{}^2 - 1}{n_0{}^2 + 2}}{\dfrac{n_{probe}{}^2 - 1}{n_{probe}{}^2 + 2}} \qquad Eq\ 55$$

Eq 55 describes the volume fraction of the condensate inside the pores as a function of only measurable quantities namely the refractive index of the whole thin film measured in air and vapor atmosphere and the well-known refractive index of the probing molecules in condensed state. In case of water vapor as the probing vapor one finds $n_{probe} = n_{H_2O}$.

2.2.5.1.1 Derivation of the Lorentz-Lorentz Effective-Medium Formula

This derivation mainly follows [26].

First of all, in order to relate the macroscopic electric susceptibility of a material to the microscopic polarizability of a dipole, one must derive an expression for the local electric field $\boldsymbol{E}_{loc}$ which is responsible for the induced dipole moment at each point of polarization. A formula for $\boldsymbol{E}_{loc}$ can be found by combing the contributions of both the macroscopic polarization density and the regular microscopic dipole lattice to the total microscopic electric field. As is well described in [26], in case of induced dipoles that are arranged on a simple cubic lattice one finds the following expression for the local electric field:

$$\boldsymbol{E}_{loc} = \boldsymbol{E} + \frac{\boldsymbol{P}}{3\varepsilon_0} \qquad Eq\ 56$$

Furthermore, it is evident to relate the microscopic induced dipole moment to the local electric field via the polarizability:

$$\boldsymbol{d} = \alpha * \boldsymbol{E}_{loc} \qquad Eq\ 57$$

Together with the density of microscopic dipoles N, one finds for the macroscopic polarization density:

$$\boldsymbol{P} = N * \boldsymbol{d} = \alpha * N * \boldsymbol{E}_{loc} \qquad Eq\ 58$$

Combinging Eq 57 and Eq 59 one finds:

$$P = \frac{N\alpha}{1 - \frac{N\alpha}{3\varepsilon_0}} E \qquad Eq\ 59$$

The electric susceptibility is defined by:

$$P = \varepsilon_0\, \chi_e\ E \qquad Eq\ 60$$

Wich allows to identify χ in Eq 59 as:

$$\chi_e = \frac{3N\alpha}{3\varepsilon_0 - N\alpha} \qquad Eq\ 61$$

Using the well, known relationship between the susceptibility and the dielectric function (see Eq 45) one can rewrite Eq 61 to the Clausius Morsotti formula:

$$\frac{\varepsilon_r - 1}{\varepsilon_r + 2} = \frac{N\alpha}{3\varepsilon_0} \qquad Eq\ 62$$

Now for a mixed material, containing two materials A & B with the according dipole polarizabilities α_A & α_B and dipole densities $\tilde{N}_A$ & $\tilde{N}_B$ in the mixed material one can modify Eq 58 to:

$$P = (\alpha_A\tilde{N}_A + \alpha_B\tilde{N}_B) * E_{loc} \qquad Eq\ 63$$

Using the same steps as before this yields the susceptibility and the dielectric function of the mixed material:

$$\chi_M = \frac{3(\alpha_A\tilde{N}_A + \alpha_B\tilde{N}_B)}{3\varepsilon_0 - (\alpha_A\tilde{N}_A + \alpha_B\tilde{N}_B)} \qquad Eq\ 64$$

$$\frac{\varepsilon_M - 1}{\varepsilon_M + 2} = \frac{\alpha_A\tilde{N}_A}{3\varepsilon_0} + \frac{\alpha_B\tilde{N}_B}{3\varepsilon_0} \qquad Eq\ 65$$

Now for the pure material A with the according dipole density N_A, Eq 62 gives:

$$\frac{\varepsilon_A - 1}{\varepsilon_A + 2} = \frac{N_A \alpha_A}{3\varepsilon_0} \qquad Eq\ 66$$

The density of type A dipoles in the mixed material $\tilde{N}_A$ can be related to the dipole density in the pure material N_A simply by the volume fraction of material A in the mixed bulk:

$$\tilde{N}_A = \frac{V_A}{V} N_A \qquad Eq\ 67$$

Analog, one finds for material B:

$$\frac{\varepsilon_B - 1}{\varepsilon_B + 2} = \frac{N_B \alpha_B}{3\varepsilon_0} \qquad Eq\ 68$$

$$\tilde{N}_B = \frac{V_B}{V} N_B \qquad Eq\ 69$$

Combining Eq 65, Eq 66, Eq 67, Eq 68 and Eq 69 yields the Lorentz-Lorentz effective-medium expression for the mixed material (see Eq 50):

$$\frac{\varepsilon_M - 1}{\varepsilon_M + 2} = \frac{V_A}{V} \frac{\varepsilon_A - 1}{\varepsilon_A + 2} + \frac{V_B}{V} \frac{\varepsilon_B - 1}{\varepsilon_B + 2} \qquad Eq\ 70$$

E ... *macroscopic electric field in matter*

E_{loc} ... *local electric field in matter*

d ... *dipole moment*

P ... *polarisation density*

α_A / α_B ... *polarizability of type A/B dipoles*

ε_0 ... *vacuum permittivity*

$\varepsilon_A / \varepsilon_B / \varepsilon_M$ ... *relative permittivity of material A/B/mixture*

χ_e / χ_M ... *electric susceptibility / in the mixed material*

$\tilde{N}_{A/B}$ ... *type A/B dipole density in the mixture*

$N_{A/B}$ ... *dipole density in pure material A/B*

V_A / V_B ... *volume of material A/B in mixture*

V ... *total volume of the mixture*

2.2.5.2 Pore size distribution

Besides the volume fraction of the pores filled with the probing vapor condensate, one can also determine the maximum radius of the pores that can still adsorb water at a certain probing vapor pressure. This allows the calculation of a pore size distribution.

The central equation for the pore size distributions in mesoporous materials is the Kelvin equation [27], [28]. It relates the curvature of a liquid (Figure 20) to its vapor pressure.
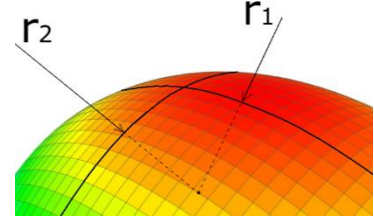
Figure 20: Curved liquid surface

$$\frac{1}{r_1} + \frac{1}{r_2} = \frac{RT}{\gamma V_m} * ln(\frac{p}{p_0}) \quad Eq\ 71$$

$$\gamma \dots surface\ tension$$

$$V_L \dots molar\ volume$$

$$p \dots vapour\ pressure\ for\ a\ liquid\ with\ a\ curved\ surface$$

$$p_0 \dots common\ vapour\ pressure\ for\ a\ flat\ liquid\ surface$$

$$r_{1/2} \dots liquid\ curvature\ radii\ on\ two\ perpendicular\ trajectories\ along\ the\ surface$$

The Kelvin Equation can be evaluated for a liquid that is adsorbed inside a cylindrical pore (Figure 21). In this case one finds a convex curvature ($r_1 < 0$) with:

and

$$|r_1| = r_{pore}\ \&\ r_2 \to \infty \quad Eq\ 72$$

$$\frac{1}{r_{pore}} = -\frac{RT}{\gamma V_M} * ln(\frac{p}{p_0}) \quad Eq\ 73$$
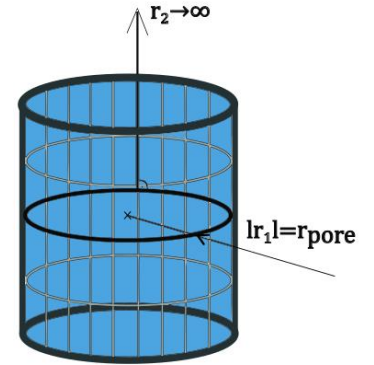
Figure 21: Liquid layer inside cylindrical pore

According to Eq 73, there is less vapor pressure for a liquid covering a pore with a smaller radius than for a bigger pore. This means that in smaller pores the probing vapor condenses at a lower pressure. Hence, with increasing pressure bigger pores adsorb the probing vapor until all pores are filled. In that case, the pressure reaches the common vapor pressure of the probing vapor for a flat surface.

Using water vapor as the probing vapor, the ratio between the vapor pressure of the curved and the flat surface is equal to the relative humidity, which can easily be measured:

$$\frac{p^{H20}}{p_0^{H20}} = RH \qquad Eq \ 74$$

Eq 73 & Eq 74 can be used to describe the maximum radius of the pores that are filled with water as a function of the relative humidity in the atmosphere surrounding the sample.

$$r_{pore} = \frac{\gamma * V_M}{R * T * \ ln(\frac{p_0}{p})} \qquad Eq \ 75$$
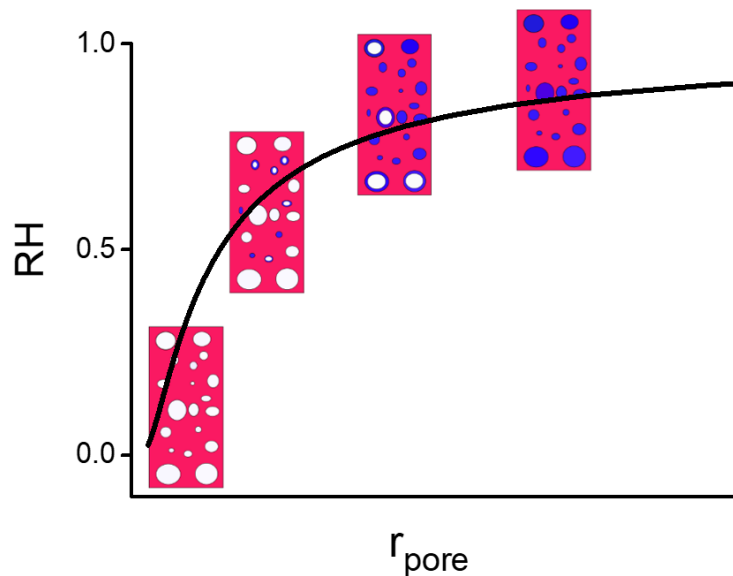
Figure 22: Relationship between maximum radius of water adsorbing pores and relative humidity

With the help of ellipsometry, the refractive index of the film can be measured as a function of the relative humidity. Applying Eq 55 and Eq 75 to such measurements allows one to relate the cumulative volume fraction of water inside the pores to their maximum radius. Yet, in terms of the pore size distribution, one is rather interested in the volume fraction of water inside pores of a defined radius. One can therefore simply take the derivative of the cumulative function with respect to the pore radius in order to obtain the pore size distribution (Eq 76, Figure 23).

$$dV_{ads(r_{pore})} = \frac{\partial V_{ads(r_{pore})}}{\partial r_{pore}} * dr_{pore} \qquad Eq\ 76$$

$V_{ads(r_{pore})}$ ... cumulative volume of water adsorbed in pores with a radius $r < r_{pore}$

$dV_{ads(r_{pore})}$ ... water volume adorbed in pores with radius $r \in (r_{pore}, r_{pore} + dr_{pore})$
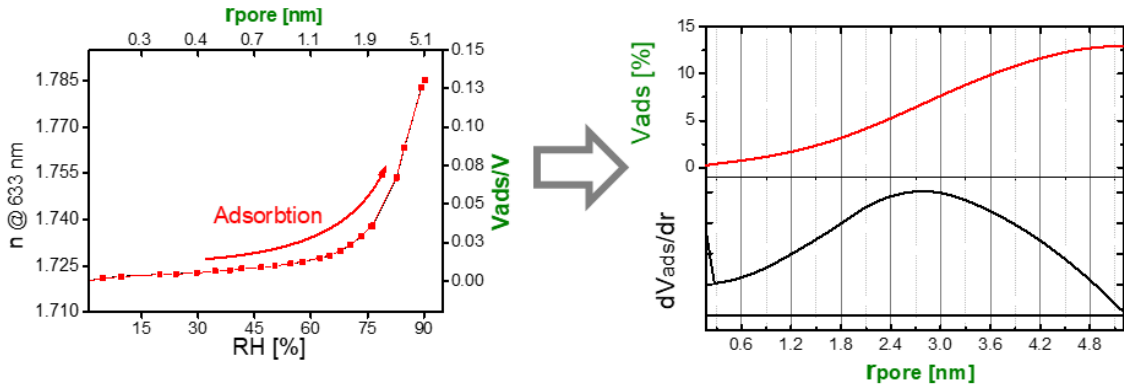
Figure 23: Derivation of the pore size distribution from an EP measurement

The pore size distribution obtained from the model described above holds in the adsorption regime of the EP measurement where the relative humidity is increased from 0 to 100%. In this case, the water adsorbs at the surface of the cylindrical pores and condenses to a cylindrical water film. However, in the desorption range, one finds a different situation since now the water desorbs from completely filled pores. Hence, the surface of the liquid-air interface is no longer cylindrical but rather like in a capillary, as shown in Figure 24. In this case, the description of the surface radii is more difficult since one requires the contact angle between water and the pore. Furthermore, groups reporting the derivation of a pore size distribution from the desorption regime of the EP measurement mainly use toluene as a probing vapor which has a lower intermolecular interaction as water vapor and is, therefore, more suitable for ellipsometric porosimetry ([27], [28]).
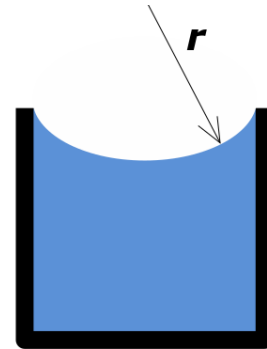
Figure 24: Water desorbing from pore

Moreover, in our system the relative humidity could not be decreased slow enough to obtain trustful data from the tardy humidity sensor, that responds to a relative humidity change with a temporal delay of more than one minute. Hence, in case of desorption, it was difficult to obtain trustful data points in the most important regime between 100 % and 70% relative humidity. Unfortunately, it is this humidity regime that is crucial for deriving a PSD in the mesoporous regime.

Since the water vapor measurements taken in the adsorption regime showed good results within a reasonable model for the pore's shape, no pore size distribution was calculated from the desorption regime of the EP measurements.
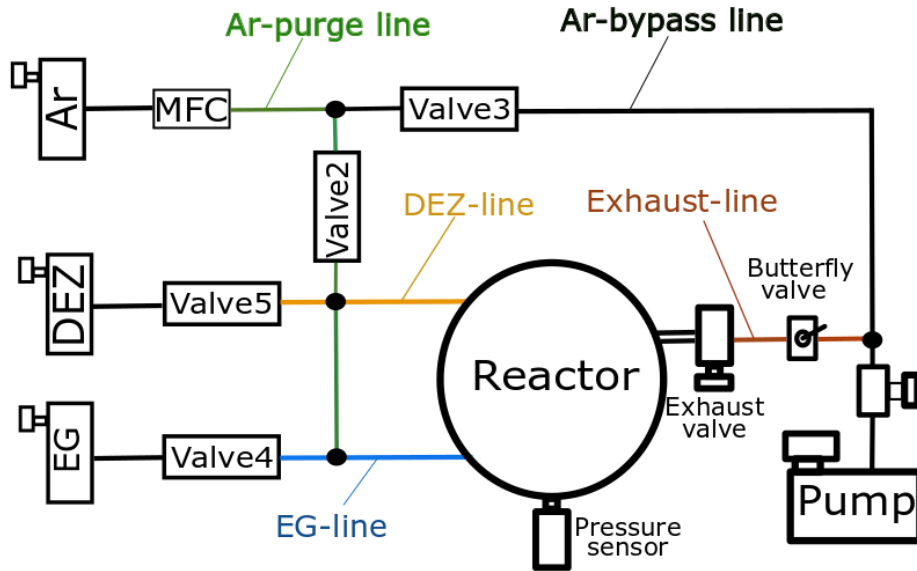
Figure 25: MLD system scheme

In order to enable the formation of thin films via MLD, a complete new deposition system was built within this master thesis. The schematic structure of the MLD system is illustrated in Figure 25. In principle, the setup consists of a reactor that is connected to both a rotary vane vacuum pump (Dev 10) and the vessels of the precursors and the purging gases. The reactor is separated from the precursors by valves that are triggered with the help of a microcontroller (Dev 7). For the connection between the precursor jars and the reactor special ALD valves were used (valve 4, valve 5: Dev 4) whereas for the purging gas lines simple mechanical valves were used (valve 2, valve 2: Dev 5). By setting the opening times of the valves with the help of the microcontroller (Dev 7) the precursor exposure times can be controlled. The flow rate of the purging gas is set with the help of a mass flow controller (MFC: Dev 6) that can be adjusted via a software (App 3). The pressure inside the reactor is constantly measured with a pressure sensor (Dev 11).

To provide a proper operating deposition process the MLD system has to fulfill several requirements. Especially when it comes to avoid condensation of the precursors inside the reactor and preventing water to take part in the chemical reactions, some measures must be taken. Furthermore, the precursor exposure times, the flow rate of the purging gas and the substrate temperature need to be controlled and a proper vacuum level needs to be established.

In order to fulfill these requirements, the following procedure can be applied.

3.1 REACTOR AND LINE HEATING TO PREVENT CONDENSATION

Condensation of the precursor molecules inside the reactor causes a major problem when it comes to preventing a CVD like growth. Condensed particles remain inside the reactor for long times and can barely be removed within reasonable purging times. The condensed precursor species is constantly outgassing inside the reactor for multiple MLD cycles resulting in an increased operating pressure (Figure 26).
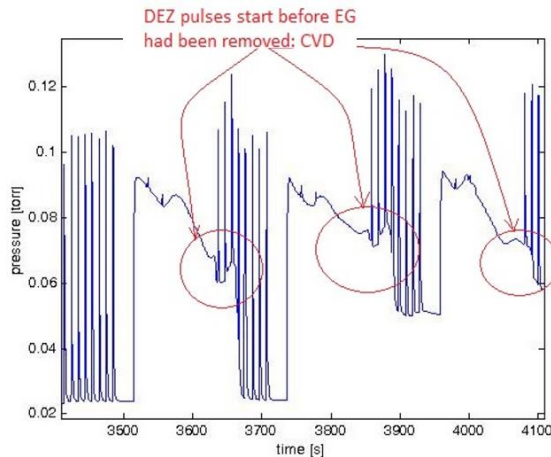
Figure 26: Condensed EG causing operating pressure increase

The outgassing of the condensate causes the simultaneous presence of both precursor types in the gas phase. This, in turn, is directly related to a CVD-like growth due to reactions in the gas phase (see 2.1.1).

To prevent condensation, a thermal gradient from low to high temperature has to be established on the precursor path from the vessel to the reactor. Especially, the ALD valve which is mounted directly on top of a heated EG precursor gas vessel (valve 4, Figure 25) demands precise heating in order to keep the valve temperature higher than the EG vessel temperature which is at 80°C (for the DEZ valve (valve 5, Figure 25) this is not a problem because DEZ has a higher vapor pressure at T_{room} and therefore needs no heating for evaporation). Otherwise, the precursor vapor condenses inside the EG valve. By opening the valve then, little droplets are shot into the system. These droplets are very hard to purge away because they remain inside the first part of the line connecting the EG vessel to the reactor. This part of the line (between valve 5 and valve 4, Figure 25) lies before the connection to the Ar-purging line and is therefore poorly purged.

The temperature of the several parts of the system was set with the help of heating wires (Dev 3). The whole system was then thermally isolated with aluminum foil. The temperature at which the several parts of the system are held can be found in Table 1.

Figure 27: MLD system before and after thermal isolation

MLD system element	Temperature °C
Reactor	110
Reactor top plate	90
DEZ gas vessel	25
EG gas vessel	80
EG valve (valve4)	85
DEZ valve (valve5)	25
Purging line valve (valve 2)	25
Bypass valve (valve 3)	25
Outlet valve	90
Butterfly valve	80
EG line	95
DEZ line	60
Outlet line	80
Ar-purge line	25
Ar-bypass line	25

Table 1: MLD system temperatures

With this setup, it is possible to heat up the reactor to its operating temperature within less than an hour (see Figure 28). Once in thermal equilibrium, the local temperature distribution along the reactor is very homogeneous within an error of $\Delta T_{reactor} = \pm 5\,°C$.
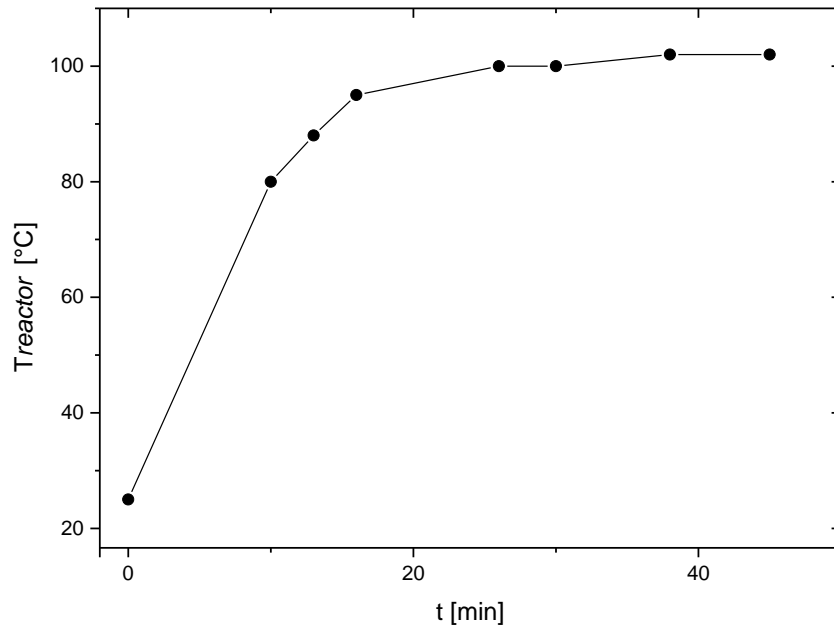
Figure 28: Heating up the reactor

3.2 STAGE HEATING

Beside the reactor, the lines, the precursor gas vessels, and the valves, also the sample stage has to be heated in order to control the substrate temperature. This is necessary since the substrate temperature has a great effect on the GPC [12]. To ensure the same conditions for all samples placed on top of the stage one has to ensure a homogeneous temperature distribution along the sample stage. To achieve this, a flexible heating disk (Dev 8) was placed at the backside of the stage (Figure 29). The heating disk is driven by a temperature controller (Dev 2). Since the stage is connected to the reactor with metal screws at three spots with no further thermal isolation the reactor temperature influences the stage temperature significantly. At the deposition conditions ($T_{reactor}$=110 °C) the temperature distribution along the stage is very homogeneous. Table 2 illustrates the temperature distribution along the sample stage depending on the reactor temperature.
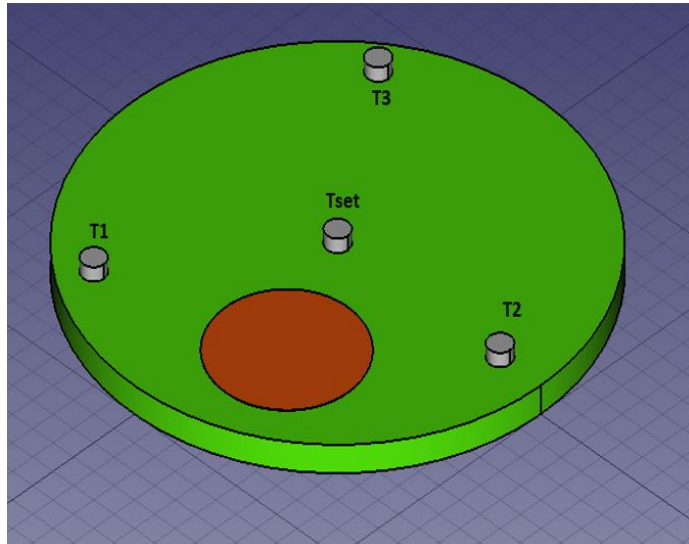
Figure 29: Stage heating

$T_{reactor}$ °C	T_{set} °C	T_1 °C	T_2 °C	T_3 °C
25	100	95	95	95
67	100	98	98	98
110	**108**	**109**	-	-

Table 2: Stage temperature distribution

3.3 Mass Flow Controller, Reactor Volume, Leak Rate

The flow of Ar going into the reactor is adjusted with the help of a mass flow controller (MFC, Dev 6) which is connected to the computer via a communication module (Dev 9). The actual flow rate is then set by an according software (App 3).
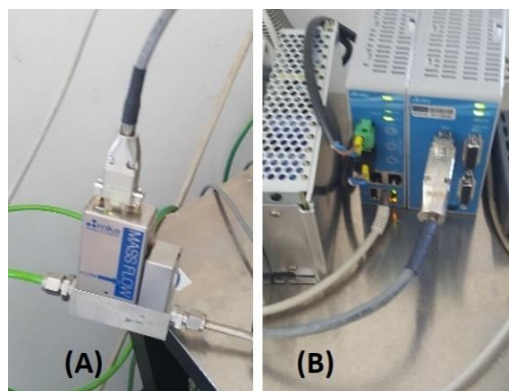
Figure 30: (A) MFC, (B) Communication module

The modulation of the purging gas flow is important for several reasons. First of all, the purging gas flow through the reactor towards the vacuum pump defines how much precursor gas is removed out of the reactor within a time increment. During the whole MLD process, there is a constant flow of Ar going through the reactor, even during the precursor exposure steps (in this case Ar is also used as a carrier gas to improve the precursor gas transport from the precursor vessels towards the reactor). Hence, water that might get into the system through little leaks is constantly carried out of the reactor, preventing the unwanted reactions described in 2.1.2. Higher flow rates of Ar, therefore, mean shorter purging times but longer precursor exposure times to reach the saturation regime of the deposition process (see 2.1.1).

Together with the pumping speed of the vacuum pump, the flow of Ar going through the reactor defines the process pressure for the deposition. Besides that, being able to define the gas flow going into the system allows the calculation of the reactor volume which for its part is necessary to estimate the leak rate of the system.

3.3.1   Reactor Volume Calculation

For a constant gas flow going into a vacuum chamber the pressure increase inside the chamber is related to its volume according to [29]:

$$\frac{\Delta p}{\Delta t} = Q/V \quad Eq\ 77$$

$$Q \ldots gas\ flowrate$$

$$V \ldots chamber\ volume$$

Since occasional changes in the system setup (device exchange etc.) always go along with a change in the reactor volume it is evidently of use to establish a quick procedure to estimate the volume. For this purpose, a program was written that simply requires the Ar flow rate going into the reactor while the vacuum pump is separated from the reactor and the according pressure increase in time that is measured with the pressure sensor (Dev 11). From this, the program calculates the reactor volume according to Eq 77 by applying a linear fitting function to the recorded pressure and taking the first derivative of this function.

For the current setup, the reactor volume is estimated to $V_{reactor} = 5\ l.$
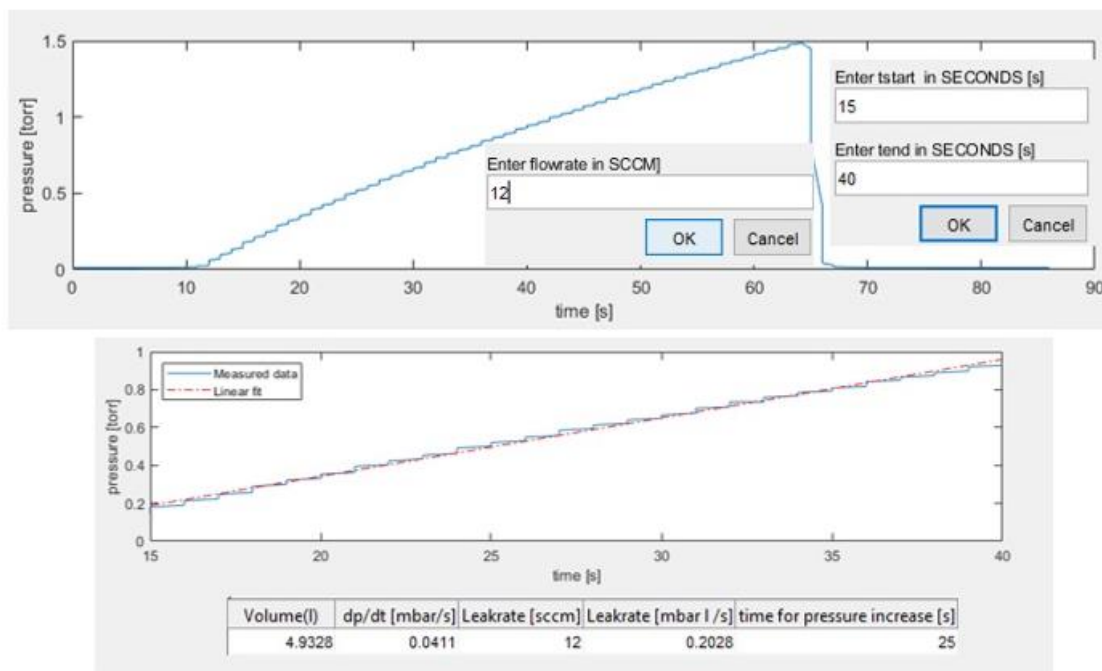
Figure 31: Reactor volume program

3.3.2 Leak Rate Estimation

Once the reactor volume is known the leak rate of the system can be measured. For this purpose, the vacuum pump is disconnected from the reactor and the resulting pressure increase is measured. In a pressure regime where the number of gas particles going out of the reactor can be neglected with respect to the number of particles going into the reactor, one can assume a linear pressure increase (this is the case for an evacuated chamber that has little particles in it compared to the atmosphere outside the chamber). Hence, the formula for the leak rate has exactly the same structure as Eq 77:

$$q_l = V * \frac{\Delta p}{\Delta t} \quad Eq\ 78$$

$$q_l \dots leak\ rate$$

$$V \dots chamber\ volume$$

A quick derivation of Eq 78 can be found at the end of this chapter.

Also for the leak rate estimation, a program was written. The program simply requires the reactor volume and the definition of the linear regime for the recorded pressure increase to calculate the leak rate according to Eq 78.

Leakrate [mbar*l/s]	Leakrate [sccm]	Volume [l]	time for pressure increase [s]
6.3290e-04	0.0375	5	135
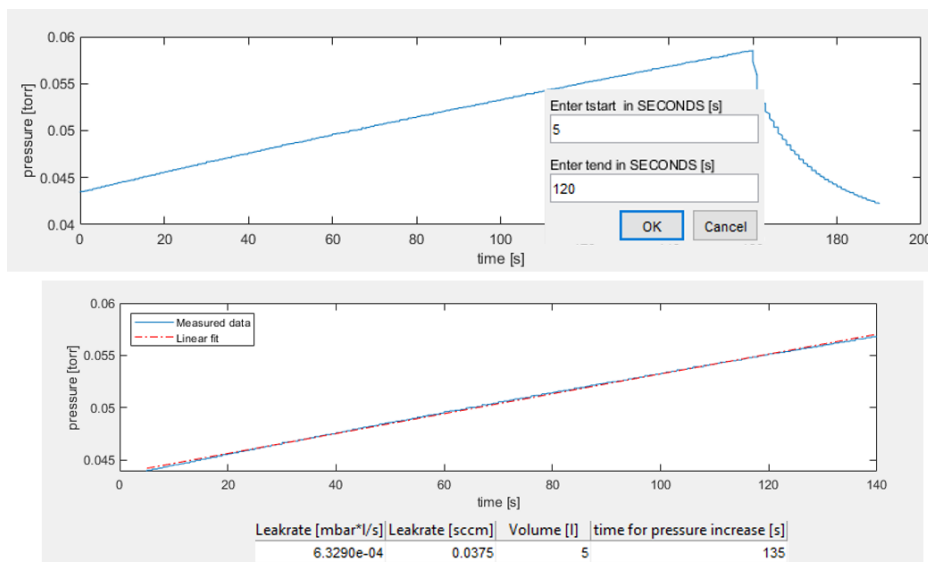
Figure 32: Leak rate program

The minimum leak rate that could be measured for the system was $q_l = 0.038\ sccm$. This ensures a proper vacuum level with a minimum amount of water diffusing into the system.

Leak rate formula derivation:

$$p * V = N * k_B * T \quad Eq\ 79$$

$$n = \frac{N}{V} \quad Eq\ 80$$

$$dp \mid_{T,V} = \left(\frac{k_B T}{V}\right) * dN \quad Eq\ 81$$

$$dN = \frac{\partial N}{\partial t} * dt \quad Eq\ 82$$

$$\frac{\partial N}{\partial t} = \frac{Q}{k_B T} \quad Eq\ 83$$

$$Q = Q_{in} + Q_{out} \quad Eq\ 84$$

$$Q_{in} \propto n_{outside} = const. \quad Eq\ 85$$

$$Q_{out} \propto n_{inside\ (t)} \quad Eq\ 86$$

For

$$n_{inside\ (t)} \ll n_{outside} \rightarrow Q_{in} \gg Q_{out} \rightarrow Q \sim Q_{in} \quad Eq\ 87$$

together with

$$Q_{in} = q_l \quad Eq\ 88$$

Eq 81 can be rewritten to

$$dp \mid_{T,V} = \left(\frac{k_B T}{V}\right) * \frac{q_l}{k_B T} * dt \quad Eq\ 89$$

what is equivalent to

$$q_l = V * \frac{\partial p}{\partial t}\Big|_{T,V} \quad Eq\ 90$$

$V \dots chamber\ volume$

$p \dots pressure\ inside\ chamber$

$Q \dots total\ gas\ flowrate\ threw\ leak$

$Q_{in} \dots gas\ flowrate\ going\ into\ the\ chamber$

$Q_{out} \dots gas\ flowrate\ going\ out\ of\ the\ chamber$

$n_{inside\ (t)} \dots particle\ density\ inside\ the\ chamber$

$n_{outside\ (t)} \dots particle\ density\ outside\ the\ chamber$

4 EXPERIMENTS & RESULTS

4.1 THE DEPOSITIONS

All films were deposited on single side polished Si-wafers with an average native oxide thickness of 1.3 nm. The wafers were cut into squared samples with a side length of 1-2 cm. For all depositions, the stage and therefore the substrate temperature was set to $T_{stage} = 109 \pm 2\,°C$. The process pressure was set to $p_{process} = 2.5 \pm 0.1 * 10^{-2}\,torr$ with a constant Ar-flowrate of $16\,sccm$ going through the system. The film thickness and refractive index were obtained with the help of spectroscopic ellipsometry. A detailed description of the experimental setup and data processing for the ellipsometry measuremets is given in 4.2.1.4.

4.1.1 Deposition Preparations, Saturation Curves

For a proper deposition process, several system settings need to be optimized. First of all, the deposition process itself must be defined. For this purpose, all system settings during the deposition are listed in Table 3. All notations for the valves in Table 3 refer to the system illustrated in Figure 25.

Process step	System setting
1. Initial valve setting	-close all valves, -open outlet and butterfly valve, -set MFC to 16 sccm
2. Constant Ar-flow threw reactor	-open valve2, -close valve3, -set MFC to 16 sccm
3.1 DEZ exposure for t_{pulse}^{DEZ} seconds	-open valve5, -wait t_{pulse}^{DEZ} s, -close valve5
3.2 DEZ purging for t_{purge}^{DEZ} seconds	- wait t_{purge}^{DEZ} s
3.3 EG exposure for t_{pulse}^{EG} seconds	-open valve4, -wait t_{pulse}^{EG} s, -close valve4
3.4 EG purging for t_{purge}^{EG} seconds	-wait t_{purge}^{EG} s
4. Finish deposition	-wait t_{end} s, -close valve2, - open valve3, set MFC to 0 sccm, -close valve3

Table 3: System settings for deposition

The number of MLD cycles and therefore the total film thickness is defined by the number of repetitions of the process steps 3.1-3.4.

Hereafter, the precursor exposure time is defined as the opening time of the valves t_{pulse} and not as the width of the pressure pulse (Figure 33) resulting from the precursor exposure since in practice it is easier to control the opening time of the valves rather than the pulse width. Anyway, the opening time of a precursor valve and the pulse width are directly related meaning longer opening times cause longer pulse width. Therefore, with the opening time of the precursor valves, one can control for how long the precursor vapors are in contact with the sample surface.
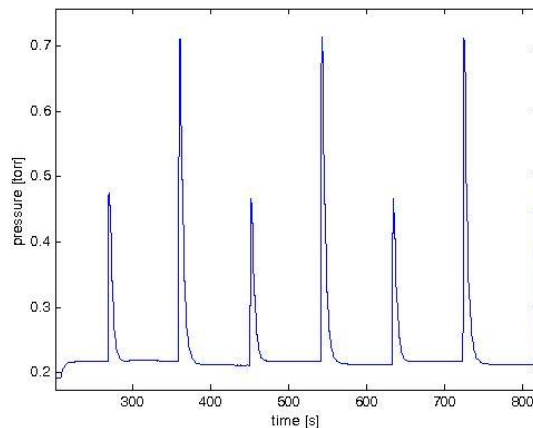
Figure 33: Pressure pulse during precursor exposure

During the whole deposition process, Ar is constantly flown through the reactor. Therefore, the Ar-flowrate affects the purging and precursor exposure time and together with the sucking power of the vacuum pump (Dev 10) defines the process pressure as described in 3.3. System pressure values corresponding to several Ar-flowrates are listed in Table 4.

Ar-flowrate [sccm]	System pressure [10^{-1} torr]
30	3.4-4.3
25	2.8-3.8
20	2.6-3.6
16	**2.4-2.6**
10	2.2-2.4

Table 4: Ar-flowrate and system pressure

For all further depositions, an Ar-flowrate of 16 sccm was chosen which turned out to provide a very stable process pressure together with an ideal compromise for minimizing both purging and precursor exposure times.

Beside the Ar-flowrate also the precursor exposure and purging times need to be optimized. On the one hand side, the purging and exposure times have to be long enough to ensure a CVD-free film growth, as described in 2.1.1. On the other hand side, they should be as short as possible to decrease the total deposition time. One can

find an ideal deposition recipe by measuring the saturation curves (see 2.1.1) of the system and choosing the shortest exposure and purging times which are still in the saturation regime of the according curve.

Before measuring the saturation curves, a relationship between the partial pressure increase due to precursor exposure and the opening times of the precursor valves must be found. A proper film growth for comparable depositions was reported at a partial pressure increase between $\Delta p_{precursor} = 10^{-2} - 10^{-1} \, torr$ ([8], [30]). The relationship between the opening times and the partial pressure increase is system dependent and therefore needs to be measured for a specific setup. For the system shown in Figure 25 one finds the following correlations listed in Table 5 & Table 6:

EG pulse time [s]	Δp [torr]
0.1	0.03
0.25	0.09
0.5	0.18
1	0.32
1.5	0.4
2	0.45

Table 5: Relationship between EG valve opening time and partial pressure increase

DEZ pulse [s]	Δp [torr]
0.02	0.04
0.05	0.09
0.1	0.18
0.15	0.22
0.2	0.25
0.25	0.28

Table 6: Relationship between DEZ valve opening times and partial pressure increase

The values obtained in Table 5 and Table 6 were obtained for a constant Ar-flow of 16 sccm.

Using the obtained precursor pulsing times as initial values made it possible to measure the saturation curves for the system. From the saturation curves, the precursor exposure and purging times for an ideal deposition recipe could be found (Eq 91). Also, the saturation curves and the ideal recipe are characteristic for the MLD system setup. They depend strongly on the geometry of the system and the flow rate of the purging gas that is constantly flown through the system. The saturation curves were taken for a constant Ar-flow of 16 sccm. The film thickness was measured with SE. The experimental setup for these measurements is specified in 4.2.1.4. The data points of the saturation curves were fitted to the according model functions derived in 2.1.1 (Eq 8 & Eq 17). The fitting parameters of the model functions gave the GPC in a saturated deposition regime. The obtained fitting parameters can be found in Table 7.

Saturation curves
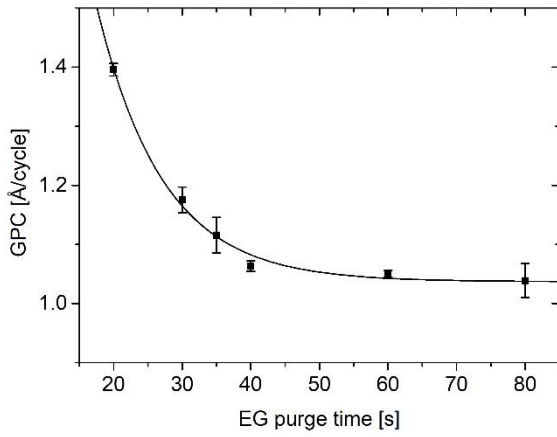
Figure 36: EG purge saturation curve
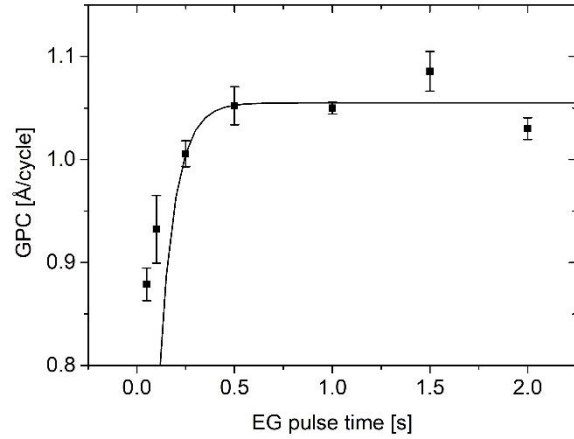
Figure 34: EG pulse saturation curve
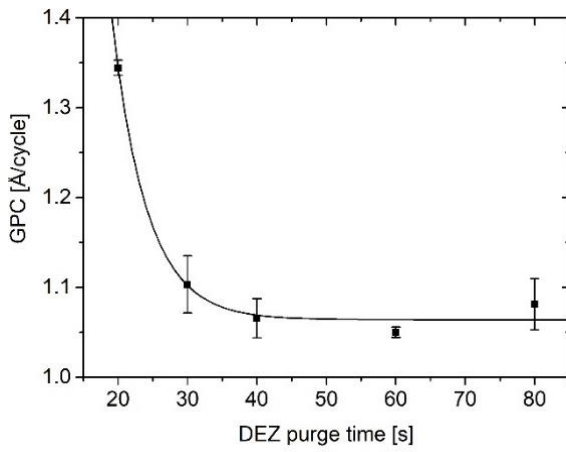
Figure 37: DEZ purge saturation curve
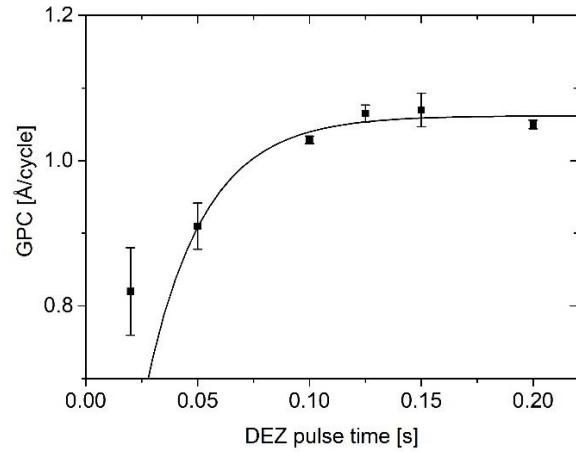
Figure 35: DEZ pulse saturation curve

Ideal deposition recipe

$$(DEZ/Ar/EG/Ar) \rightarrow (0.15/60/1/60) \text{ s} \quad Eq\ 91$$

According to the ideal deposition recipe, the total time for a complete MLD cycle is approximately 2 min.

GPC in saturation

$$GPC = 1.055 \ \frac{\text{Å}}{cycle} \quad Eq\ 92$$

Figure	Fit function	Fit parameter
Figure 35	$GPC_{(t)} = G * (1 - ex\,p(-p_0 * t))$	$G = 1.062$ Å, $p_0 = 38.68\ s^{-1}$
Figure 34	$GPC_{(t)} = G * (1 - ex\,p(-p_0 * t))$	$G = 1.055$ Å, $p_0 = 12.24\ s^{-1}$
Figure 36	$GPC_{(t)} = G + GPC_{max}^{CVD} * exp(-C * t)$	$G = 1.037$ Å, $GPC_{max}^{CVD} = 2.849$ Å, $C = 0.1034\ s^{-1}$
Figure 37	$GPC_{(t)} = G + GPC_{max}^{CVD} * exp(-C * t)$	$G = 1.064$ Å, $GPC_{max}^{CVD} = 15.25$ Å, $C = 0.1998\ s^{-1}$

Table 7: Saturation curve fitting parameters

Averaging the fitting parameter G for the four saturation curves (see Eq 23) gives the value for the GPC in saturation (Eq 92)

4.1.2   Depositions in the Saturation Regime

With the ideal deposition recipe, several samples were produced for which the number of MLD cycles was increased from 30 to 500.
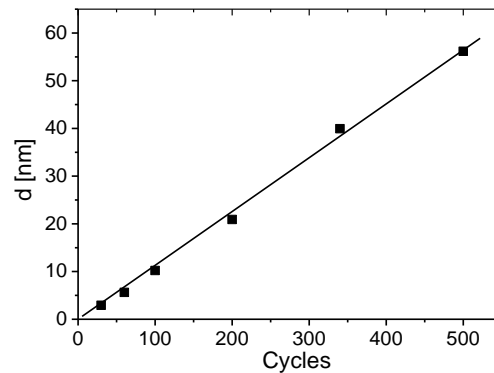
Figure 38: Film thickness vs cycle number
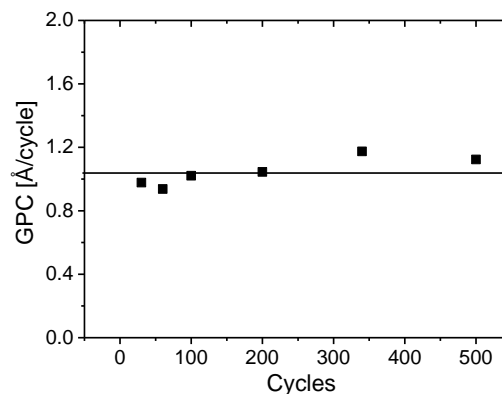
Figure 39: GPC vs cycle number

Figure 38 clearly shows a linear correlation between the total film thickness and the number of MLD cycles. This means that the GPC varies only within a little error, even when the number of cycles changes within one order of magnitude. A constant GPC is a strong indicator for a deposition process in saturation that avoids any kind of CVD like growth. Therefore, Figure 39 underlines the MLD-like character of the deposition process. It also shows that there is only little formation of double bonds as depicted in Figure 6. An increased formation of double bonds would lead to a decreased GPC for a larger number of cycles, which is not the case.

Samples up to 50 nm film thickness were produced. The recorded data shows no tendency of a decreasing GPC with higher cycle numbers. It is therefore likely that samples of even greater thickness can be produced without any problems.

4.2 THIN FILM CHARACTERISATION

4.2.1 Heating Experiments

With Zincone films up to 50 nm thickness heating experiments could be carried out in order to create the desired porous ZnO structure. For this purpose, samples were heated to both 400°C and 600°C at a very low heating rate of 200°C/h. A low heating rate was chosen to give the remaining zinc and oxygen enough time for structural reorganization after the removal of the organic linker.

Several in- and ex-situ techniques were used to characterize the film transformation caused by heating. FTIR was used to determine the chemical composition of the film before and after heating. In situ XRD measurements were carried out in order to specify the crystallization behavior of the film. Measuring the film with XRR during the heating process gave several film parameters such as the electron and mass density as well as the film roughness and thickness as a function of temperature. Spectroscopic ellipsometry allowed to measure the film thickness and refractive index as a continuous function of increasing temperature and was therefore ideal to give a detailed insight into the structural change during the heating experiment.

4.2.1.1 Ex Situ FTIR: Before and After Heating

With the help of FTIR, it was possible to check if the organic part in the film can be removed by heating. For this purpose, FTIR spectra of several samples were taken before and after the heating process with the help of a Michelson interferometer (Dev 12). Each spectrum results from averaging 1000 measurements in order to minimize the signal-to-noise ratio. The substrate Si wafers were measured before and after the deposition. The transmission spectrum of the deposited film was then obtained from the ratio between the spectra measured before and after the deposition. Therefore, the spectrum taken before the deposition serves as a reference spectrum. Dividing the two spectra provides a smaller noise-related relative error than the subtraction of the two. Furthermore, each spectrum shown below was baseline corrected to illustrate the absorption peaks as good as in any way possible. In the following, only the change in the chemical composition caused by heating was elaborated. Changes in the film caused by degradation processes related to reactions with water from ambient air are further investigated in 4.2.3.
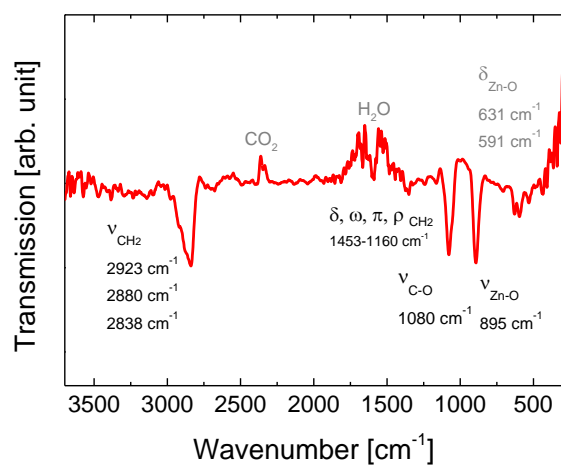
Figure 40: FTIR: Zincone film after deposition (not degraded)
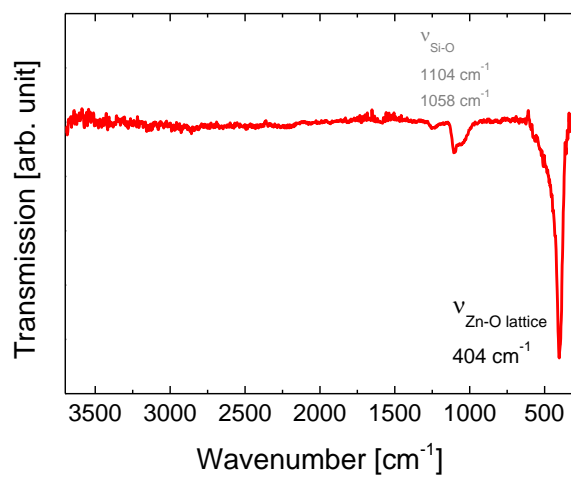
Figure 41: FTIR: film after heating to 600 °C in air
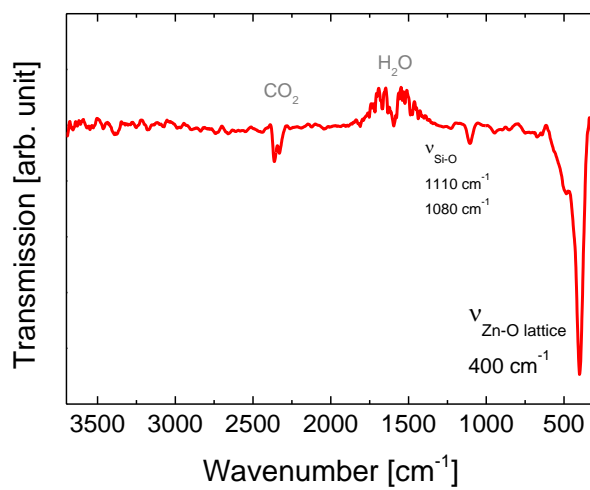
Figure 42: FTIR: film after heating to 400 °C in air
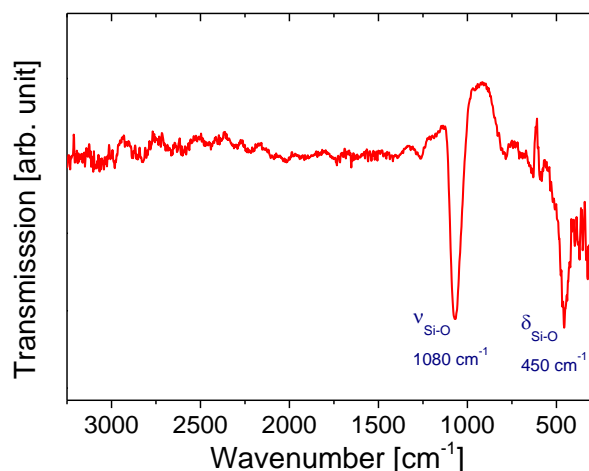
Figure 43: FTIR: Si wafer change due to 600 °C heating in air

Figure 40 shows the transmission spectrum of a film right after the deposition. The sample was exposed to ambient air less than ten minutes and therefore barely had the chance to react with water from ambient air. The spectrum shows all expected characteristics of a metal organic Zincone film. Similar spectra were published in several papers such as [8] & [10]. For the assignment of the peaks [8] was used as a reference for the spectrum of a typical Zincone film. The peaks at 2923, 2880 and 2838 cm^{-1} are assigned to $C-H$ stretching modes in a CH_2 unit. Peaks between 1453 and 1160 cm^{-1} can be ascribed to bending, rocking and wagging modes in a CH_2 unit. The peak around 1080 cm^{-1} is related to a $C-O$ mode. All these peaks can be related to the organic linker in the Zincone films.

The CO_2 peaks around 2350 cm^{-1} can be explained by a higher CO_2 content in the atmosphere while measuring the reference spectrum. The broad characteristic H_2O peaks are due to the fact that the reference sample was exposed to ambient air much longer than the sample after the deposition. Hence, more water could adsorb inside the Si wafer which leads to a higher content of water in the reference than in the sample measured right after the deposition. The H_2O feature could also be explained by a higher content of water in the ambient during the reference measurement. In any case, both the H_2O and the CO_2 peaks are not related to the thin film itself but result from different environmental conditions.

The peak at 895 cm^{-1} is assigned to a $Zn-O$ stretching mode while the peaks at 631 and 591 cm^{-1} are related to bending modes of $Zn-O$. The measured spectrum is consistent with the expected Zincone hybrid structure assumed in chapter 2.1.1.

Figure 41 and Figure 42 show the FTIR spectra of samples that were heated to both 600 °C and 400 °C respectively in ambient air. In both cases, all the typical carbon-related peaks of Zincone disappear except for the CO_2 and H_2O peaks which are not related to the film. However, one can clearly see a peak at roughly 1100 cm^{-1}. For both

the 600 °C and the 400 °C spectra this peak consists of a big peak at 1104 and 1110 cm^{-1} respectively, followed by a broader shoulder peak at lower wavenumbers. This is the typical stretching vibration peak of $Si - O$ in SiO_2. For pristine SiO_2 this peak consists of a sharp peak at 1080 cm^{-1} with a smaller shoulder peak at higher wavenumbers. For an increasing impurity content, the peak at higher wavenumbers increases and can even surpass the original shoulder peak. It is possible that carbon that was initially bond inside the film pollutes the SiO_2 that forms during the heating process.

To prove that this peak belongs to SiO_2 formed during the heating process and is therefore not related to the film itself a heating experiment for a pristine Si wafer was carried out. FTIR spectra were measured for a pristine Si wafer at room temperature and after heating the Si wafer to 600 °C. Both spectra were divided by each other in order to characterize the modification of Si caused by heating (Figure 43). Figure 43 shows two peaks which are both related to a $Si - O$ vibrations in SiO_2. Yet, only the peak at 1080 cm^{-1} shows up in the spectra of the heated Zincone sample (Figure 41 & Figure 42). The smaller peak in the pristine Si-wafer spectrum at 450 cm^{-1} is not visible in the heated Zincone film spectra because it is superimposed by another much bigger peak arising at 400 cm^{-1}.

The peak at 400 cm^{-1} in Figure 42 & Figure 41 is assigned to a $Zn - O$ stretching vibration of ZnO arranged on a regular lattice. Hence, the only peak that can be assigned to the film in the two heated Zincone spectra corresponds to crystalline ZnO.

Therefore, already the FTIR data show that heating the Zincone film to both 600 °C and 400 °C results in the formation of crystalline ZnO and removal of all the organic content inside the film.

4.2.1.2 In Situ XRD

In order to further investigate the crystallization process during the temperature increase, XRD measurements were taken at several temperatures during the heating experiments. The measurements were done with an X-ray diffractometer (Dev 13) that is equipped with a Cu_{K_α} X-ray source with the according wavelength of $\lambda_{Cu_{K_\alpha}} =$ 1.542 Å. For the temperature increase, a special heating stage (Dev 14) was used. In order to tell the diffraction peaks of the crystalline film apart from possible peaks referring to diffractions at crystal lattice of either the Si substrate or the sample stage, reference measurements were taken for both a pristine Si wafer with a 1.3 nm native oxide layer and the sample stage only. The reference measurements are illustrated below.
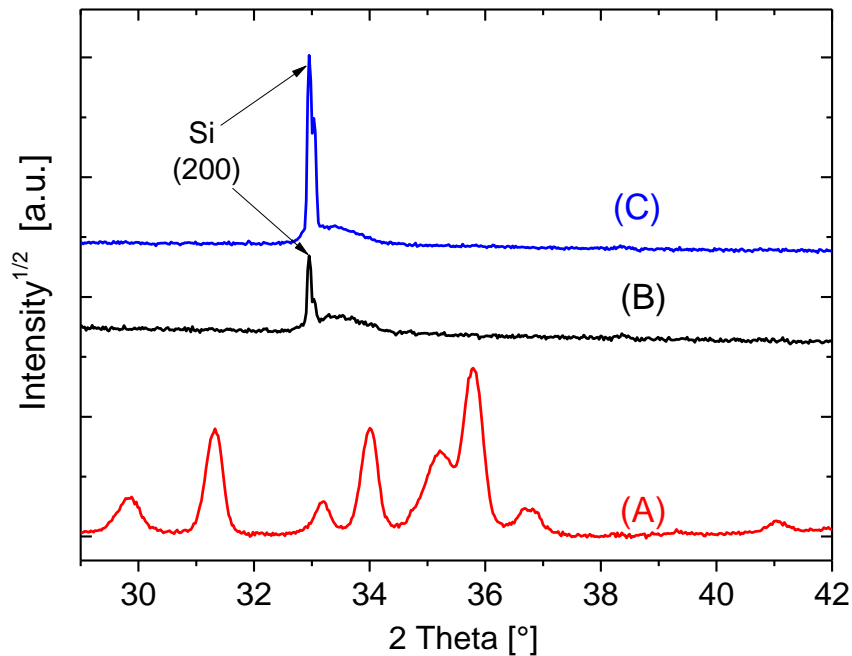
Figure 44: XRD scan for A) Sample stage, B) Si wafer with 1.3 nm native oxide, C) Zincone film before heating (non-crystalline film)

Figure 44 shows that the big Bragg peak at 32.94 ° together with its broader shoulder peak at higher diffraction angles refers to the Si substrate. This peak is also visible in the XRD spectrum of the Zincone film. Bragg peaks referring to the sample stage do not appear in the spectrum of the Zincone film.

In the following, all the peaks in the XRD spectra of the crystallizing film (Figure 45 & Figure 46) which are not explicitly labeled refer to diffractions at the substrate.

In order to find the temperature for which the initial Zincone film starts to form crystalline ZnO quick XRD scans were taken for every 20 °C of temperature increase between 220 °C and 400 °C (Figure 45). At 340 °C the first characteristic Bragg peaks of crystalline ZnO appear at scattering angles of 31.7 ° and 36.1 ° corresponding to the (100) and (101) net plane of ZnO, respectively.

Already between 340 °C and 400 °C the Bragg peaks referring to ZnO increase in height meaning that the ZnO crystallite size is growing rapidly even in this small temperature regime (see Eq 22).
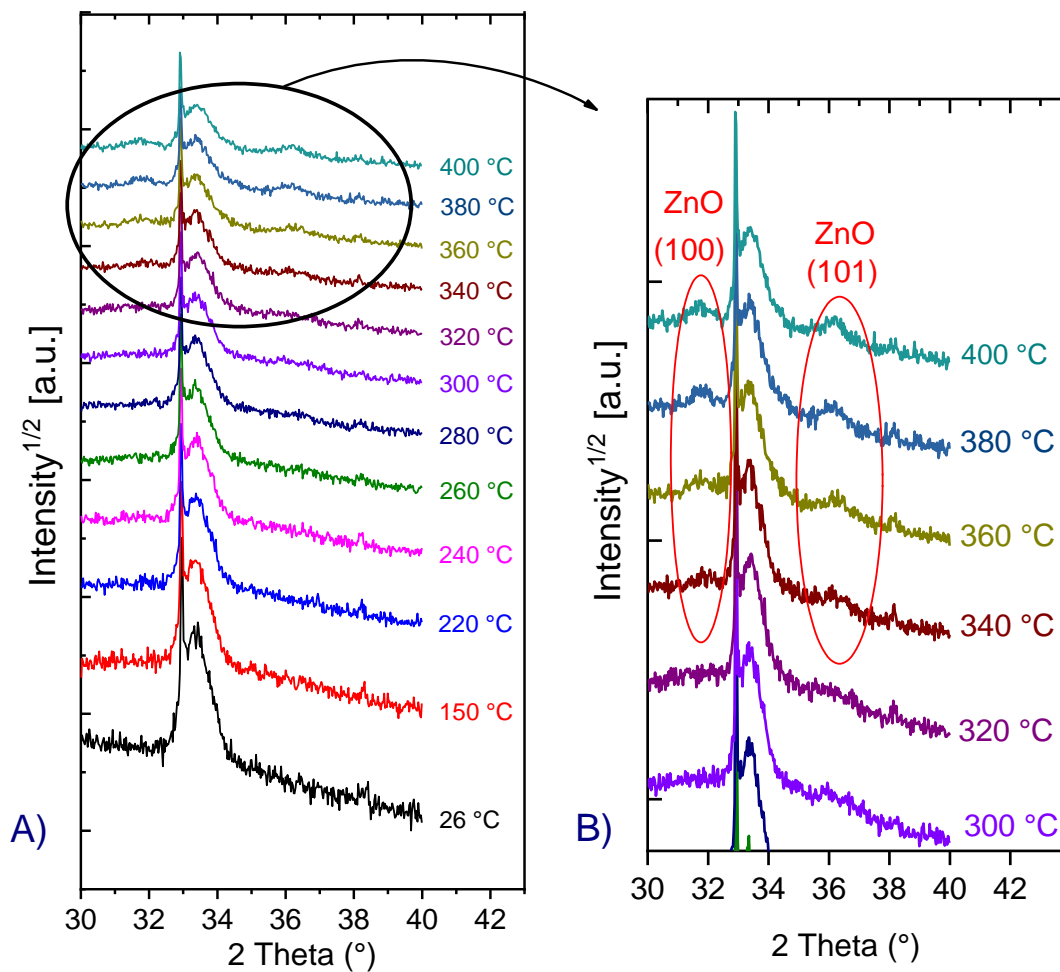
Figure 45: A) XRD quick scan between 220 °C and 400 °C, B) ZnO Bragg peaks starting at 340 °C

To provide high-resolution scans in the temperature range where the crystallization takes place, XRD measurements with long acquisition times were taken in the temperature range between 360 °C and 600 °C, and after the film had been cooled back down to room temperature (Figure 46).
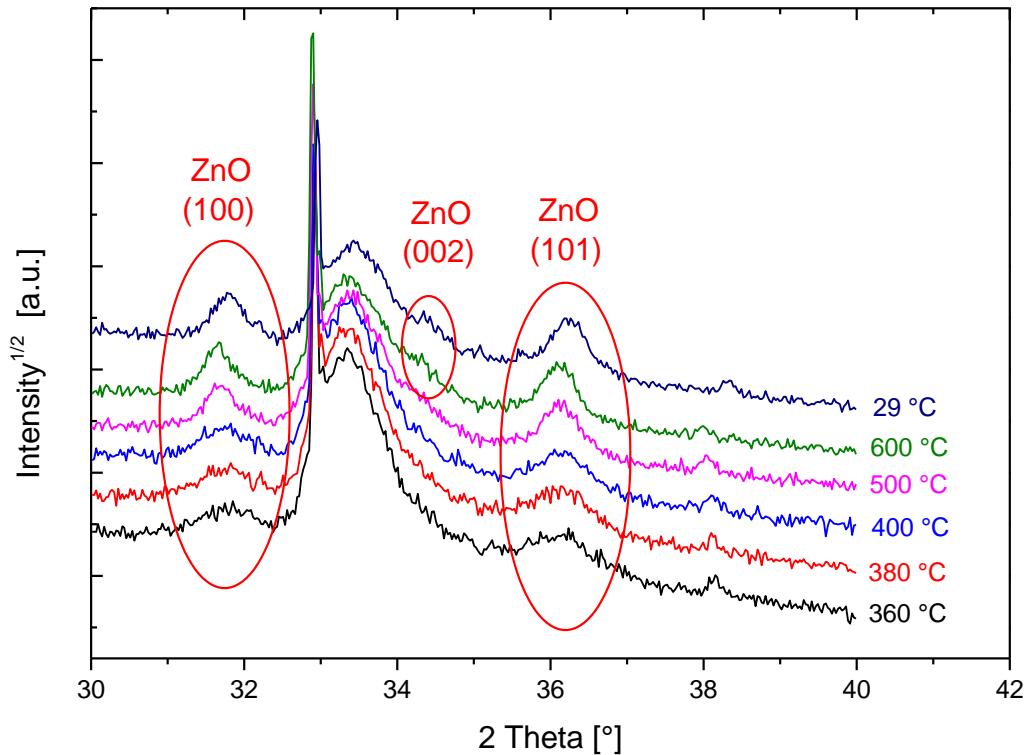
Figure 46: XRD long scan between 360 °C and 600 °C

Between 360 °C and 500 °C, the ZnO (100) and (101) diffraction peaks are increasing in height while simultaneously decreasing in width. This shows that the ZnO crystallites grow mainly in this temperature region. From the shape of the according Bragg peaks the crystallite size was estimated according to Eq 22, with the aim of representing the crystallite length perpendicular to the sample surface as a function of temperature (Figure 47 & Figure 48). For temperatures even higher than 500 °C a small peak at 34.3 ° arises in Figure 46 which is ascribed to diffraction at the ZnO (002) net planes.

Summarising, three different ZnO Bragg peaks can be observed during the temperature increase corresponding to three different crystallite orientations with respect to the sample surface. Therefore, polycrystalline ZnO is grown within the heating process.

Furthermore, comparing the XRD scan taken at 600 °C to the one of the sample that was cooled back down to room temperature after heating one can clearly see that the two measurements are basically identical except for the fact that the Bragg peaks shift to higher angles which can be related to a decrease in the interplanar distance of the ZnO crystal lattice caused by the plane relaxation after thermal expansion. This means that the polycrystalline structure of the film that was created within the heating process remains stable when cooling the film back down to room temperature.
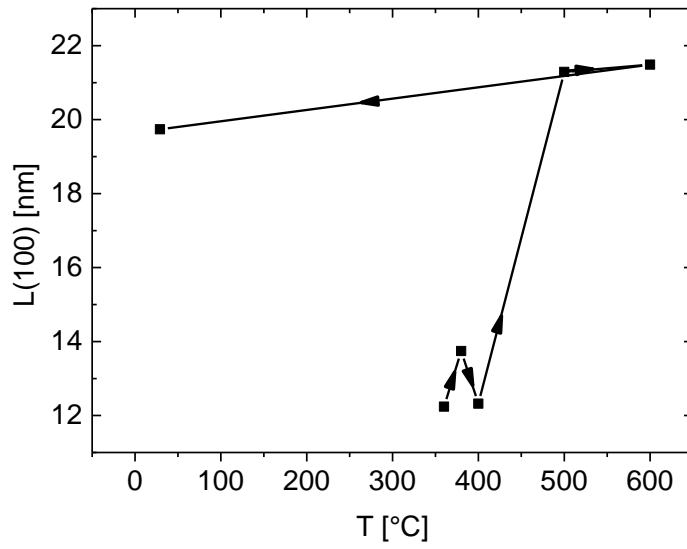
Figure 47: (100) crystallite length perpendicular to the sample surface
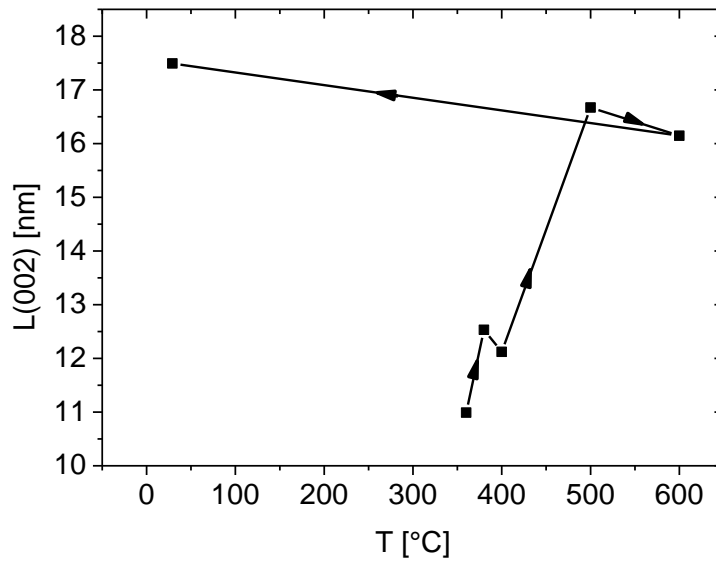
Figure 48: (101) crystallite length perpendicular to the sample surface

Figure 47 & Figure 48 suggest a crystallite size roughly between 17 nm and 21 nm for the crystalline ZnO film that was cooled back down to room temperature after heating to 600 °C.

4.2.1.3 In Situ XRR

Measuring the Zincone films with XRR during the heating experiments allowed to illustrate several parameters of the film as a function of temperature. For the XRR scans the same device setup as in 4.2.1.2 was used. The different XRR scans, taken at the same temperatures as the XRD scans in 4.2.1.2, are illustrated below:
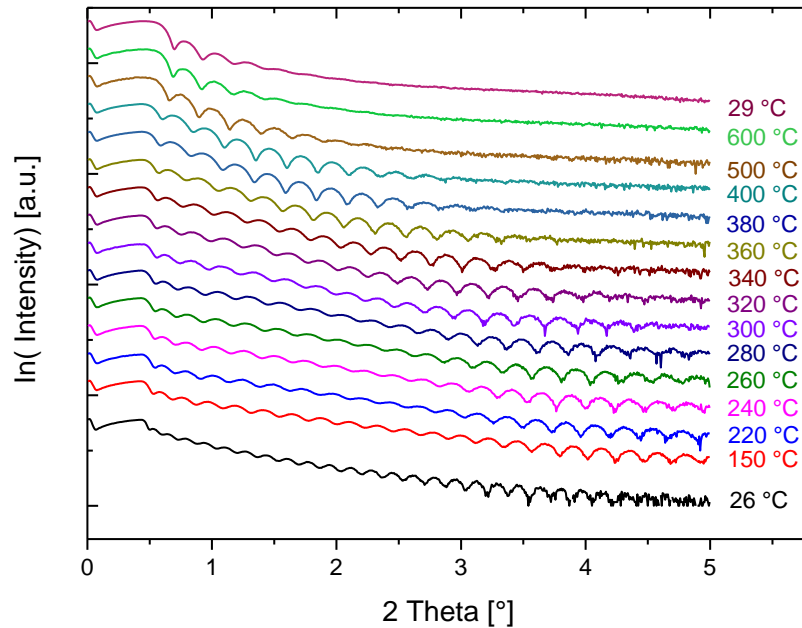
Figure 49: XRR spectra of the heated Zincone film

First of all, for every measured XRR spectrum the critical angle was defined as the incidence angle where the intensity of the reflected X-ray beam has dropped to half its initial value (see Figure 13). From the critical angle, the electron density of the film was calculated according to Eq 26. Thus, the electron density of the film could be illustrated as a function of temperature (Figure 50).

According to Figure 50, the electron density increases with increasing temperature. The slope of the electron density with respect to temperature changes around 340 °C. This change in the slope is related to a phase transition of the film namely the crystallization of ZnO. This is totally in agreement with the XRD measurements that show the beginning of the crystallization at exactly the same temperature. Hence, in order to interpret the rise in the electron density with increasing temperature one has to differentiate between temperature regions below and above 340 °C.
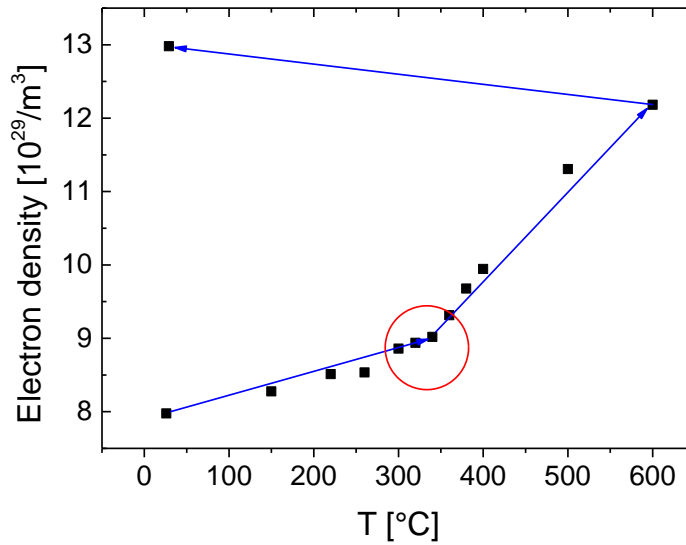
Figure 50: Electron density vs. temperature

Below 340 °C, there are several reasons that can cause an increase in the electron density. First of all, the FTIR data shows that already below 400 °C all the "light" organic content is removed and only the "heavier" zinc and oxygen atoms remain inside the film. This is directly related to an increasing mass- and electron density of the film.

Furthermore, although there are no signs for crystallization the film can still rearrange its internal structure and densifies below 340 °C. Beside others, the reorientation process of the non-crystalline ZnO can cause the reduction of vacancies which are created during the removal of the organic part of the film. Since reorientation is typically favored by higher temperatures the mass- and electron density increase with increasing temperature.

For temperatures higher than 340 °C one can mainly assign the mass- and electron density increase to the crystallization process. A higher content of crystalline ZnO over non-crystalline ZnO obviously increases the density of the film. Besides, the XRD data (Figure 47 & Figure 48) show a growing crystallite size mainly between 340 °C and 500 °C. Growing crystallites cause a decrease in cavities between crystal grains also resulting in an increased mass- and electron density of the film.

When the film is cooled down from 600 °C back to room temperature the electron density increases. This is related only to thermal expansion since the XRD data suggest no change in the crystal structure and composition of the film within the cooling process. Model calculations on the temperature dependency of the related mass density of zinc oxide show that changes in the density caused by temperature decrease are on the same order of magnitude as the measured values. Such calculations can be found at the end of this chapter.

Assuming a proper model for the chemical composition of the thin film and the substrate material, the measured XRR spectra could be fitted with the help of a convenient software (App 1). The fitting program requires several input parameters such as the chemical composition of the substrate as well as an assumption on the number of layers on top of the substrate together with the specification of their order and composition. Both the substrate and each defined layer generate three different fitting parameters namely the thickness, the surface roughness and the mass density of each ply. For each variable one can choose to set it to a constant value or to use it as a fitting parameter in the fit. Obviously, with the number of fitting parameters the degrees of freedom for the fitting function increases, allowing to easily minimizing the least square error between the measured data and the fitting function. However, the fit with the least square error does not automatically lead to the best estimation for the real physical values of the parameters. Quite the contrary, values which provide a minimal least square error may be completely unphysical. Therefore, meticulous attention needs to be paid in order to use only physically justifiable layers and fitting parameter values.

For each fit, a model was assumed that includes Si as the substrate material together with an according native oxide layer of SiO_2 on top. The assumption for the chemical composition of the on deposited film required further considerations. While the electron density of the film has a one-to-one correspondence to the critical angle in each XRR spectrum (see Eq 26), the mass density depends on the choice of the chemical composition of the layer. The reason for this is that the chemical composition relates the electron density of a material to its mass density as described in 2.2.3. Hence, the right

Figure 51: Layer modes for XRR fit

choice for the chemical composition of the film is crucial for the validity of the mass density obtained from the XRR fit. Unfortunately, the chemical composition of the film changes during the temperature increase since carbon and hydrogen is removed out of the system. One is therefore confronted with a variable chemical composition with a not fully known temperature dependency. Luckily, there are two temperature regimes for which the chemical composition is well known, namely before and after the heating experiment. According to the Zincone model described in 2.1.2 the chemical composition of the thin film before the heating process was chosen as $ZnO_2C_2H_4$. After the heating experiment, based on the FTIR data, a pristine ZnO model was chosen to properly describe the film. For the temperature regime between room temperature and 600 °C, one of the two models had to be chosen, despite the fact that none of them would fully correctly describe the film. The first fit was done at room temperature with a Zincone film model of the composition $ZnO_2C_2H_4$. Since this first fit provided important initial parameters for the further fits at higher temperatures the same Zincone film model was used for the fits at higher temperatures, keeping in mind that the obtained values for the mass density at higher values would not match the real physical value (Figure 52).

Calculations that can be found at the end of this chapter show that during the temperature increase the mass density of the Si substrate and the SiO₂ native oxide change only within less than 1 %. Therefore, these values were obtained from the first fit that was done for the spectrum taken at room temperature and were then set constant in the further fits of the higher temperature spectra. Furthermore, also the thickness of the native oxide layer was obtained from the first fit and was then set constant. This is justifiable due to the low thermal expansion coefficient of SiO₂ compared to the one of ZnO. The thickness of the substrate is set to an infinite length, hence is never used as a fitting parameter. Therefore, for the higher temperature XRR spectra, only the film thickness, the mass density of the film and the roughness at the different layer interfaces were used as variable fitting parameters. This offers the advantage that within the fitting procedure, changes in the measured XRR spectra are being related only to those parameters which physically change during the temperature increase.
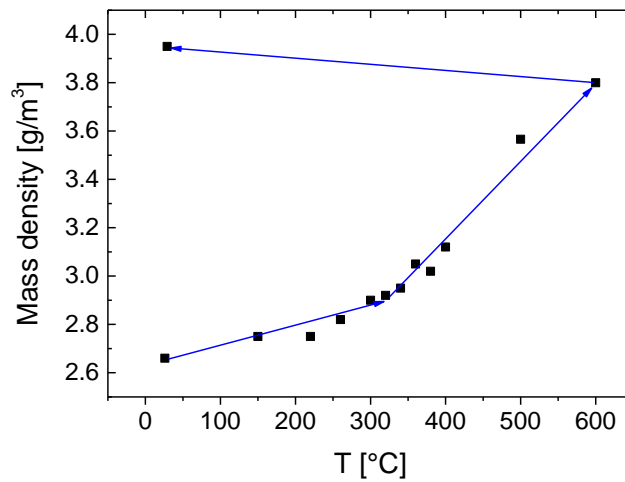
Figure 52: Zincone model mass density vs. temperature from XRR fit
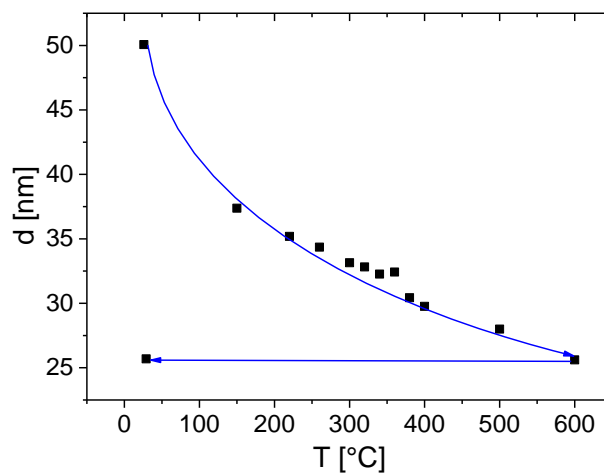
Figure 53: Film thickness vs. temperature from XRR fit
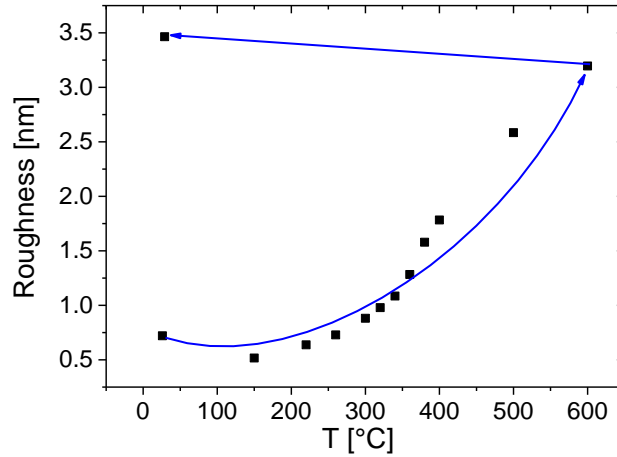
Figure 54: Film roughness vs. temperature from XRR fit

Even though the values of the mass density depicted in Figure 52 do not fully coincide with the real physical values due to the variable composition of the film during heating, the general trend of the temperature dependency is well illustrated in Figure 52. Yet, when it comes to exact physical values, the electron density (Figure 50) is a much more reliable quantity to describe temperature dependency since it is not dependent on the chemical composition of a hypothetical film model. Besides that, the electron density is also representative for the mass density, meaning that the temperature dependency of the mass density in Figure 52 is equivalent to the electron density in Figure 50. Therefore, the different characteristics in the temperature dependency of the mass density can be assigned to the same origins as for the electron density.

Using a simple ZnO model for the chemical composition of the film that was cooled back down to room temperature after the heating process led to the following value for the mass density:

$$\rho^{Film}_{(cooled\ 29\ °C)} = 4.54\ g/cm^3 \qquad Eq\ 93$$

Comparing this value to the well-known mass density of bulk ZnO shows a film mass density that is decreased by 20 % compared to the bulk ZnO.

This together with the fact that the organic content of the film is negligible after the heating process suggests a total film porosity of 20 %.

$$\frac{\rho^{Film}_{(cooled\ 29°C)}}{\rho^{Bulk\ ZnO}} \sim 0.8\ \rightarrow 20\ \%\ Vacancies \qquad Eq\ 94$$

At this point it is crucial to distinguish between the total porosity which includes also fully encapsulated voids inside the film (closed porosity) and the open porosity of the

69

film which is accessible from the film surface. Unlike total porosity, the open porosity can only be measured with ellipsometric porosimetry (see 4.2.2).

The obtained values for the thickness and roughness during the heating experiment are largely independent of the choice of the chemical composition of the film and are therefore trustful (Figure 53 & Figure 54).

Figure 53 shows a decreasing film thickness with increasing temperature. This is in line with a film densification due to both the removal of the organic content of the hybrid film and structural reorganization as well as crystallization of the remaining ZnO inside the film. Especially, between room temperature and 150 °C, the thickness strongly decreases. This is mostly related to a structural collapse of the film due to the carbon removal. A much more detailed description of the structural changes in this temperature region can be found in 4.2.1.4 where the thickness was measured as a continuous function of temperature with the help of spectroscopic ellipsometry. Between 150 °C and 600 °C the film thickness is further decreasing which is related to reorientation process of the remaining ZnO below 340 °C and to crystallite grain growth between 340 °C and 600 °C. The minimal film thickness decrease during the cooling process is assigned to thermal expansion only (see Eq 106). This underlines the stable structure of the film after the cooling process.

According to Figure 54, the roughness of the film increases with temperature mainly between 300 °C and 600 °C. This can be ascribed to the formation of cavities at the film surface as well as to the crystallization process that forms growing crystallite grains which roughen the surface morphology of the film.

Mass density and film thickness change due to thermal expansion

The mass density is defined as:

$$\rho_{(T)} = \frac{M}{V_{(T)}} = \frac{M}{L_{x(T)} * L_{y(T)} * L_{z(T)}} \quad Eq\ 95$$

Which gives the following temperature dependency:

$$\frac{d\rho}{dT} = \sum_{i=1}^{3} \frac{\partial \rho}{\partial L_i} * \frac{\partial L_i}{\partial T} \quad Eq\ 96$$

$$\frac{\partial \rho}{\partial L_i} = -\frac{\rho}{L_i} \quad Eq\ 97$$

For an isotropic material:

$$\frac{\partial L_i}{\partial T} = L_i * \alpha \qquad Eq\ 98$$

Combining Eq 96, Eq 97 & Eq 98 gives:

$$\frac{d\rho}{dT} = \sum_{i=1}^{3} -\frac{\rho}{L_i} * L_i * \alpha = -3 * \rho * \alpha \qquad Eq\ 99$$

For a first-order Taylor expansion of the mass density with respect to temperature one finds:

$$\rho_{(T)} - \rho_{(T_0)} = \frac{\partial \rho}{\partial T}\Big|_{T_0} * (T - T_0) \qquad Eq\ 100$$

Eq 99 & Eq 100 give the following expression for the temperature dependency of the mass density:

$$\rho_{(T)} = \rho_{(T_0)} * (1 - 3 * \alpha * (T - T_0)) \qquad Eq\ 101$$

Last but not least, for first-order thermal expansion one can write:

$$L_{(T)} - L_{(T_0)} = \frac{\partial L}{\partial T}\Big|_{T_0} * (T - T_0) \qquad Eq\ 102$$

Together with Eq 98, this gives:

$$L_{(T)} = L_{(T_0)} * (1 + \alpha * (T - T_0)) \qquad Eq\ 103$$

$$\rho \dots mass\ density$$

$$M \dots mass$$

$$V \dots volume$$

$$L_i \dots length\ in\ direction\ i$$

$$\alpha \dots thermal\ expansion\ coefficient$$

With the help of Eq 101, it is possible to estimate changes in the mass density caused by thermal expansion. In the following this is calculated for the Si substrate and the SiO$_2$ native oxide layer as well as for the already crystallized ZnO film to estimate the thermal expansion effect during the heating and cooling process, respectively.

Si substrate

$$\alpha_{Si} = 2.6 * 10^{-6} \ °C^{-1} \rightarrow \frac{\rho_{Si\,(600\,°C)}}{\rho_{Si\,(26\,°C)}} = 0.996 \rightarrow \Delta\rho_{Si} = 0.4\% \qquad Eq\ 104$$

SiO₂ native oxide

$$\alpha_{SiO_2} = 0.75 * 10^{-6} \ °C^{-1} \rightarrow \frac{\rho_{SiO_2\,(600\,°C)}}{\rho_{SiO_2\,(26\,°C)}} = 0.999 \rightarrow \Delta\rho_{SiO_2} = 0.1\% \qquad Eq\ 105$$

Eq 104 & Eq 105 show that the change in the mass density of the substrate and native oxide caused by thermal expansion during the heating process is negligible. Therefore, it is reasonable to set the mass density of the substrate and native oxide to a constant value during the fit of the XRR data.

Crystallized ZnO film

$$\alpha_{ZnO} = 1.57 * 10^{-5} \ °C^{-1} \rightarrow \frac{\rho_{ZnO\,(600\,°C)}}{\rho_{ZnO\,(26\,°C)}} = 0.973 \rightarrow \Delta\rho_{ZnO} = 2.7\ \% \qquad Eq\ 106$$

$$\frac{L_{ZnO\,(600\,°C)}}{L_{ZnO\,(25\,°C)}} = 1.009 \rightarrow \Delta L_{ZnO} = 0.9\ \%$$

The calculated change in the crystalline ZnO mass density of 2.7 % is very close to the observed change of 3.8 % during the cooling process (Figure 52). For the thickness decrease during the cooling process, a value of 0.9 % was calculated considering only thermal expansion. This is comparable to the measured thickness decrease of 0.3 % in Figure 53. Hence, changes in the mass density (Figure 52) and the closely related electron density (Figure 50) of the film as well as in the film thickness during the cooling process can definitely be assigned to thermal expansion.

4.2.1.4 In Situ Ellipsometry

With the help of spectroscopic ellipsometry, it was possible to measure the refractive index and the thickness of the film as a continuous function of temperature. This allowed a very precise specification of the temperature regimes of the different transformation mechanism inside the film. For this purpose, an ellipsometer (Dev 15) was used in combination with a special heating stage (Dev 16) which is operated by the according system controller (Dev 17) and can be cooled with the help of a liquid nitrogen cooling pump (Dev 18).

For processing the measured ellipsometry data, a fitting software *CompleteEASE* (App 2) was used along with a proper sample model, including Si as the substrate material together with the according SiO_2 native oxide layer and the on-deposited film. For the substrate and the native oxide layer, precast models were used that can be found in the library of the fitting software (NTVE_JAW and Si_Temp_JAW respectively). The precast substrate model (Si_Temp_JAW) offers the advantage of automatically adjusting the substrate material properties to the current temperature. For the deposited film, a Cauchy model (Eq 31) was used to fit the refractive index of the film from the measured data where A & B were used as fitting parameters and C was set to 0. Also, the film thickness is used as a fitting parameter. The absorption coefficient of the film (Eq 32) was not used as a fitting parameter but set to 0 because of the transparency of the films in the investigated spectral regime between 450 nm and 900 nm. Using 450 nm as the lower wavelength limit ensures the transparency of the film even after the crystallization process that involves the formation of the typical ZnO band gap around 375 nm. Following these guidelines allows measuring the film's thickness and refractive index for a variable temperature.

Furthermore, the total percentage of vacancies inside the film was estimated with the help of an effective medium approximation (EMA) as described in 2.2.5.1. The *CompleteEASE* software offers several EMA fitting models. A Maxwell-Garnett approach was chosen for the EMA. The Maxwell-Garnett approach assumes the film as a two-component material that consists of spherical voids filled with air embedded in a host material. The host material itself was described by a Cauchy model. Using the fraction of voids inside the film as a fitting parameter together with the typical Cauchy fitting parameters for the host material allows one to specify the fraction of total porosity within the film.

In the following the refractive index at a wavelength of 632.8 nm and the thickness of a film that was heated to 600 °C in an ambient air atmosphere are illustrated as functions of temperature.
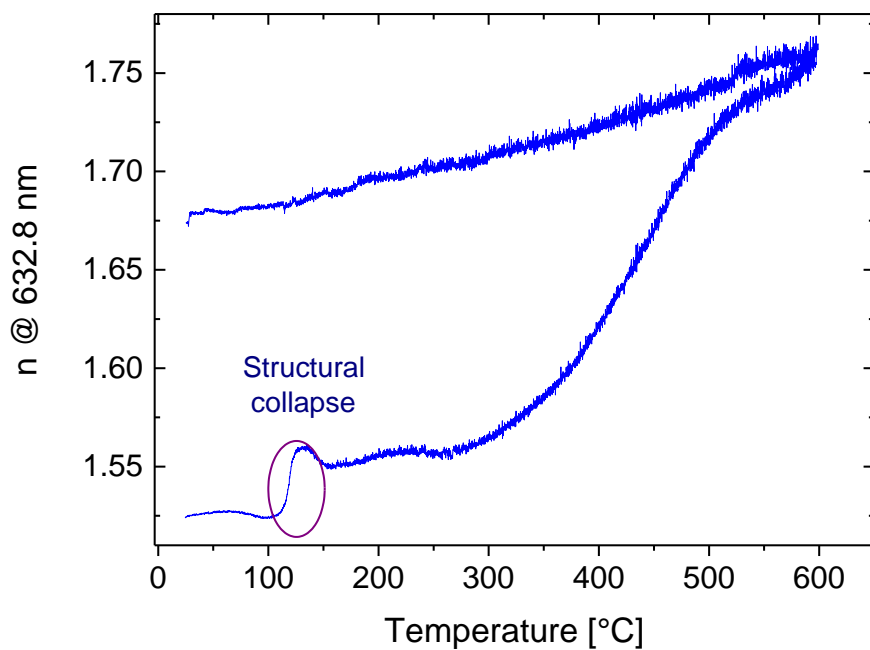
Figure 55: Refractive index at 632.8 nm vs. temperature from SE fit
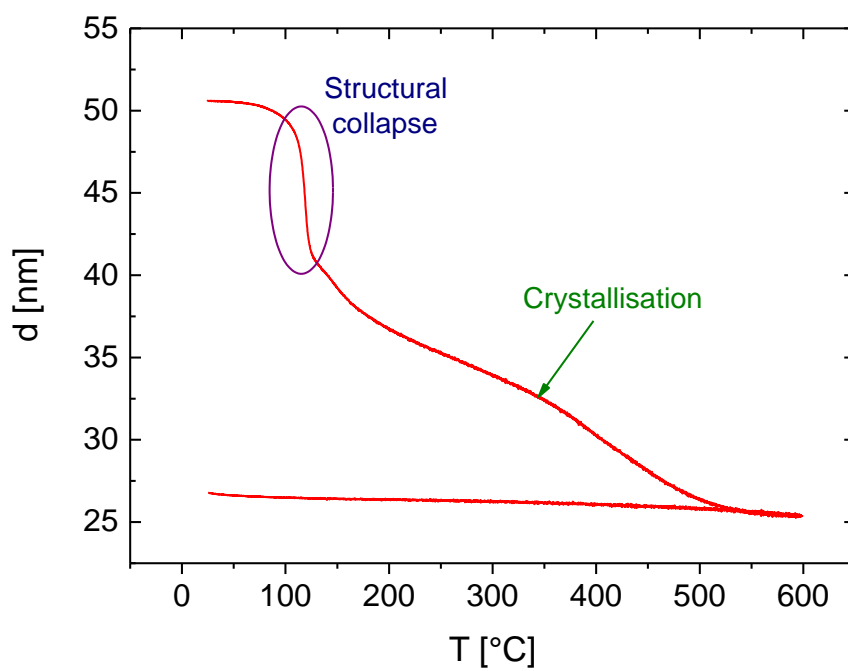
Figure 56: Film thickness vs. temperature from the SE fit

According to Figure 55 & Figure 56, the film thickness and refractive index are fairly constant below 120 °C. At 120 °C, one can observe a massive drop in the film thickness and a rapid increase in the refractive index. The thickness drop indicates a collapse of the hybrid structure inside the film explained by the removal of the film's organic content. The sudden removal of carbon and hydrogen from the film together with the breakdown of the film structure is in line with an increased electron density which explains the quickly increasing refractive index at 120 °C according to Eq 49.

Between 120 °C and 340 °C, the film thickness is slowly decreasing which is mainly related to reorientation processes of the remaining ZnO and to further carbon and hydrogen removal. The refractive index increases only marginally due to a barely changing electron density in this temperature region.

At 340 °C, the crystallization of the remaining ZnO starts. Figure 56 clearly shows that the slope of the film thickness with respect to temperature abruptly changes at 340 °C, reflecting the phase transition of the film at this temperature.

The crystallites grow mainly between 340 °C and 500 °C (see Figure 47 & Figure 48). In this temperature range, the film thickness decreases continuously with increasing temperature. Beyond 500 °C, the thickness decrease saturates meaning that the film densification process due to progressing crystallization terminates around 500 °C causing the film thickness to converge to a constant value.

Also, the XRR data (Figure 50) show a drastic increase in electron density caused by crystallization between 340 °C and 600 °C. Along with Eq 49, this explains the increasing refractive index in Figure 55. Also, the increase of the refractive index saturates for temperatures higher than 500 °C, showing the termination of the crystallization process.

When the film is cooled back down to room temperature, no significant changes in the film thickness could be measured with ellipsometry. This underlines the stability of the crystallized ZnO films. The refractive index, however, changes drastically when the film is cooled down. For non-porous crystalline ZnO, the temperature dependency of the below-band-gap refractive index at a wavelength of 630 nm is reported to be in the range of $\frac{\partial n}{\partial T} = 0.8 - 0.9 * 10^{-4}\, K^{-1}$ ([31] & [32]) In Figure 50 a temperature dependency of $\frac{\partial n}{\partial T} = 1.4 * 10^{-4}\, K^{-1}$ was measured during the cooling process. Comparing the refractive index to the electron density measured by XRR (Figure 50) shows that according to Eq 49 the electron density cannot be the determinative property for the decrease of the refractive index in the cooling regime. Rather, with decreasing temperatures, a decreased electronic polarizability is responsible for the behavior of the refractive index while cooling. The difference of the refractive index in the heating and cooling regime underlines the irreversible character of the crystallization process. Generally, the tendency of the temperature dependency of the refractive index in the cooling regime points at a crystalline ZnO film. However, one cannot ignore the difference between the reported and the measured value for the temperature dependency of the refractive index. The origin of this discrepancy is not

fully clear. Obviously, the porous structure of the film plays a role, but also the polycrystalline structure of the film as well as possible impurities can affect the temperature dependency of the refractive index.

A Maxwell-Garnet EMA fitting model was applied to the measured data in order to illustrate the development of voids during the heating process. The fitting parameter A of the Cauchy model, describing the refractive index of the host material, and the fitted void fraction inside the film, are plotted as a function of temperature during the heating and cooling process. The Cauchy model fitting parameter A for the host material is generally similar in value to the host material's refractive at a wavelength of 632.8 nm. The refractive index of bulk ZnO at 632.8 nm is roughly 2. Hence, the maximum value of A was set to 2 since higher values would be unphysical considering the possible elements inside the film. Defining a maximum value for the refractive index of the host material is physically meaningful, however choosing the right value is difficult since the refractive index of the host material cannot be measured by itself but can only be obtained from a fitting procedure. In fact, if A was not given an upper limit, the fitting procedure would converge to a refractive index of the host material that is roughly 5 and a porosity of 90 % which is totally unphysical. Hence, it is crucial to notice that the graphs below obtained from the EMA shall only illustrate the schematic development of the pores during the heating experiment. The values obtained from the fit may differ significantly from the actual physical values, for the reasons mentioned above. However, the general behavior of the film during the heating experiment is well reflected by the data below.
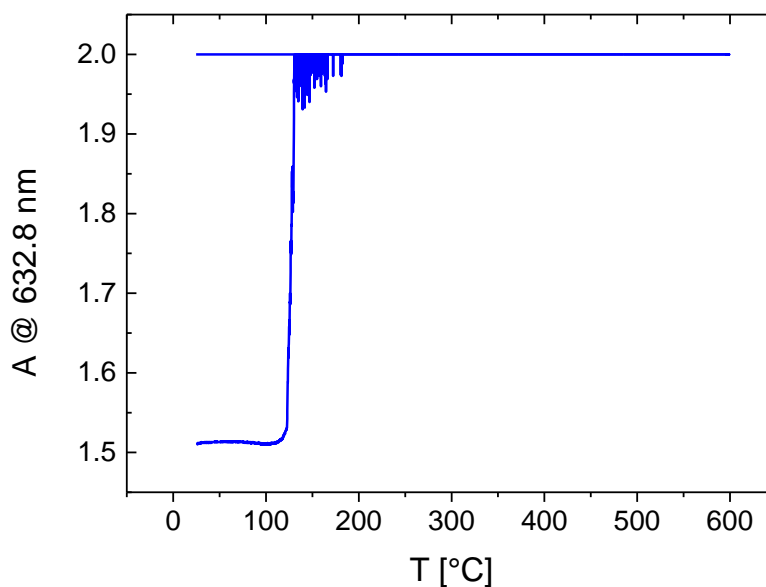
Figure 57: Host material Cauchy model fitting parameter A from Maxwell-Garnett EMA
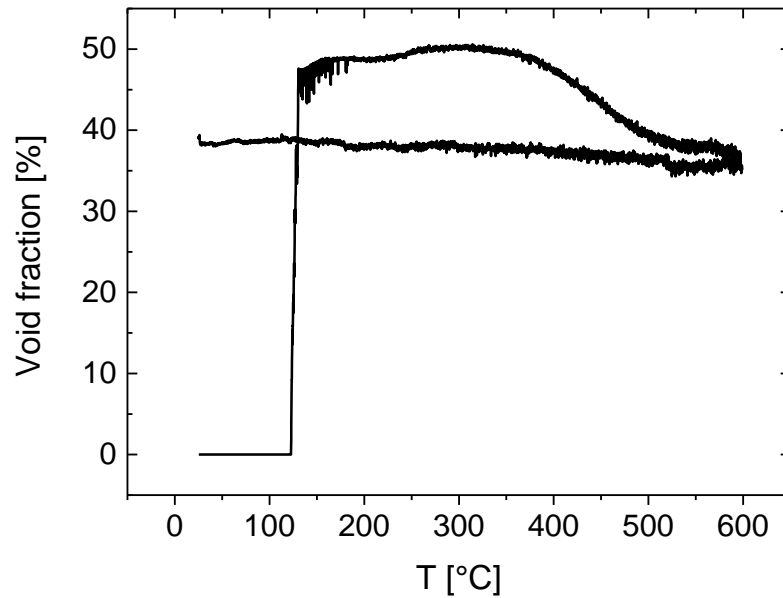
Figure 58: Total porosity from Maxwell-Garnett EMA

Figure 57 shows that the Cauchy model fitting parameter A for the host material increases rapidly around 120 °C. Hence, also the EMA suggests that the organic content is removed around 120 °C.

Figure 58 shows that the voids inside the film appear simultaneously with the carbon removal around 120 °C. Between 120 °C and 340 °C, the fraction of voids is almost constant. In the temperature range between 340 °C and 500 °C, the number of voids inside the film decreases. This can be explained by the crystallization process. While the crystallites grow, the film is densified and loses some of its cavities. Hence, the progression of the crystallization is closely related to the porosity inside the film and the void reduction ends together with the termination of the crystallization process around 500 °C.

The cooling process does not affect the porous structure of the film in any way.

4.2.2 Ellipsometric Porosimetry (EP)

In order to specify the exact fraction of open porosity, ellipsometric porosimetry measurements were carried out on films that had been heated to both 400 °C and 600 °C. Already the EMA fitting of the in situ ellipsometry measurements in 4.2.1.4 suggest that the amount of total porosity can be tuned by the maximum heating temperature. With the help of EP, this effect could be further investigated and quantified precisely.

The measurement principle, as well as the layer model for fitting the data, are equivalent to the one described in 4.2.1.4. Yet, in order to control the humidity in the atmosphere surrounding the sample, the sample stage (Dev 16) was modified. The stage was isolated from the surrounding environment with the help of a dome that was placed on top of the stage. The dome has two transparent windows that allow the incident and reflected light beam of the ellipsometer to be transmitted. Inside the dome, an atmosphere with a controlled relative humidity can be established. In order to precisely tune the relative humidity, water vapor is flown through the dome with the help of a customized vapor supply construction, depicted in Figure 59.

For the water vapor supply, gaseous N_2 was flown through a water bubbler into the inside of the dome. The total flow rate of N_2 was controlled by a simple mechanical mass flow controller (MFC, Dev 19). After the MFC the N_2 supply splits up into two lines. One line directly goes into the inside of the stage dome. The other line is connected to the water bubbler providing the desired water vapor. The N_2 flow through each line is adjustable by two needle valves (Valve1&2, Dev 20). By carefully varying the N_2 flow through the lines the amount of water vapor going inside the stage dome could be tuned. This, in turn, allowed precise control of the relative humidity in the atmosphere surrounding the sample. The relative humidity inside the dome was recorded with the help of a humidity sensor (Dev 21).
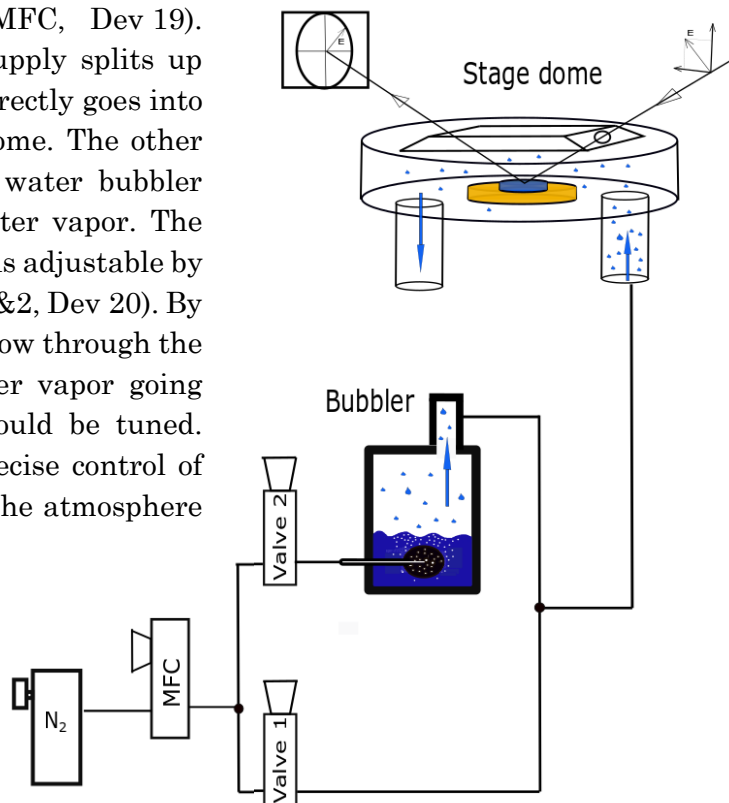
Figure 59: Experimental setup scheme for EP measurements

4.2.2.1 EP upon Heating to 600°C

The first EP measurement was done for a film that had been heated to 600 °C. For this purpose, the relative humidity was successively increased from 0 % to 95 % and was then lowered to 0 % again. Figure 60 shows the refractive index and the film thickness that were measured simultaneously with the relative humidity. When the relative humidity surpasses the 90 % mark the refractive index drops rapidly while the film thickness increases. For a single porous ZnO layer that adsorbs more and more water with increasing relative humidity, this is a very counterintuitive behavior. Typically, the refractive index should increase with increasing relative humidity because more and more pores adsorb water from the ambient (see 2.2.5). Furthermore, a discontinuous abrupt thickness increase is unlikely for a rigid host material like ZnO. The behavior of the refractive index and the film thickness for a relative humidity higher than 90 % can be explained by the formation of a water layer on top of the sample surface. The measured thickness and refractive index then hold for a thin film that consists of two layers, namely the ordinary porous ZnO layer in which the pores are completely filled with water and the additional water layer on top. Obviously, the formation of a water layer causes the total film thickness to increase. Furthermore, the refractive index of the water layer is lower than the refractive index of porous ZnO with pores filled with water. Hence, with the formation of an additional water layer the total film's refractive index decreases.

To obtain a pore size distribution from the refractive index measured as a function of the relative humidity it is crucial to associate the changing refractive index only to the amount of water adsorbed inside the pores. Yet, for a relative humidity higher than 90 % it is impossible to quantify the water layer's contribution to the total index of refraction. Therefore, in the latter, the maximum value for the relative humidity was set to 90 % assuming water adsorption inside the entire porous structure at this point.
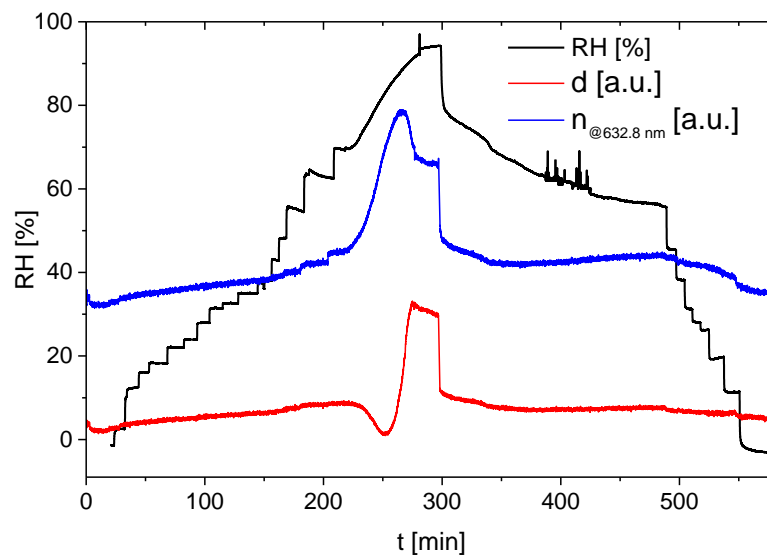
Figure 60: Relative humidity, refractive index & film thickness in EP measurement

Figure 61 shows the measured refractive index as a function of the relative humidity. The scale on the right-hand side shows the according volume fraction of adsorbed water calculated from Eq 55, showing a maximum value of roughly 13 %. Hence, the fraction of open porosity inside the film is 13 % for the sample that had been heated to 600 °C.

The hysteresis-like shape is due to differences in the adsorption and desorption mechanisms (see 2.2.5.2). Yet, in the most informative regime between 100 % and 60 %, the relative humidity could not be decreased slow enough for the slow response of the humidity sensor used. Hence, the data points in this regime are not trustful enough to create a meaningful PSD in the desorption regime. After the desorption process finished, the refractive index did not fully go back to its initial value. This is due to a residual fraction of water inside microscopic pores.

From the data points in the adsorption regime, a pore size distribution (PSD, Figure 62) was derived as described in 2.2.5.2. The PSD shows a maximum for a pore radius of 2.8 nm.

For pore radii smaller than one nanometre (microporous regime) the Kelvin equation (Eq 75) is not valid anymore. In this regime the pores are too small for a classical approach, rather requiring quantum mechanical calculations such as DFT simulations. Hence, the PSD obtained from the classical Kelvin equation is only valid for radii bigger than one nanometre. Therefore, the obtained PSDs are valid in the mesoporous regime. According to Figure 62, the volume fraction of water adsorbed in the micropores is approximately 1 %. Consequently, the fraction of mesoporosity in the film is 12 %. Cutting off the PSD for radii smaller than one and subsequent normalization of the PSD allows for the calculation of the mean value of the pore radius in the mesoporous regime. The mean pore radius of 2.9 nm was calculated which leads to an average pore diameter of 5.8 nm.
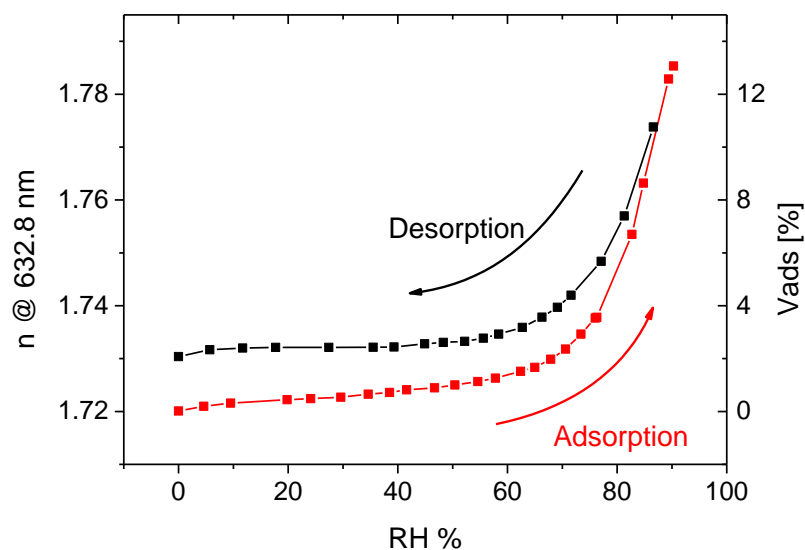
Figure 61: 600 °C film: Refractive index vs. relative humidity 1
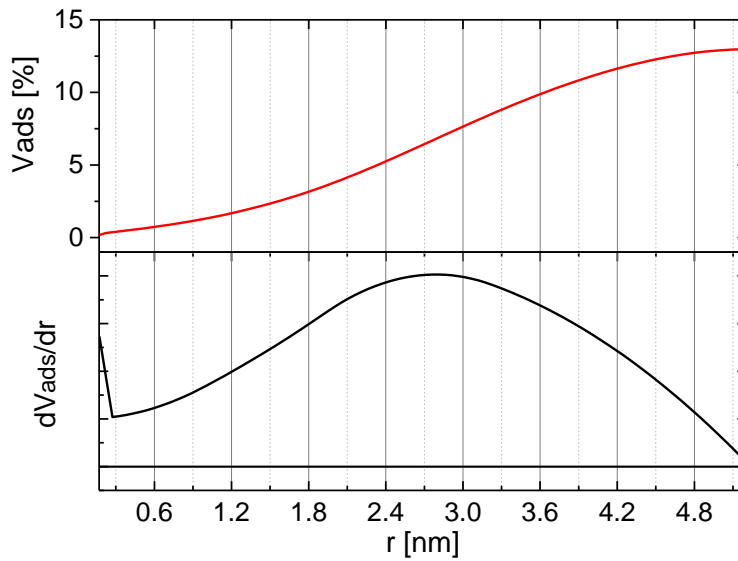
Figure 62: 600 °C film: PSD 1

In order to verify the stability of the porous ZnO film after complete water adsorption, the EP measurement was repeated for the same sample. The according PSD (Figure 63) is very similar to the one obtained in the first measurement. The main difference is a little shift of the maximum to 2.3 nm. Analog to the first measurement the PSD was cut off for radii smaller than one and was normalized afterward. From this, the mean pore radius was calculated to 2.3 nm which is a decrease of 0.6 nm compared to the first measurement. However, the total fraction of open porosity decreases only by a negligible amount.

A possible explanation would be that after the heating experiments the small pores contain some remnant impurities that are "washed out" after the first water adsorption. A contrary explanation would be that the adsorbed water introduces impurities at the surface of the pores. Since the volume to surface ratio decreases with decreasing pore radii the volume reduction caused by impurities attaching onto the surface of bigger pores is greater than for small pores. However, both phenomena would cause a change in the total fraction of open porosity which is not observed. It is also possible that the water adsorption causes small changes in the porous structure of the film. However, with a high probability, this would also change the total fraction of porosity. Hence, it is most likely that the slow response of the humidity sensor introduces a small systematic error on the pore size distributions.
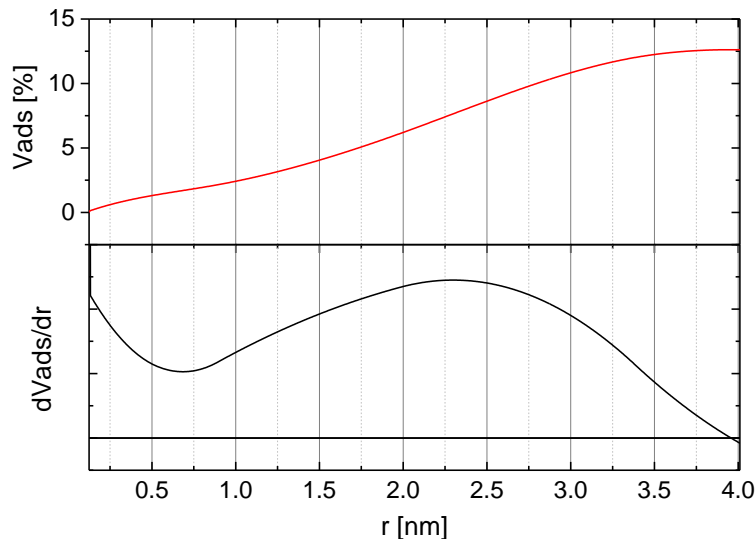
Figure 63: 600 °C film: PSD 2

4.2.2.2 EP upon Heating to 400°C

Analog to the 600 °C sample, EP measurements were carried out on a film that had been heated to 400 °C. The according refractive index as a function of the relative humidity is depicted in Figure 64. It shows that the total fraction of open porosity is 20 %, which is a significant increase compared to the film heated to 600 °C. This underlines the results of the EMA derived in 4.2.1.4 that indicates a decreasing fraction of voids inside the film for increasing temperature in the crystallization regime between 340 °C and 500 °C.

The PSD derived from the data points in the adsorption regime (Figure 65) differs significantly from the one obtained for the 600 °C sample. It shows enhanced antisymmetric features indicating an increased contribution of smaller pores. The PSD has a maximum for a reduced pore radius of 1.7 nm. However, due to the antisymmetry, the mean pore radius was calculated to the same value as for the 600 °C sample, namely 2.9 nm.

The fraction of pores in the microporous regime increased to 3 %. This strengthens the assumption that between 340 °C and 500 °C the crystallites grow at the costs of small vacancies. However, the fraction of mesoporosity is still 17 % which is a significant increase compared to the film heated to 600 °C.
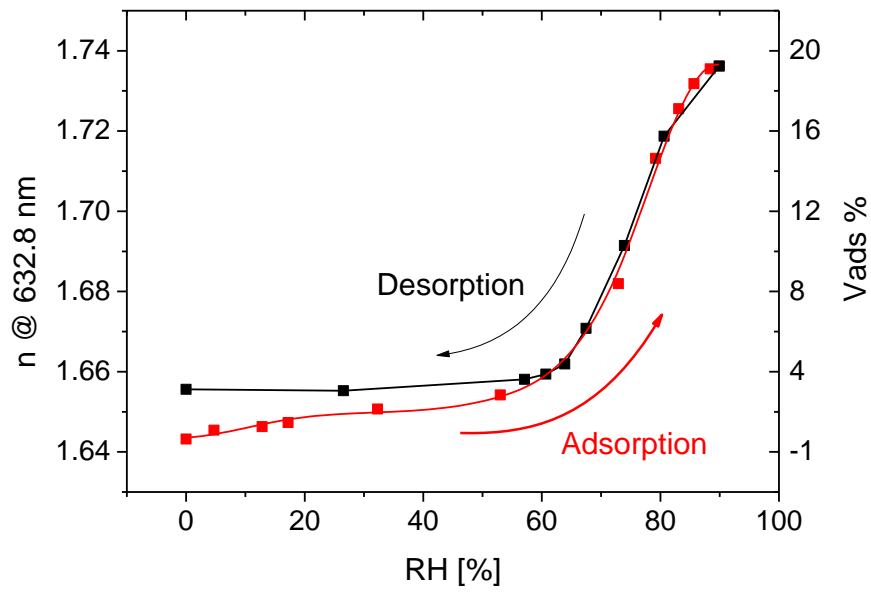
Figure 64: 400 °C film: Refractive index vs. relative humidity
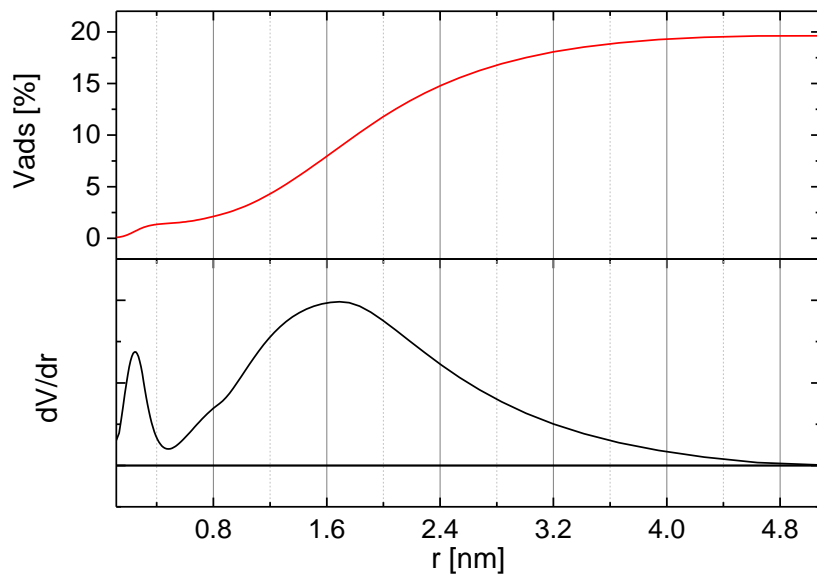
Figure 65:400 °C film: PSD

4.2.3 Degradation

Zincone films were investigated with respect to their degradation behavior in ambient air. For this purpose, frequent SE and FTIR measurements were taken on a short- and long-term range for samples exposed to ambient air (for the measurement setup see 4.2.1.1 & 4.2.1.4).

Figure 66 and Figure 67 show the refractive index and the thickness of a sample that was measured regularly with SE for three weeks. The measurements show that the film mainly changes within the first two days. Within this time span the thickness and the refractive index decrease by 3 %. For the next four days, no significant changes could be observed. After roughly one week the film's refractive index and thickness slowly start to increase reaching 98.5 % of their initial value after three weeks.

In terms of film thickness, the changes within the three weeks in ambient air are relatively small and are not comparable to the heating process. Hence, it is most likely that the main fraction of the organic content remains inside the film. However, a change of 3 % for the refractive index indicates a modification of the internal properties of the film. Earlier studies on the degradation behavior in metal-organic hybrid films using EG as the organic precursor propose that water from ambient air causes the hydrolysis of the film's organic content [8] [14].
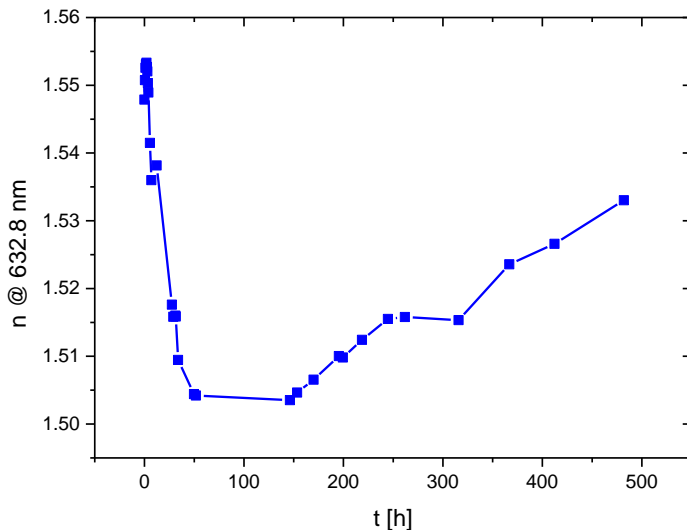
Figure 66: 3 weeks degradation: refractive index
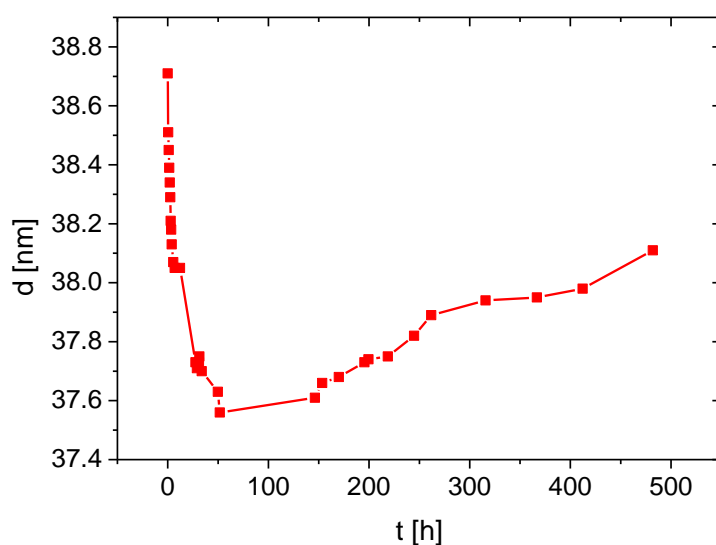
Figure 67: 3 weeks degradation: thickness

For further insight into the film mutation, multiple FTIR spectra were taken during the degradation process. The interpretation of the FTIR spectra is mainly based on literature reporting on the degradation behavior of metal-organic hybrid films using EG as the organic precursor (primarily [8] & [14])

Figure 68 shows the FTIR transmission spectrum of a Zincone film right after the deposition, pointing out the typical characteristics of the metal-organic hybrid polymer that have already been specified in 4.2.1.1.

After four hours of ambient air exposure, another FTIR spectrum was taken (Figure 69). Already after this short time span the absorption peaks at 2830 cm^{-1}, 1080 cm^{-1} and 895 cm^{-1} assigned to CH_2, $C-O$ and $Zn-O$ respectively reduce drastically. Similar behavior of Zincone films was reported in [8] and has been related to reactions with water from the ambient. Also, the appearance of the significant feature between 3100 cm^{-1} and 3500 cm^{-1} corresponding to $O-H$ stretching vibrations is a well-known attribute of a degrading Zincone film ([8]) and is attributed to hydrolysis caused by water vapor penetrating into the film.

The O-H stretching peak remains unchanged for over three weeks while especially the peak at 895 cm^{-1} disappears already after 5 days (Figure 70 & Figure 71). At the same time, peaks around and below 500 cm^{-1} are increasingly coming to the fore. These features are assigned to $Zn-O$ vibrations within an altered film structure.

Figure 70 & Figure 71 show the typical absorption peaks of C=C and $C-O$ modes. Features of this kind have already been reported as part of degradation studies on alucone films synthesized by MLD using EG as the organic precursor ([14]). Within the alucone films, these absorption peaks were assigned to enolate-type vinyl ether species in the form of $CH_2=CH-O-Al$ formed by dehydration within the organic

85

species of the film. It is highly likely that similar conversion takes place within the Zincone films. Unfortunately, within the FTIR spectra, the enolate-type absorption peaks are in the same range as the broad water feature in Figure 68 & Figure 69 (as described in 4.2.1.1 the water feature is not related to the Zincone film itself but to different environmental conditions for the measurement of the film and reference spectrum). Hence, the formation of the enolate-type species cannot be attributed to the degradation of the film at absolute certainty. Still, it is likely that the enolate-type species develops within progressing degradation.
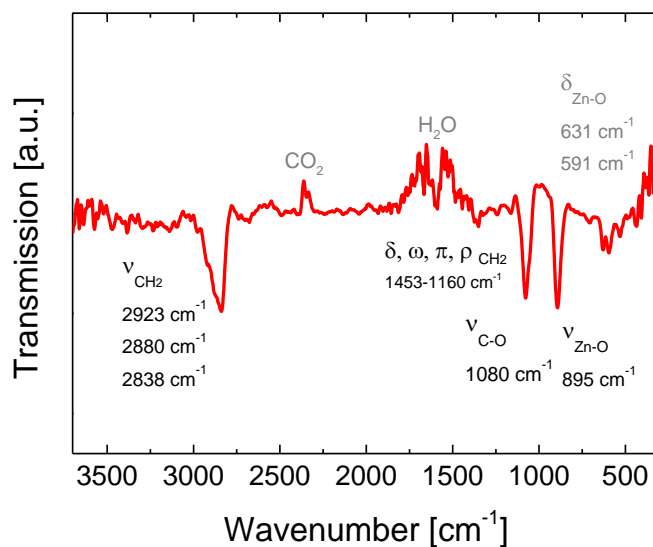
Figure 68: FTIR: Zincone film after deposition (not degraded)
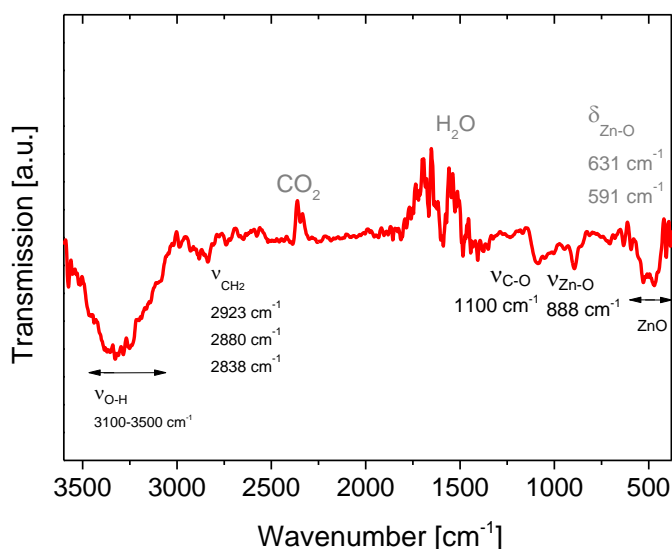
Figure 69: FTIR for the Zincone film after 4 hours in ambient air
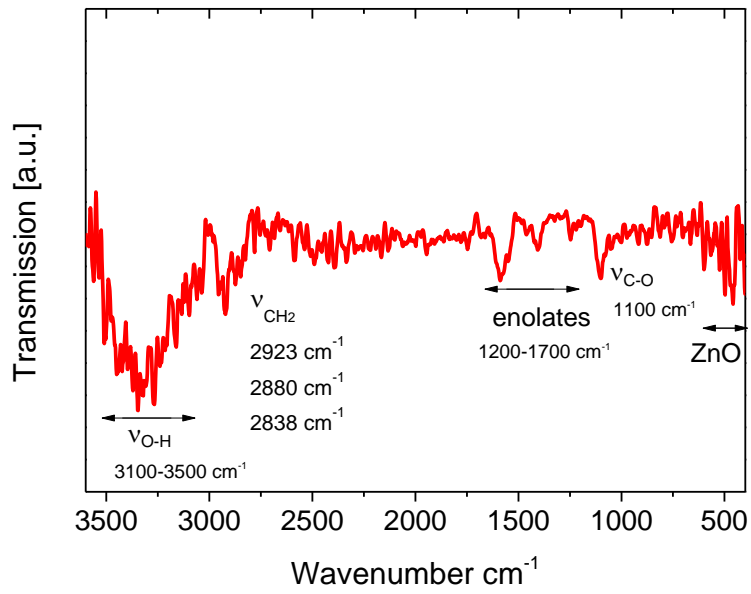
Figure 70: FTIR for the Zincone film after 5 days in ambient air
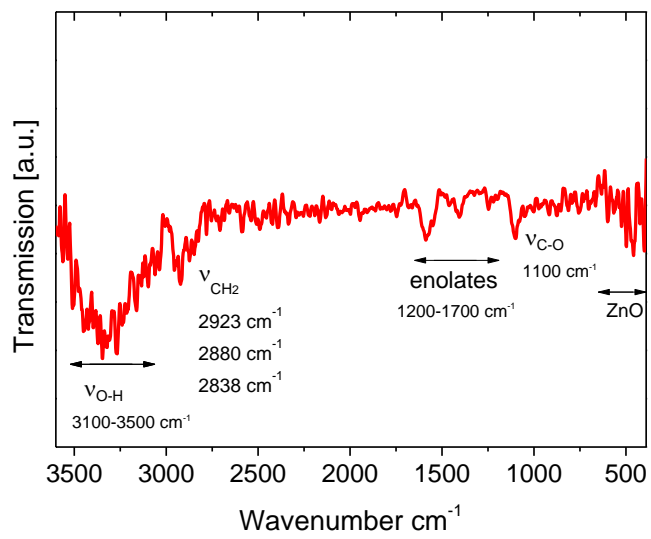
Figure 71: FTIR for the Zincone film after 3 weeks in ambient air

5 CONCLUSIONS

A MLD system was established and optimized for the synthesis of metal-organic Zincone films using DEZ and EG as the precursor and Ar as the purging gas. Especially for this system, the precursor and purging times for an ideal deposition recipe were found as (DEZ/Ar/EG/Ar) → (0.15/60/1/60) s.

According to the ideal deposition recipe, Zincone films of different thickness were produced by varying the number of MLD cycles from 30 to 500. A constant GPC of 1.055 Å/cycle was measured.

The behavior of fifty nanometer-thick Zincone films transforming to porous ZnO within heating experiments was investigated with FTIR, XRD, XRR, and SE.

FTIR measurements were taken before and after heating Zincone films to 400 °C as well as to 600 °C. Before the heating experiments, the films show typical characteristics for a metal organic hybrid structure. After heating the film to both 400 °C and 600 °C no more organic content could be measured with FTIR. Though, the FTIR data clearly suggest a film of pure crystalline ZnO after the heating process (4.2.1.1).

The film's crystallization behavior during the heating experiments was measured with XRD. The measurements show the growth of polycrystalline ZnO. The crystallite growth starts at 340 °C and terminates around 500 °C. For temperatures higher than 500 °C and after the cooling process no significant changes in the crystalline structure could be found (4.2.1.2).

With the help of XRR further material parameters such as the film's thickness, roughness, electron and mass density could be measured as a function of temperature. The electron density and mass density clearly increases with increasing temperature indicating densification due to the removal of the film's organic content and subsequent internal reorganization and crystallization supported by increasing temperatures. For the same reasons, the thickness that was also measured with SE decreases with increasing temperatures. The roughness increases with increasing temperature which can be related to both crystallization and the formation of pores at the surface. All the measurements show a stable film structure after the cooling process (4.2.1.3)

In Situ Ellipsometry shows the structural transformation during the heating process. It suggests that porosity is created due to the removal of the organic film content and that the fraction of total porosity decreases with ongoing crystallization from 340 °C to 500 °C. Furthermore, SE shows that the film collapses at 120 °C which suggests that the main part of the organic content is removed out of the film at this temperature. The overall film thickness decreases to roughly 50 % of its initial value after the heating experiment (4.2.1.4).

EP shows that the mean pore diameter in the mesoporous regime is roughly 6 nm independent of the maximum heating temperature. Decreasing the maximum heating temperature from 600 °C to 400 °C increases the total fraction of open porosity in the mesoporous regime from 12 % to 17 % respectively. According to the obtained PSDs decreasing the heating temperature also enhances the presence of micropores from 1 % to 3 %.

Finally, the stability of metal organic Zincone films in ambient air was investigated for three weeks with the help of SE and FTIR. The degradation studies show internal conversion of chemical bonds inside the film. Yet, only minimal changes in the film thickness were observed. The obtained FTIR spectra are in line with former degradation studies on metal-organic hybrid films. Mainly reactions with water from the ambient air are blamed for the film's mutation (4.2.3).

6 ACRONYM LIST

CVD	Chemical vapor deposition
DEZ	Diethylzinc
EG	Ethylene glycol
EMA	Effective medium approximation
EP	Ellipsometric porosimetry
FTIR	Fourier-transform infrared spectroscopy
GPC	Growth per cycle
MFC	Mass flow controller
MLD	Molecular layer deposition
PSD	Pore size distribution
SE	Spectroscopic ellipsometry
XRD	X-ray diffraction
XRR	X-ray reflectivity
ZnO	Zinc oxide

7 DEVICE LIST

Device	Brand	Type
Dev 1: Reactor & linte temperature controller	EMKO	ESM9711HN
Dev 2: Stage temperature controller	Omega	CN142
Dev 3: Heating wire	Winkler	WBG00402-230XX400-025000625
Dev 4: ALD valve	Swagelok	ALD 3
Dev 5: Purging gas valve	Burkert	6013A 3.0 FKM MS
Dev 6: Mass flow controller	MKS	MF1
Dev 7: Microcontroller	Arduino	Uno
Dev 8: Heating disk	Omega	KHR-2/10-P
Dev 9: Communication module	MKS	AS11870G-02
Dev 10: Rotary vane pump	Pfeifer	DUO 005 M
Dev 11: Inverted magnetron Pirani pressure gauge	Inficon	MPG400
Dev 12: Michelson interferometer	BOMEM	MB-102
Dev 13: X-Ray diffractometer	Panalytical	Empyrean
Dev 14: X-ray diffractometer heating stage	Anton Paar	DHS 900
Dev 15: Ellipsometer	J. A. Woolam Co.	M-2000V
Dev 16: Ellipsometer temperature controller stage with an additional dome	Linkam	THMS600
Dev 17: Link Pad System Controller	Linkam	T95
Dev 18: Liquid nitrogen cooling pump	Linkam	LNP95
Dev 19: Mechanical mass flow controller	KROHNE	DK800/PV
Dev 20: Needle valve	Swagelok	SS-4BMW
Dev 21: Humidity & temperature sensor	Sparkfun	SHT15

8 SOFTWARE LIST

App	Company	Software
App 1: XRR fitting software	Panalytical	X'Pert Reflectivity 1.3
App 2: Ellipsometry software	J.A. Woollam Co. Inc.	Complete Ease 5.19
App 3: MFC control software	MKS	ControlsWorkbench2.11.10.2

9 FIGURE LIST

10 TABLE LIST

11 BIBLIOGRAPHY

[1] M. Laurenti and V. Cauda, "Porous Zinc Oxide Thin Films: Synthesis Approaches and Applications," *Coatings 2018 , 8(2), 67,* 2018.

[2] S. P. Singh, S. K. Arya, P. Pandey and B. D. Malhotra, "Choleterol biosensor based on rf sputtered zinc oxide nanoporous thin film," *Applied Physics Letters 91,* pp. 063901-1-3, June 2007.

[3] P. Sharma, A. Mansingh and K. Sreenivas, "Ultraviolet photoresponse of porous ZnO thin films prepared by unbalanced magnetron sputtering," *Applied Physics Letters, Volume80, Number4,* pp. 553-555, January 2002.

[4] A. Lamberti, R. Gazia, A. Sacco, S. Bianco, M. Quagilo, A. Chiodoni, E. Tresso and C. F. Pirri, "coral-shaped ZnO nanostructures for dye sensitized solar cell photoanodes," *Progress in Photovoltaics 22,* pp. 189-197, 2014.

[5] R. Gazia, G. Canavese, A. Chiodoni, A. Lamberti, S. Stassi, A. Sacco, S. Bianco, A. Virga, E. Tresso and C. F. Pirri, "Novel sponelike nanostructured ZnO films: Properties and applications," *Journal of Alloys and Compounds, 2014, 586,* pp. 331-S335.

[6] M. Laurenti, G.-. Canavese, S. Stassi, M. Fontana, M. Castellino, C. Pirri and V. Cauda, "A porous nanobranced structure: An effective way to improve piezoelecticity in sputtered ZnO thin films," *RSC Advances, 6,* pp. 76996-77004, 2016.

[7] S. M. George, B. Yoo and A. A. Dameron, "Surface Chemistry for Molecular Layer Deposition of Organic and Hybrid Organic-Inorganic Polymers," *Accounts of Chemical Research, 2009, 42,* pp. 498-508, 2009.

[8] Q. Peng, B. Gong, R. M. VanGundy and G. N. Parsons, ""Zincone" Zinc Oxide-Organic Hybrid Polymer Thin Films Formed by Molecular Layer Deposition," *Chemistry of Materials, 2009, 21,* pp. 820-830, 2009.

[9] J. Liu, B. Yoon, E. Kuhlmann, M. Tian, J. Zhu, S. M. George, Y.-C. Lee and R. Yang, "Ultralow Thermal conductivity of Atomic/Molecular Layer-Deposited Hyvrid Organic-Inorganic Zincone Thin Films," *Nano Letters, 2013, 13,* pp. 5594-5599, 2013.

[10] B. Yoon, J. l. O'Patchen, D. Seghete, A. S. Cavanagh and S. M. George, "Molecular Layer Deposition of Hybrid Organic-Inorganic Polymer Films using Diethylzinc and Ethylene Glycol".*Chemical Vapor Deposition, 2009, 15.*

[11] X. Liang, Y.-B. Jiang and A. W. Weimer, "Nanocoating zinc alkoxide (zincone) hybrid polymer films on particles using a fluidized bed reactor," *Journal of Vacuum Science & Technology, 2012, 30(1),* 2012.

[12] P. Sundberg and M. Karppinen, "Organic and inorganic-organic thin film structures by molecular layer deposition: A review," *Beilstein Journal of Nanotechnology, 2014,5,* pp. 1104-1136, 2014.

[13] J. W. Elam and S. M. George, "Growth of ZnO/Al2O3 Alloy Films Using Atomic Layer Deposition Techniques," *Chem. Mater. 2003, 15,* pp. 1020-1028, 2003.

[14] A. Dameron, D. Seghete, B. Burton, S. Davidson, A. Cavanagh, J. Bertrand and S.M.George, "Molecular Layer Deposition of Alucone Polymer Films Using Trimethylaluminium and Ethylene Glycol," *Chemistry of Materials, 2008, 20,* pp. 3315-3326, 2008.

[15] P. R. Griffiths and J. A. D. Hasenth, Fourier transform infrared spectrometry, John Wiley & Sons, 2007.

[16] R. Berger, *Water uptake of proton conductive thin films,* Graz, 2014.

[17] D. Briggs and J. T. Grant, Surface analysis by Auger and X-ray photoeletron spectroscopy, IM publications, 2003.

[18] C. Kittel, Introduction to Solid State Physics, Oldenburg, 2004.

[19] M. Zawodzki, "Introduction in X-ray Reflectivity andGracing Incident X-ray Diffraction," TU Graz, 2013.

[20] M. Yasaka, "X-ray thin-film measurement techniques 5: X-ray reflectivity measurement," *The Rigaku Journal, 26(2),* 2010.

[21] W. Kriegseis, "Röntgen-Reflektometrie zur Dünnschichtanalyse," Justus-Liebig-Universität Gießen, 2002.

[22] J.A.Nielson and D.McMorrow, Elements of Modern X-Ray Physics, John Willey and Sons.

[23] F. Hiroxuki, Spectroscopic ellipsometry: Principles and applications, Wiley, 2007.

[24] J.A. Woollam Co Inc, Complete EASE Software Manual: Data Acquisition and Analysis Software for J.A. Woollam Co. spectroscopic Ellipsometer, J.A. Woollam Co. Inc., 2004.

[25] I. F. Almog, M. Bradley and V. Bulovic, "The Lorentz Oscillator and its Applications," 2011.

[26] D. Aspenes, "Local fild effects and effective medium theory: A microscopic perspective," *American Journal of Physics,1982, 50,* pp. 705-709, 1982.

[27] J. Dendooven, K. Devloo-Casier, E. Levrau, R. V. Hove, S. P. Sree, M. R. Baklanov, J. A. Martens and C. Detavernier, "In Situ Monitoring Of Atomic Layer Deposition in Nanoporous Thin Films Using Ellipsometric Porosimetry," *Langmuir 2012, 28 (8),* p. 3852–3859, 2012.

[28] M. R. Baklanov, K. Mogilnikov, V. G. Polovinkin and F. N. Dultsev, "Determination of pore size distribution in thin films by ellipsometric porosimetry," *Journal of Vacuum Science & Technology B: Microelectronics and Nanometer Sructures Processing, Measurement and Phenomena, 18, 2000,* pp. 1385-1391, 2000.

[29] Pfeifer Vacuum, The Vacuum Technology Book.

[30] B. Yoon, B. H. Lee and S. M. George, "Highly Conductive and Transparent Hybrid Organic-Inorganic Zincone Thin Films Using Atomic and Molecular Layer Deposition," *The Journal of Physical Cemistry , 2012, 116 (46),* pp. 24784-24791, 2012.

[31] R. Schmidt-Grund, N. Ashkenov, M. Schubert, W. Czakai, D. Faltermeier, G. Benndorf, H. Hochmuth, M. Lorenz and M. Grundmann, "Temperature-dependence of the refractive index and the optical transitions at the fundamental band-gap of ZnO," in *AIP Conference Proceedings 893, 271*, 2007.

[32] C. Bundesmann, R. Schmidt and M. Schubert, Transparent Conductive Zinc Oxide; Chapter 3: Optical Properties of ZnO and Related Compounds, Springer, 2007.

[33] K. S. Babu, A. R. Reddy, C. Sujatha, K. V. Reddy and A. N. Mallika, "Synthesis and optical characterization of porous ZnO," *Journal of Advanced Ceramics, 2013, 2,* pp. 260-265.